Observation of the Hot Electron Interchange Instability in a High Beta Dipolar Confined Plasma

Eugenio Enrique Ortiz

Submitted in Partial Fulfillment of the
Requirement for the degree
of Doctorate of Philosphy
in the Graduate School of Arts and Sciences

Columbia University

2007

Observation of the Hot Electron Interchange Instability in a High Beta Dipolar Confined Plasma

Eugenio Enrique Ortiz

Abstract

In this thesis the first study of the high beta, hot electron interchange (HEI) instability in a laboratory, dipolar confined plasma is presented. The Levitated Dipole Experiment (LDX) is a new research facility that explores the confinement and stability of plasma created within the dipole field produced by a strong superconducting magnet. In initial experiments long-pulse, quasi-steady state microwave discharges lasting more than 10 sec have been produced with equilibria having peak beta values of 20%. Creation of high-pressure, high beta plasma is possible only when intense HEI instabilities are stabilized by sufficiently high background plasma density. In LDX the HEI instability is found to occur under three conditions: during the low density regime, as local high beta relaxation events, and as global intense energy relaxation bursts. Each regime is characterized by how the plasma behaves in response to heating and fueling. Measurements of the HEI instability are made using high-impedance, floating potential probes and fast Mirnov coils. Analysis of these signals reveals the extent of the transport during high beta plasmas. For intense enough high beta HEI instabilities, fluctuations at the edge significantly exceed the magnitude of the equilibrium field generated by the high beta electrons and energetic electron confinement ends in under 100 μsec. For heated plasmas, one of the consequences of the observed high beta transport is the presence of hysteresis in the neutral gas fueling required to stabilize and maintain the high beta plasma. Finally, a nonlinear simulation code is used to compare theoretical calculations to both electrostatic and magnetic experimental observations.

Acknowledgments

I would like to acknowledge my family for their patience and endless support throughout all the years of my education, of which there have been many. Mom, Eddie, Ricky and Dad, thank you for being there for me when I needed you most. I love you all!

Next, I want to acknowledge friends who have either helped me, distracted me, or helped me by distracting me along the way. Mike & Danielle thanks for always doubting my commitment to graduate school. James thanks for teaching me so much about friendship and making graduate school that much more enjoyable. Noemi you are a great friend. Thank you for the encouragement to continue with this thesis. Melissa, thank you for the support you gave me early on. It really helped me get through the tough days and countless frustrations with the experiment. I hope you have a much easier time with your thesis. John, thank you for the comedic relief you provided and nicknames that made my time away from school fun. Seth, thanks for your incredible race car plasma analogy. I tried to include it but it turns out it was already taken. Rachael, thank you so much for your tireless patience in editing my thesis and for your willingness to do it! You made it ten time better than it would have been. Also, thank you for listening and for your constant support and understanding when I needed it most.

Next, I would like to acknowledge friends and co-workers from the PSFC. Thank you to my fellow graduate students Ishtak, Jen, and Alex B. and to UROPs Sarah, Austin and Michelle, who helped me tremendously over the years. Thank you to Alex H. for making sure all my order slips were in and for your advice and edits to my APS presentations. Also, thank you to Don and Rick for helping me build, install and fix the many components and diagnostics. I also want to thank Bill P., Jan E., and the numerous PSFC staff who provided me with electronic and digitizing support. Finally, and most importantly, I would like to acknowledge the hard work and dedication of my advisors, Mike, Jay and Darren. Without their vast knowledge, expertise, and enthusiasm this work would never have been possible.

I am very grateful for the opportunity to have worked on such a complex and innovative experiment. I only wish I could have done more to help with levitation. The best of luck to LDX as it attempts to fly!

Para mi querida madre...

Contents

List of Figures

Chapter 1

Introduction

1.1 Motivations For The Levitated Dipole Experiment

In the United States of America early magnetospheric research drew its focus from Van Allen's 1958 discovery of geomagnetically trapped radiation in the earth's upper atmosphere. When satellites began exploring this region many puzzling phenomena could be directly examined; especially, the polar aurora and disturbances in the earth's magnetic field. This region, located above the ionosphere, was dubbed "magnetosphere" by Gold [16] in 1959 due to the dominant control that the earth's magnetic field has over the motions of gas and fast charged particles. Over the next decade Explorer satellites were instrumented and launched to study the magnetosphere and gradually revealed its trapped particles, boundary, and long magnetic tail on the night side [22].

Deep space satellites have provided data that shows most of the other planets in our solar system are also magnetized with dipole magnetic field configurations much like earth's. The giant planets, initially explored by Voyager 1 and 2, are much more strongly magnetized than the Earth [3] and their magnetospheres are also much larger. This is due in part to their stronger dipole moments and the solar wind becoming increasingly rarefied far from the sun. Tiny Mercury has a magnetic moment of only about 1/2000 that of Earth and a very small magnetosphere, Venus seems non-magnetic, and the existence of a weak magnetic field surrounding Mars is still in question. For comparison purposes the magnitudes of the dipole moments of Mercury, Earth, Jupiter, Saturn, Uranus and Neptune are, in units of 10^{15} Telsa-m^3, 0.004 (approx.), 7.9, 150,000, 4300, 420 and 200, respectively [3, 33].

Parallel to the space missions exploring the magnetic dynamics of the solar system were lab experiments in which plasma scientists sought to understand the behavior of trapped,

charged particles in magnetic fields. The results of these experiments helped to explain satellite observations of natural magnetic configurations that successfully trapped and confined charged particles (plasma). The trapping of charged particles is an important concept not only to the astrophysics community but also to the magnetic nuclear fusion community. The goal of achieving controlled thermonuclear fusion reactions through magnetic confinement of plasmas in a laboratory environment still remains the driving force behind plasma research. The early lab experiments led to a further understanding of particle confinement in magnetic fields and of adiabatic invariants [45, 48, 56]. They also engendered new ideas for potential thermonuclear reaction containment devices inspired sometimes by nature herself.

Fusion reactions between charged particles occur at extremely high temperatures: temperatures hot enough to melt any vessel used to confine the plasma. Thus, in order to sustain fusion reactions it was necessary to develop a confinement device whereby no physical material came in contact with the charged particles. Magnetic fields, thanks to their special interaction properties with charged particles, can be used to trap the high energy particles, keeping them away from the walls of the confinement vessel. The question then became: what magnetic configuration makes the best magnetic bottle for confining charged particles and enabling fusion reactions? Stellarators, tokamaks and magnetic mirrors have dominated the magnetic fusion confinement scene for many years. Stellarators and tokamaks are the most extensively investigated toroidal confinement concepts while magnetic mirrors, typically linear machines, have received less attention. This thesis explores a new confinement concept closely related to the magnetic mirror.

A magnetic mirror is a magnetic field configuration in which the field strength changes along a field line in such a manner as to cause charged particles following the field line to reverse direction and bounce back from high field regions to low field regions. Thus the name 'mirror'. Magnetic mirrors occur in nature. For example, electrons and ions in the magnetosphere travel along the magnetic field lines of the earth bouncing back and forth between the poles reflected at each end by the stronger magnetic fields there. Early in the United States's fusion program, magnetic mirror machines were considered as a viable candidate for producing fusion energy, partly due to their ability to achieve high beta; the ratio of the plasma pressure to the magnetic pressure, $\beta = p/p_{mag} = 2\mu_0 p/B^2$. In fusion power applications this parameter can be thought of as a figure of merit; as it indicates the relative importance of kinetic to electromagnetic phenomena and serves as a measure of the

realistic potential for producing magnetic confinement fusion energy.

The encounter of Voyager 2 with Uranus [49] in the mid 1980s provided new observations of its magnetosphere including its high beta centrally-peaked plasma pressure, which is maintained by solar-wind-driven plasma circulation and heating. These observations motivated the proposal of a new magnetic fusion energy confinement concept, the magnetic dipole. Akira Hasegawa first proposed the dipole fusion concept in 1987 [21]. He wondered whether fusion energy could benefit from our knowledge of plasma trapped and confined naturally in the dipole-like fields of magnetized planets.

Unlike traditional toroidal configurations in which field lines define irrational flux surfaces (which surround and include rational surfaces) the dipole has closed field lines and no toroidal field. In other magnetic geometries stability requires average good curvature and magnetic shear. In contrast, magneto-hydrodynamic (MHD) stability in a dipole derives from plasma compressibility [48]. Dipole plasmas are stable to interchange and ballooning instabilities when the pressure gradients are sufficiently gentle, even when the local plasma pressure exceeds the magnetic pressure or, equivalently, when $\beta > 1$ [14]. The dipole reactor concept has advantages relative to the (magnetic shear stabilized) toroidal reactor concepts since theory suggests that high beta energy confinement can exceed particle confinement allowing for the operation of an advanced fuel cycle [30].

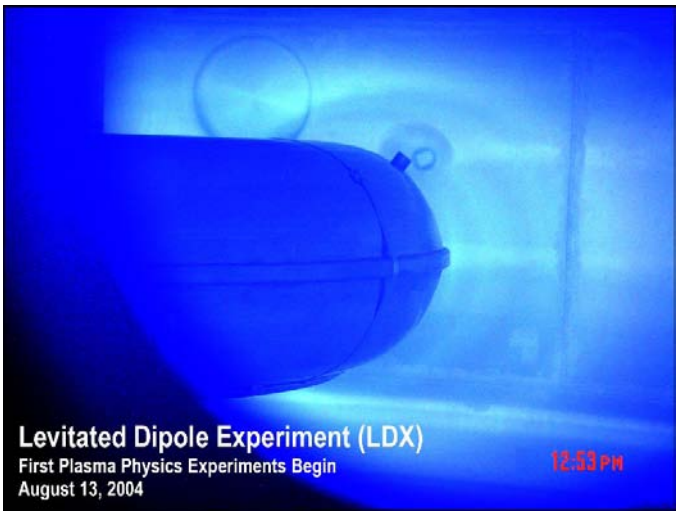

Figure 1-1: The Levitated Dipole Experiment begins operation on August 13, 2004. This is the first plasma created in LDX.

The Levitated Dipole experiment (LDX) is a new experiment built to assess the fusion potential of the dipole magnetic field configuration. It allows scientists to explore the fundamental physics of plasma confined in a dipole field and furthers the application of superconducting magnets in fusion research. LDX began operation in August 2004 conducting high beta plasma experiments in supported mode. In this first phase of operation an important step has been to evaluate the most destructive instabilities inherent to dipole plasmas. For example, under certain conditions conditions interchange instabilities can lead to a complete destruction of plasma confinement. LDX has already shown that some of these instabilities can be avoided as the experiment transitions into a high beta plasma, a critical result for the future success of the experiment. Levitation of the floating coil will occur in the near future and a large scale "pure" dipole experiment will finally be available to test the dipole reactor concept theories.

The remainder of this chapter is broken into two parts. First, it introduces the concept of interchange motion in dipoles and briefly describes the hot electron interchange mode in LDX; the main topic of this work. A more detailed reference of the theory behind dipole physics, interchange motion and the hot electron interchange mode can be found elsewhere [4, 15, 23, 31, 32, 35, 36, 41, 57, 58, 60]. The second part presents the organization of this dissertation.

1.2 Interchange Instabilities

Interchange motions are among the most basic motions of magnetized plasma. They cause transport and large amplitude interchange motion exhibits complex nonlinear effects. Interchange modes are important to ionospheric dynamics [28] and interchange motions have been regarded as being of great importance in magnetospheric physics [16, 54, 55]. They can also cause nonuniformity and gradients in a plasma that serve as a free energy source for plasma instabilities. Plasma profiles may change and confinement may be lost as a consequence of these instabilities and therefore much effort has been made to understand, probe and prevent these instabilities. In 1957 the theoretical basis for interchange instabilities was first described by Rosenbluth and Longmire [48].

In 1962 the first detailed lab observations of a plasma interchange instability, the classical fluid instability known as the Rayleigh-Taylor instability, were made in an experimental expanding plasma [9]. In fluids this instability is driven by the gravitational force and

occurs when a heavier fluid rests on top of a lighter fluid. In a laboratory dipole plasma it is driven either by the centrifugal force on particles moving along the curved field lines (like a gravitational force) or by plasma pressure gradients. It is called the flute instability because the mode structure has a flute-like perturbation. It propagates perpendicular to the magnetic field without variation along the field and exhibits interchange motion.

Similar to gravity, curvature can play a role in driving interchange instabilities. Curvature-driven interchange modes were observed in the outer regions of multipoles [44] and more recently as low frequency electrostatic fluctuations for a plasma produced by a steady state discharge in a purely toroidal device [50, 61]. Interchange motion readily occurs in laboratory dipole devices. Centrifugal interchange, for example, appears when plasma trapped in a dipole rotates rapidly [34]. Pressure gradients can also lead to interchange motion in a dipole. The role of anisotropic pressure in dipole fields and particle acceleration resulting from (μ, J) conservation was analyzed by Fazakerly and Southwood [12].

The most studied and documented interchange instability seen in a dipole is the Hot Electron Interchange (HEI) instability. As the name suggests, these are driven by energetic "hot" electron pressure gradients. Interchange instabilities with a population of energetic electrons were first described by Krall [31] and Berk [4]. Their results show that the HEI instability is distinct from a standard MHD flute instability in that it is driven entirely by electron pressure gradients. When interchange instabilities are excited by magnetically-trapped energetic electrons, the modes have a real frequency proportional to the fast grad-B drift of the hot electrons, ω_d. The Collisionless Terrella experiment (CTX) was the first to report this observation for the low-frequency HEI instability in a low beta dipole plasma. They also made the first global mode structure measurements of this instability [35] and developed a simulation code to understand the HEI instability [36, 39, 41, 42].

LDX experiments provide the first observations of the HEI instability in a high beta plasma [13,47]. ECRH power creates steep, highly localized pressure gradients. Occasionally, when the conditions are right, the high beta HEI instability can lead to a global collapse of the plasma pressure. The necessary conditions for this to happen have been identified and are discussed in chapter 4. Another manifestation of the high beta HEI instability are localized minor relaxation events [47]. As the plasma beta increases small localized pressure imbalances can lead to a rearrangement of the local pressure profile. This new instability behavior coincides with an additional drop in beta, not previously seen.

1.3 Organization

This thesis focuses on the initial high beta results from the Levitated Dipole experiment operated in supported mode. The high beta results include equilibrium plasma parameters and behavior, as well as instability measurements and studies. Most of the thesis places emphasis on experimental data and when appropriate new theory is developed and included.

The thesis is organized into five parts. Chapter 2 describes the LDX device and diagnostics tools used to control and study the high beta deuterium plasma. In addition, this chapter gives an in-depth presentation of the highly complex magnet system and gives a sense of how difficult this innovative confinement experiment is to operate. The remainder of the thesis documents the high beta equilibrium plasma results, introduces new HEI instability behavior in a high beta plasma, analyzes the transport of particles during the instability, and compares experimental electrostatic and magnetic results to a non-linear particle simulation code used to model the response of the plasma during the HEI instability.

Experiments have shown that creation of high pressure, high beta plasma is possible only when intense HEI instabilities are stabilized by sufficiently high background plasma density [13]. Chapter 3 provides the main equilibrium plasma results from initial experiments. This includes introducing the three unique plasma regimes in LDX. Each is characterized by how the plasma behaves in response to microwave heating and background fueling parameters. LDX operates long-pulse, quasi-steady state microwave discharges that last more than 10 seconds. Peak beta values have been found to be greater than 20%.

Chapters 4–6 focus on the HEI instability in LDX. Chapter 4 describes the three conditions under which the HEI instability has been observed in LDX, defines instability characteristics and compares the instability behavior for each condition. Instability behavior varies depending on the regime and unique spectral characteristics have been identified for select combinations of microwave heating and background fueling parameters.

Chapter 5 examines the transport behavior of hot electron particles during the HEI instability. A changing diamagnetic current, a product of the rearrangement of the high beta electrons in physical space, is detected by Mirnov coils. This measurement provides the first non-perturbing, high-speed diagnostic of the HEI-induced transport. The conditions under which HEI induced transport occur and the consequences of this transport to the stability of the HEI mode are also presented.

Chapter 6 takes a non-linear particle simulation code developed by CTX [42], HEI_SIM, and adapts it to LDX parameters and conditions. In addition, a magnetic module was created and added to probe the simulation code giving results that can be directly compared to the experimental Mirnov coil signal. This chapter attempts to paint a coherent picture of the plasma behavior during the HEI instability through simulations and comparisons with magnetic and electrostatic signals. Finally, a summary of all results is given in chapter 7.

Experimental data presented in this thesis has been obtained in a supported mode dipole experiment. Although the aim of the experiment is to levitate and create a "pure" dipole plasma, plasma experiments with controlled magnet levitation were not achieved in time to be included in this thesis.

Chapter 2

The Levitated Dipole Experiment

Measurements described in this work were made using the Levitated Dipole Experiment (LDX); a new research facility developed and built at the MIT Plasma Science and Fusion Center as part of a joint research project with Columbia University. LDX aims to investigate the confinement and stability properties of magnetized plasma in a dipole field configuration generated by a strong superconducting magnet [29]. This chapter describes the LDX device as well as the tools and diagnostics used to control and study the plasma.

2.1 The LDX Device

As shown in Figure 2-1, LDX consists of an internal superconducting coil located within a 5 m diameter vacuum vessel. Experiments have been conducted with a dipole coil current (I_d) up to 1.2 MA, leading to a dipole moment ($M \equiv \mathrm{B_\circ L_\circ^3}$) of $0.34\, I_d$ A·m^2. A large bore superconducting coil, located below the main vessel, is used to inductively charge the dipole coil which is lifted for plasma experiments by a vacuum hoist. In supported mode configuration three 0.75 cm diameter support rods intersect the plasma causing heat and particles to be lost. Operations during the first year have focused on understanding the experiment and confinement of thermal plasmas while operating a supported dipole. In future experiments the coil will be magnetically levitated, eliminating losses to the supports.

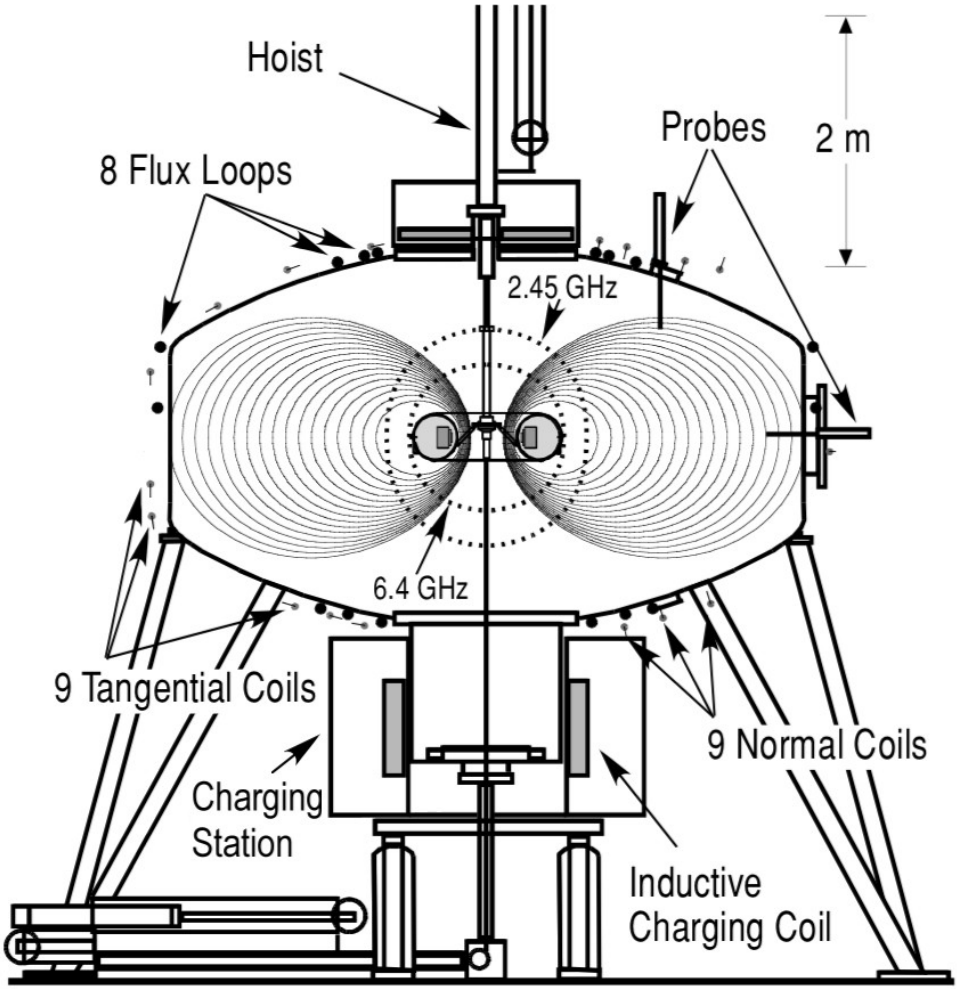

Figure 2-1: This schematic of LDX shows the dipole magnet suspended within the vacuum vessel. Loops and coils measure the equilibrium plasma current and probes measure fluctuating potentials. Injected microwave power strongly heats electrons at the cyclotron resonance.

2.1.1 Magnets

The partnership between plasma scientists and magnet technology experts is an integral and vital element of the success behind LDX. Through innovative engineering and design three super-conducting magnets were built and tested for steady state operation [52]. They are the floating or **F-coil** [53, 63, 64], the charging or **C-coil** [65], and the levitation or **L-coil** [51]. In addition, a pair of copper Helmholtz coils are installed for pulsed operation and plasma shaping experiments. Below is a description of all four coils.

Floating Coil

The floating coil is the internal superconducting coil that will be magnetically levitated in the center of the LDX vacuum vessel. The floating coil was fabricated in two phases. The first phase includes the coil winding and impregnation. It was performed by Everson Electric in Bethlehem, PA. Subsequent testing was completed at MIT in a helium pool where the magnet coil was energized without quenching up to 2.2 kA. The second phase encapsulated the magnet coil into a cryostat fabricated by Ability Engineering Technology in South Holland, IL. Lastly it was brought back to MIT for final testing before its first successful operation in August 2004.

The magnet was designed to carry up to 2.07 kA (or 1.48 MA-turns) yielding a peak field in the center of the doughnut of 5.3 T. It is made from 1.5 km of advanced pre-reacted Nb_3Sn Rutherford cable having a critical current greater than 1.5 times that of the ITER conductor; extending its duration up to several hours of operation [53, 64]. The operating temperature range is between 4.5 K and 10.8 K. The magnet coil sits inside a helium filled pressure vessel that is itself surrounded by a fiberglass-lead composite thermal shield and a toroidal Inconel 625 vacuum vessel shell with major and minor diameters of 762 and 254.5 mm, respectively. The mass of the coil is 550 kg and is broken down as follows: 250 kg magnet coil, 150 kg helium vessel, 60 kg radiation shield, and 90 kg vacuum shell [62, 63]. Figure 2-2 shows a cross section of the cryostat.

The cryostat design allows the coil to levitate safely for several hours without electric and cryogenic connections. While the cryostat is being cooled, it rests at the bottom of the LDX vacuum vessel in a special section called the "charging station", see Figure 2-1. Retractable cryogenic transfer lines are used to cool down the magnet for operation. The F-coil can be

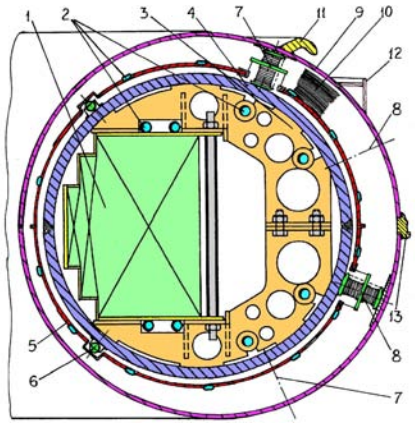

Figure 2-2: Cross-sectional view of the floating coil cryostat. 1. magnet; 2. heat exchanger; 3. gusset; 4. helium vessel; 5. radiation shield; 6. glass ball shield support; 7. vacuum shell and shield support; 8. side bumper; 9. vacuum shell; 10. MLI; 11. lifting disk; 12. laser beam control structure; 13. vacuum shell ring. (from Ref. [64] with permission)

re-cooled without loosing its field (or current) in-between plasma runs and has been done routinely in each of the first year experimental runs.

Charging Coil

The charging coil was constructed in St. Petersburg, Russia by the Efermov Institute. It is made from 35 km of NbTi conductor formed into a large 8-ton, 4 MA coil [65]. Tests conducted in March 2003 revealed that the coil operates quench free up to 440 A. This is less than the design value by approximately 86 A, see Table 2.1. This will limit the maximum F-coil charge and peak plasma beta. Nevertheless, it has been determined that the physics program will not be affected and the recovery of the remaining design current can be performed at a later date as part of a facilities upgrade.

The C-coil is a free standing solenoid magnet encapsulated by a low heat leak liquid helium bath cryostat and having a warm bore of more than 1 m in diameter. A four-quadrant 40 V and 600 A power supply is used to charge the C-coil. The C-coil inductively charges and discharges the floating superconducting magnet up to a value of 1.65 kA (2.07 kA nominal). This is only possible when the F-Coil is situated inside the charging station, name given

Parameter	Value
Total number of turns	8250
Winding density, turns/m^2	7.4×10^4
Operating current, A	526
Stored energy, MJ	12.5
C-coil self inductance, H	88.85
F-coil self inductance, H	0.3886
Mutual inductance of C and F-coil, H	1.688
C-coil protection dump time constant, s	< 17.2

Table 2.1: Design parameters of the C-coil winding pack, from Reference [65] with permission.

to the special large cylindrical flange inside the C-coil warm bore and holding all of the cryogenic and electrical connections required for proper F-coil diagnosis and operation.

A magnet quench protection system exists to protect both the superconducting C-coil and the power supply in case of a quench or a power failure. It can dissipate most of the 12.5 MJ of stored energy released during a quench through a very large external dump resistor. Once the F-coil is out of the charging station, the C-coil protection circuit must remain open. In the March 2003 testing trials the quench protection system was tested and worked as expected.

Levitation Coil

Levitation of the F-coil is achieved using a disk-shaped, high-temperature super-conducting L-coil. Located on top of the vacuum vessel, its position is stable to tilt and horizontal displacements, thus reducing the control power requirements for motions in off-axis directions. The L-coil is a BSSCO-2223 coil and is the first high temperature superconducting coil to be used in a fusion program experiment [51, 62]. The coil winding and cryostat were manufactured at Everson Electric Company in Bethlehem, PA.

The L-coil cryostat uses very little cryogen to operate. Instead, the coil is conduction cooled by a cold head inserted into the top of the cryostat. The Cryomech cryocooler has 20 W of refrigeration at 20 K. High temperature superconducting leads are used to reduce the heat load to the cold mass and a cooled copper thermal shield is used to intercept room temperature radiation. The shield is cooled by a liquid nitrogen reservoir located in the top

of the vacuum can. During operation, the liquid nitrogen reservoir is automatically re-filled to the desired level.

The L-coil power supply was specifically designed for the LDX experiment. The 15 kW, 2 quadrant power supply provides up to 150 A dc and ± 100 V dc. A secondary crowbar circuit exists to protect against a loss of the F-coil control and prevent catastrophic damage to the F-coil. The power supply is also equipped with an integrated dump resistor for rapid discharge. A complex and realtime feedback system provides vertical stability to the F-coil during operation by adjusting the L-coil power supply. A series of internal flux loops as well as laser diagnostics are fed into the system to keep the F-coil levitated.

Typical Magnetic Field and Helmholtz Coils

During the first year of operation LDX ran with three separate magnets in a supported dipole magnet configuration. The first two, F-coil and C-coil, have been described above. The third, a pulsed Helmholtz coil, was manually made out of an insulated copper conductor. Assembly occurred underneath the main vacuum vessel and before the C-coil was in place. Each coil consists of 16 turns of 1/2 inch copper conductor with a paper insulator and has a final diameter of 4.7 m. Each coil can carry up to ±4 kA at 400 V for short pulses lasting only a few seconds. The coils are shown on the LHS in Figure 2-3.

Cooling occurs radiatively and therefore over-heating of the coils becomes an issue near maximum current operation. Readings of the top-coil temperature, taken in-between shots, have shown that two things can be done to keep the temperature down. The first is to slightly increase the time in-between shots, especially after a large current load. The second is to alternate high and low current loads between consecutive shots. By applying these two restrictions, operation of the Helmholtz coils can be sustained indefinitely while keeping the temperature below the insulation melting point. This will avoid a short and the costly installation of additional cooling schemes.

Helmholtz coils are used to investigate the relationship between the plasmas outer-boundary and the ability of the dipole configuration to confine high beta plasma. This is done by using the Helmholtz coils to shape the plasma, change the compressibility and even create a null divertor. The plasma volume decreases as the Helmholtz field increases as is observed in simulations that calculate the magnetic geometry, see Figure 2-3. And since the two Helmholtz coils are connected to separate power supplies, individual adjust-

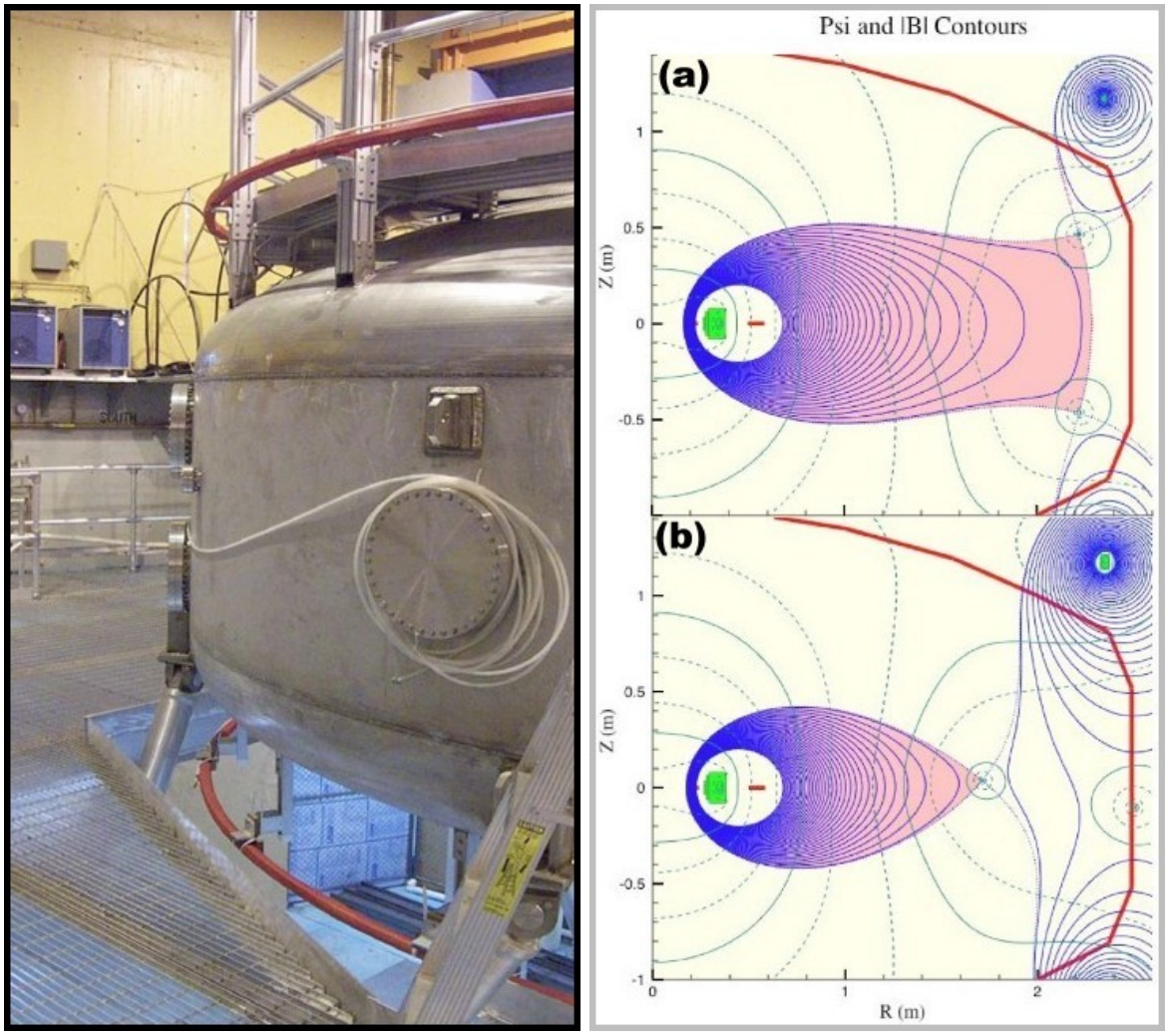

Figure 2-3: LHS – The LDX Helmholtz coils are shown above wrapped in red tape. RHS – The magnetic geometry for a Helmholtz field created with (a) 30 kA-turns and (b) 50 kA-turns is shown above. As the Helmholtz field increases an "x-point" forms and the enclosed plasma volume shrinks (pink area) [19].

ment of each coil's current will change the Helmholtz field shape and intensity. With high enough currents the simulations also reveal the presence of an "x-point" or toroidal field null that forms at different radii. Depending on the level and shape of the Helmholtz field, again see Figure 2-3, the divertor(s) can be set along, above or below the axis of symmetry. Experiments which take advantage of this fact have been conducted and investigate the stability and confinement properties of both single and double point divertors during high beta plasmas. For these cases it has been found that the reduction of confined plasma volume changes the plasma compressibility and lowers the total stored energy. In general, the results presented in this Thesis will be from plasmas created without a Helmholtz field, unless otherwise specifically indicated.

Operating the Magnets

Operating the superconducting magnets of LDX requires patience and technical experience with cryostats, in particular liquid helium (LHe), liquid nitrogen (LN_2), gaseous helium (GHe) and gaseous nitrogen (GN_2). LHe is the major experimental expense due to the large quantities needed to cool the superconducting magnets. A typical three day run campaign consumes between 3,000 and 4,000 liters. The price of LHe is approximately $\$\,4$ a liter and the annual budget for LHe is set at $\$\,150{,}000$. This enables only nine run campaigns throughout the entire year. Because of this high expense, the LDX helium recovery system was built to save the experiment about 25% in total helium costs. This re-adjusts the real cost of LHe to about $\$\,3$ per liter, a savings of about $\$\,40{,}000$ per year, or the addition of two or three run campaigns.

Preparing for an experiment begins at least one week in advance and requires strict monitoring of the cooling for all superconducting magnets. Everything begins with the ordering of LHe since it has the longest lead time for the quantities needed. Cooling of the C-coil follows and must begin a week in advance to running if starting from room temperature. If kept bathed in LN_2, the C-coil takes only three days to cool down. On the day of the run the F-coil is also cooled. First by cold GN_2, then by LN_2, and finally by LHe flowing through the cryostat heat exchanger. This can take anywhere from 4–6 hours. When the F-coil is close to 17 K the C-coil is charged. Inductive charging of the F-coil begins when its helium vessel reaches temperatures below 8 K. A inductive discharge of the C-coil charges the F-coil and the C-coil is left as an open circuit. Cooling of the F-coil helium vessel continues

until it reaches a temperature near 4.5 K and then the flow is terminated and the retractable cryogenic transfer lines are removed and instrument connectors are detached. The F-coil and the vacuum systems are now ready for experiments.

At this point, the F-coil is moved to the middle of the vacuum vessel and plasma can be created continuously for up to two hours. Plasma shots are typically 4 to 12 seconds long with an additional 3 minutes for the data acquisition to complete the store cycle. This translates to one shot every 3–5 minutes. The two hour limit on the F-coil has been studied for various F-coil charging currents and includes a 15 minute buffer to insure the F-coil remains superconducting and can be safely brought back down without quenching. Once back in the charging station instrument connectors and cryogenic transfer lines are reattached. Depending on the day's run plan the F-coil is either re-cooled by the LHe flow for the next plasma experiment or the F-coil is discharged using the C-coil. In the latter case a warm GHe flow is used to bring the F-coil temperature above 17 K and the C-coil is discharged [63].

2.1.2 Vacuum System

The LDX vacuum system can reach pressures of 10^{-7} Torr and is composed of a large main vacuum vessel (> 65 m^3), custom and standard diagnostic flanges, gate-valves and a series of pumps and pressure gauges. It is partially controlled by a Allen-Bradley process logic controller (PLC) running RSLogix 5 software. It is capable of displaying any diagnostic readings (such as pressure gauges), storing data, and remotely turning on/off any components with this capability. Ladder logic has been used to program the PLC so as to protect the remote controllable pumps and other sensitive equipment in case of a vacuum accident. The rest of this section describes the key components used to create a vacuum in LDX.

The vacuum vessel is kept at low pressures by a turbo-molecular pump and two cryo pumps. The pumping speed of the turbo and cryo pumps is 1,000 liters/s and $>$ 20,000 liters/s (mostly H_2O), respectively. The turbo-molecular pump located on top South-West 16 inch port is horizontally mounted and situated behind a remote controllable gate valve. A gridded screen has been welded inside the vessel to prevent plasma from coming in contact with the gate valve o-ring. Each cryo pump is located on opposite ends of the vessel and on the 24 inch North and South ports. They have built in manually operated gate valves.

The rest of the pumping stack includes a very large mechanical pump which has a pumping speed of 3,000 liters/s and is used to rough pump the vacuum system and two rotary-vane pumps to back the turbo pump, each with a pump speed of 200 liters/s.

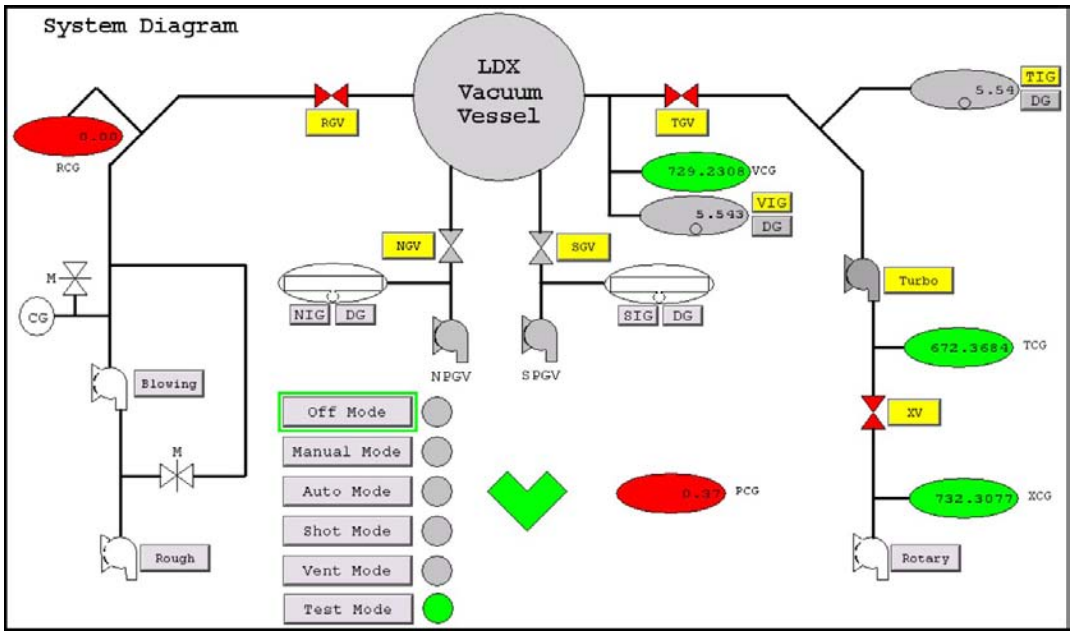

Figure 2-4: The vacuum pressure can be monitored using a Process Logic Controller (PLC) and computer software. The various vacuum components are displayed above. Depending on the selected mode, the different pumps and gauges can be turned on/off. In addition, safety limits have been coded into the logic to prevent damage of critical systems during a vacuum accident.

Several gauges measure the pressure in the vacuum vessel. A Pirani gauge, starting from atmospheric pressure, is used to observe when the roughing pump brings down the pressure into the milli-Torr range. This process takes about half an hour when the vessel is filled with nitrogen. Two convectron gauges, one located on the same port as the turbo pump and the other in the backing line of the turbo pump, are used to monitor the pressure down to a few milli-Torr and are hardwired into the PLC. Two ion gauges, one behind the turbo pump and one in front of the turbo pump, monitor the pressure below a milli-Torr and are also hardwired into the PLC. Figure 2-4 shows the interface used to control the LDX vacuum system.

Glow Discharge

The conditioning of plasma facing surfaces is a common operation done in plasma physics experiments. Typically, this occurs following a vessel up-to-air opening or a major leak. Some experiments even include it in their routine experimental operations. A variety of techniques exists which will remove loosely bound low-Z impurities from the plasma facing components or bind them to the surface. These include baking, glow discharge cleaning (GDC), pulsed discharge cleaning and RF discharge cleaning. Due to the large surface area ($\sim 80\,\mathrm{m}^2$) of the LDX vacuum system the technique most suitable for the purpose of in situ conditioning is GDC.

The ability of a glow discharge plasma to enhance the chemical reactivity of the constitutive gases has given rise to its application for conditioning large ultrahigh vacuum systems. The development of GDC techniques in magnetic fusion research has been driven by a technical requirement to minimize particle-induced deposition coefficients and a practical requirement to find a cost-effective means of surface cleaning [10]. GDC has proven to be useful for both impurity removal and hydrogen recycling control and is routinely used in many fusion devices [1, 2, 26, 46].

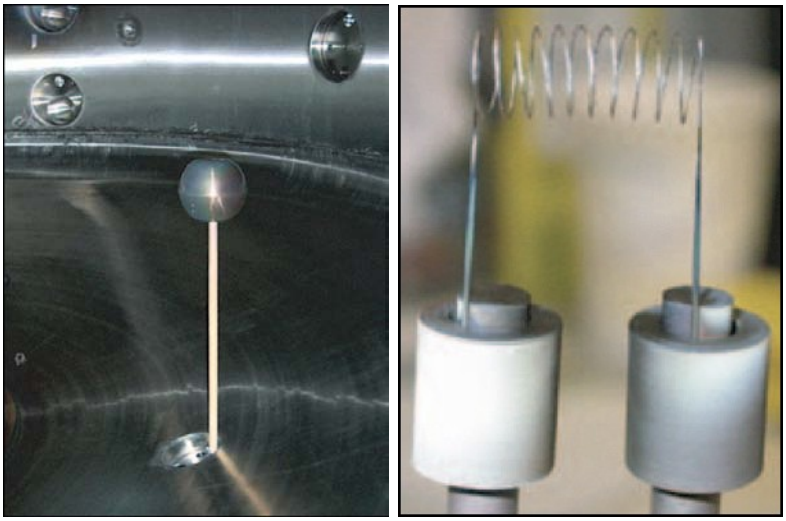

Figure 2-5: LHS – The GDC system anode extends up a meter into the vessel on a ceramic rod. RHS – The tungsten filament aids the operation of GDC at lower background pressures by emitting electrons into the plasma.

LDX has built and implemented (as of January 2004) a simple dc glow discharge system. The discharge gases (H_2, D_2, Ar, or He) are supplied by the gas injection system and the vessel pressure (in the range of a few milli-Torr) is maintained using a feed-back loop on the PLC. A high voltage power supply (1 kV) is used to bias an anode mounted on a movable ceramic rod, seen in Figure 2-5. This power supply can be operated either in voltage or current control mode with a maximum of up to 7.5 kW. In addition, a tungsten filament is heated and biased at -300 V dc to provide the necessary electron emission for stable low pressure operation. Arc formation has been minimized by placing a large $25\,\Omega$ resistor in series with the power supply and anode system. During GDC the turbo pump provides sufficient pumping speed to remove impurities, although it performs less effectively in removing hydrogen.

In LDX the GDC is typically used as a two step process: (1) to remove oxygen and other volatile impurities, mostly with hydrogen (H_2-GDC) fuel but sometimes with argon, and (2) to enhance hydrogen and CO desorption with helium (He-GDC) [37]. The important advantage of using H_2-GDC is the chemical nature of the cleaning mechanism as opposed to the physical sputtering effects which dominate when heavier gases are used. Previous work done with GDC, summarized by Dylla [10], shows that when using H_2-GDC the ion energy distribution of the cathodic flux from a dc-driven glow has a dominant peak at or near the anode potential and for the molecular ion H_2^+. Therefore, it is important to keep the supply voltage below 500 V dc (the sputtering threshold) to minimize the translational energy of each H^+ ion. This will in turn reduce the H^+ sputtering and allow for a faster recovery from hydrogen implanted walls typical of GDC. Larger ion GDC, such as He-GDC, takes advantage of particle induced desorption processes. A typical wall conditioning schedule for LDX may include three days of GDC prior to the start of a run. Table 2.2 summarizes how this GDC can be applied after an extended up-to-air period.

2.1.3 Plasma Heating and Fueling

ECRH

Plasmas are created by ionizing and heating deuterium gas using microwaves that resonate with the electron gyro-motion (electron cyclotron resonance heating or ECRH). Two ECRH sources provide heating power for LDX plasmas. The sources are a Gerling magnetron at $f_\mu =$

Hrs	Tech	Adj Vac (mTorr)	PwrSup Volt(V)	PwrSup Curr(A)	PwrSup Mode	Filament Bias(mA)	Filament Heat(%)
12	H_2-GDC	10	300	1–3	VoltCtrl	30	75
4	Ar-GDC	5	400	2–4	VoltCtrl	60	75
24	He-GDC	5	400	2–6	VoltCtrl	60	75

Table 2.2: An example of a wall conditioning schedule and operational settings for the LDX GDC system after an extended up to air period. Increasing the He-GDC time up to three days is preferred.

2.45 GHz and a Varian klystron at $f_\mu = 6.4$ GHz. Each delivers a maximum continuous wave power of 3 kW [20]. The microwaves from each source are transmitted to the experimental vacuum vessel via 6 m waveguide runs. The antennae inside the vacuum vessel are made from segments of waveguide cut at the appropriate angle so as to maximize the transmission and minimize the directivity, see Figure 2-6. The vacuum vessel forms a microwave cavity and the waves execute multiple passes through the plasma until they are absorbed by resonant electrons. A small first-pass absorption is followed by multiple reflections of microwaves which has the benefit of making the heating relatively isotropic. Forward and reflected power are measured by a directional coupler positioned within the waveguide.

For electromagnetic waves, such as microwaves, to propagate into the plasma they must have a frequency below the electron plasma frequency $\omega_{pe}^2 \equiv n_e e^2/\epsilon_o m_e$, where n_e is the electron particle density, m_e electron mass and ϵ_o is the permittivity of free space. In LDX, this constrains the density to values below $n_e < 7.5 \times 10^{10}\,\mathrm{cm}^{-3}$ for 2.45 GHz ECRH and $n_e < 5.1 \times 10^{10}\,\mathrm{cm}^{-3}$ for 6.4 GHz ECRH. The dotted lines in Figure 2-1 show the heating regions for both sources.

Fueling

The gas injection system prepares, mixes, and leaks various types of experimental grade gases into the vacuum vessel. The system consists of the necessary hardware and software to control the flow remotely from the control room. Key hardware components include: steel and aluminum gas cylinders, gas regulators, regular and flexible tubing, flashback arresters, H_2O and hydrocarbon filters, inline mixing, and storage tanks and gas injection valves. The PLC control layout of the gas injection system is shown in Figure 2-7.

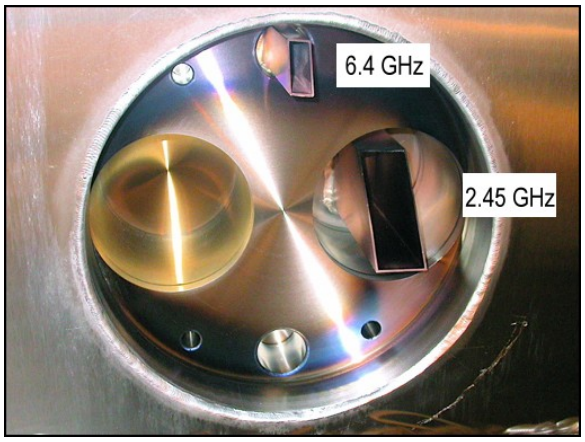

Figure 2-6: The image above shows the antennas used for ECRH heating. They are made from segments of waveguide cut and mounted onto a side port. Relatively isotropic heating occurs due to the reflections in the vessel cavity.

The main component to the gas injection system is the piezoelectric gas flow valve (model No. PEV-1). This high precision gas leak valve uses a piezoelectric bender element that responds directly to a voltage signal. A thresh-hold value exists between 20–30 V dc and the valve opens with a response time of 2 milli-seconds. Gas flows from the main cylinders via (oxygen pre-cleaned) stainless steel tubing to a storage tank and then into the inlet of the piezoelectric valve. Gas puffing experiments suggests a linear relationship between the equilibrium vacuum pressure and gas puffing frequency. These experiments were done using the following parameters: piezoelectric valve inlet pressure of 15 psi, a low frequency (< 10 Hz) square wave with a 45 volt amplitude and 15 milli-second pulse width and helium gas.

The two main uses for the gas puff system are to puff gas for experimental plasma discharges and to continuously provide gas for GDC conditioning. Up to four gases can be accessed by the system. The three modes of gas injection system are: (1) continuous flow at constant pressure; (2) pulsed flow by program control, (3) pulsed flow via density feedback control or grass control. The system can also handle the introduction of gaseous impurities or mixtures via a second piezoelectric valve. Currently, plasma experiments use high grade deuterium (D_2) with a purity better than 99.7%. For wall conditioning high purity (99.999% pure) H, He and Ar are used. Purging of the system is also possible via the PLC interface.

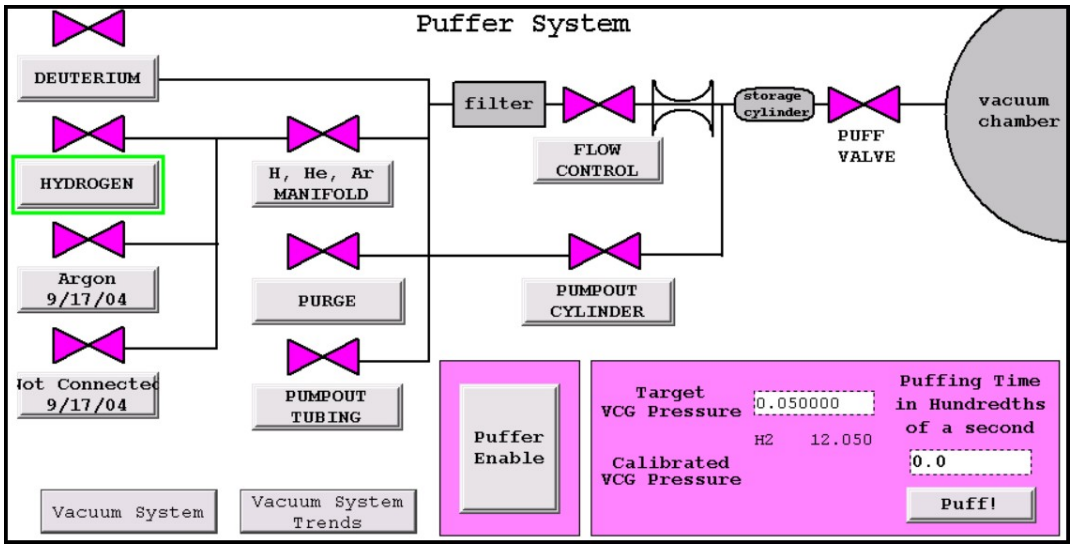

Figure 2-7: LDX has several options for fueling as the PLC layout above indicates. Experiments can be run with separate gases or as mixtures. Although most of the experiments to date have used deuterium, xenon can be used for comparative studies.

2.2 LDX Diagnostics

An expansive set of relatively low-cost diagnostics are operational on LDX and take advantage of the excellent access to the plasma. They measure global equilibrium plasma parameters including stored energy, and pressure profile, plasma density, hot electron energy, plasma fluctuations and instabilities, and edge plasma characteristics. Data from these diagnostics is digitized, processed, and stored via MDS-Plus. Additional recorded video is also stored separately.

LDX was designed to produce high-temperature, high beta, low-density plasmas (relative to many tokamak experiments). These characteristics permit the use of intrusive probes as a way to measure edge parameters. The probes, known as Langmuir probes, measure the edge electron temperature, density, ion saturation current and electrostatic fluctuations. They can be fixed to a single point in space or moveable. On LDX a motorized probe interface system allows for a single probe to move linearly about a vertical (or horizontal) chord of the outer magnetic field topology. This system also uses a stand-off gate valve designed to enable the replacement of probe tips in situ, in-between run campaigns and without venting

the main vacuum vessel. The following section describes the current Langmuir probe system.

2.2.1 Probe Diagnostics

Electric Langmuir probes have been operational on LDX since the first run in August 2004. Figure 2-8 shows the first three Langmuir probes installed. These three are permanently attached to the outer mid-plane while another four probe stands allow for additional probes to be used during experiments. During the supported dipole campaign data has been collected using various Langmuir probes including: swept single tip, swept dual Mach tip, non-swept negatively biased ion saturation and floating potential type probes.

Langmuir probes serve two purposes: (1) swept probe data provides edge equilibrium parameters and (2) fixed/floating potential probes capture fluctuations. The next few sections describe the Langmuir probes, electronics, and the probe stands. A quick summary of other working diagnostics is also given.

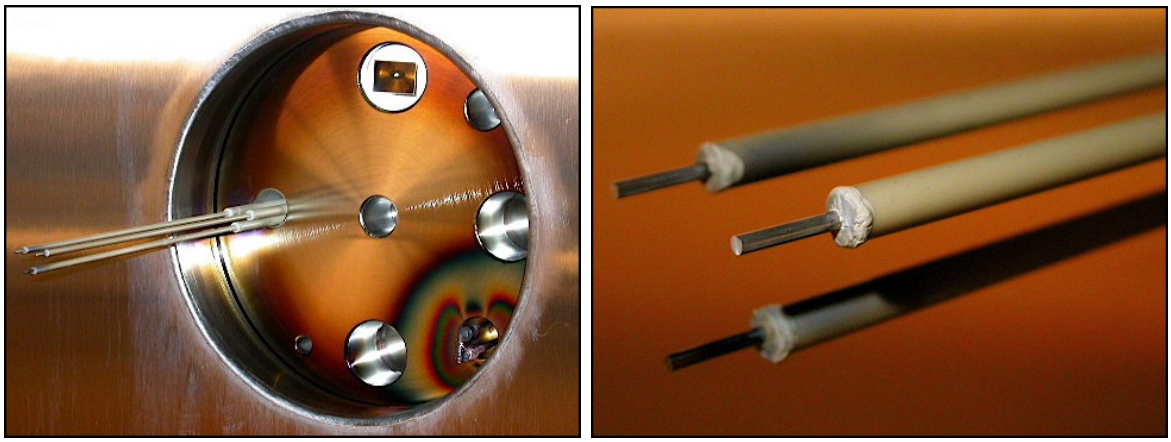

Figure 2-8: The first three Langmuir probes on LDX are shown above. They enter the vessel at the mid-plane and from a head on view are: top left – a fixed voltage probe to collect ion current, top right – a swept probe to collect both ion and electron current for the purpose of I-V analysis, and bottom – a high impedance floating potential probe with a 50 kΩ resistor in series (not shown).

Swept Probes

Swept probes are used to collect both positive and negative current from a biased probe in a plasma. The collected current can then be plotted versus the applied voltage to obtain the I-V characteristic curve. This plasma I-V characteristic curve varies depending on the type of probe tip (i.e. cylinder, sphere, planar) used, but in general has the same form as is depicted in many basic plasma physics diagnostics books [7, 25, 38]. For LDX plasmas, the most important regions of the curve are the flat ion-saturation current and exponentially changing characteristic regions. The study of these regions (after a making a few assumptions) yields an edge electron plasma density and temperature. The theory behind these calculations is also documented in the texts above and will not be repeated here. Instead, a description of the components used to capture the swept probe data is given and an overview of the processing of such data to yield the desired equilibrium parameters is presented.

The components used to operate this type of probe are: an amplifier, an adjustable wave-form generator, a data processing electronics board, and a digitizer. The amplifier is a Kepco 4-quadrant 400 W BOP (model number BOP 100-4M) power supply. BOPs are high speed power operational amplifiers that can be used to replicate arbitrary AC waveforms. The wave-form generator produces a saw-tooth wave with a low sweep frequency (< 20 kHz) that is set as the input to the BOP amplifier. The amplification factor is 10 and the BOP has enough power to run several probes. A wave can also be dc offset to sample a greater negative voltage range and obtain a more accurate measure of the ion saturation current.

LDX adapted the design from the Alcator CMOD Langmuir probe board to operate in LDX plasmas [17]. Built into this board are several modes of operation that can be remotely set. The modes are selected manually using seven logic inputs. Two logic inputs are used to select the sweep voltage source since up to three sources can be connected. A third logic input allows the board to by-pass all voltage sources and be used to measure floating potential. The fourth logic input is used to put the board in calibration mode. Three more logic inputs are used to select the resistor pair value used to determine the collected probe current. On the original Alcator boards these resistor pairs changed the measurable current sensitivity scale by an order of magnitude. For LDX, a new set of smaller resistor pairs means that the sensitivity scale changes by less than an order of magnitude, see Table 2.3. This change affects the overall board circuit in such a way as to allow a tiny amount of leakage current. It turns out that this leakage current is not an issue for swept probes but is an undesirable

effect for probes operating in floating potential mode.

The board outputs are un-calibrated values of probe tip voltage and collected current. The calibration for the probe tip voltage output is the factor 20. To obtain a calibration for collected current the board calibration mode was used. This was done by obtaining the I-V characteristic for a high-precision 2 kΩ resistor, built into the board. Calibration of the collected current output is then determined from Ohm's Law. The values for the two resistor pairs most commonly used during LDX experiments are given below in Table 2.3.

Resistor Pair	Input Logic Mode	Calibration Factor
10 kΩ	1 0 0	-1 / 601.940
100 kΩ	1 1 0	-1 / 98.569

Table 2.3: Calibration values and board selection logic for the Langmuir probe board's collected current output. The probe tip voltage output calibration is the factor 20.

Data collection occurs using four transient recorders (TR10) built by INCAA Computers. This digitizer set has 64 channels and is capable of sampling at 16 bits up to 200 kS/s per channel. By choosing the data collection rate, number of points per sweep, and voltage scale resolution, a limit is set on the sweep frequency. For example, for data sampled at 200 kS/s, with at least 100 points (per sweep), and enforcing a 1 V resolution on the V scale, an upper limit of 1 kHz is set for the sweep frequency. This means that if the voltage is swept from –50 to 50 V the I-V characteristic curve for that sweep would have 100 points on it in equal 1 V intervals. Through experiment it has been determined that between 75 and 100 points per sweep adequately capture the exponential and ion-saturation regions of the plasma I-V characteristic curve. The actual values chosen for LDX are the following: 200 kS/s, 1.125 kHz sweep frequency and a range of –50 to 40 V. In a 4 second shot (typical of LDX) nearly 10^4 I-V curves can be produced!

Analysis of each individual I-V curve is not always practical. For simplicity it is good to assume that the plasma is homogenous and quasineutral in the absence of the probe, electrons and ions have a Maxwellian velocity distribution with temperatures of T_e and T_i (with $T_e \gg T_i$), the mean free paths of electrons (λ_e) and ions (λ_i) is large compared to the relevant probe length, and each particle hitting the probe is absorbed and does not react with the probe material [38]. Unfortunately, in practice these are not always true over the period

of a single sweep. Collected swept probe data often shows curious behavior uncharacteristic of the typical plasma curve. To alleviate this problem an averaging technique is applied over a few I-V curves that smoothes out the irregularities and the data can then be interpreted using the assumptions above. This averaging technique reduces temporal resolution but still yields an adequate data set from which equilibrium plasma results can be obtained.

Analysis of swept probe data on LDX is done as follows. The data is averaged over five sweeps and the ion saturation current is taken as the current value when V_{probe} = –50 V, (sometimes it requires extrapolating from a fitted curve of the ion saturation region). The ion saturation current is then subtracted from the entire characteristic leaving behind the electron current (I_e) to the probe (as given by the thermal equilibrium value for an isotropic velocity distribution) with a $1/T_e$ exponential dependence. If the electrons have a Maxwellian distribution the slope of the logarithm of I_e is constant about the characteristic region of the I-V curve yielding a measure of T_e. The density may be determined from the equation for the ion-saturation current drawn from the probe [25, 38]. Values in standard SI units for the electron density, pressure, temperature, ion-saturation current and floating potential are calculated and written back into the tree.

Ion Saturation Probe

An ion saturation probe is a fixed voltage Langmuir probe that has been biased at a large negative voltage. The negative potential on the probe limits the flow of electron current and collects ions. This type of probe is ideal for studying density fluctuations which would otherwise be missed by a swept probe. On LDX biasing occurs using a Xantrex XFR 1200 W programmable dc power supply (maximum of 150 V and 8 A) and a probe circuit identical to that of the swept probes above.

High Impedance Probe

Langmuir probes with high (r_1 = 50 kΩ) impedance resistors attached in series near the probe tip are used to study electrostatic fluctuations, see Figure 2-10. These high impedance probes measure the floating potential of the plasma and special amplifiers increase the gain of the circuit to the digitizer scale. The stand-alone low-noise amplifiers (ZFL-500LN-BNC) are made by Mini-Circuits and work well for this purpose given their low (r_2 = 50 Ω)

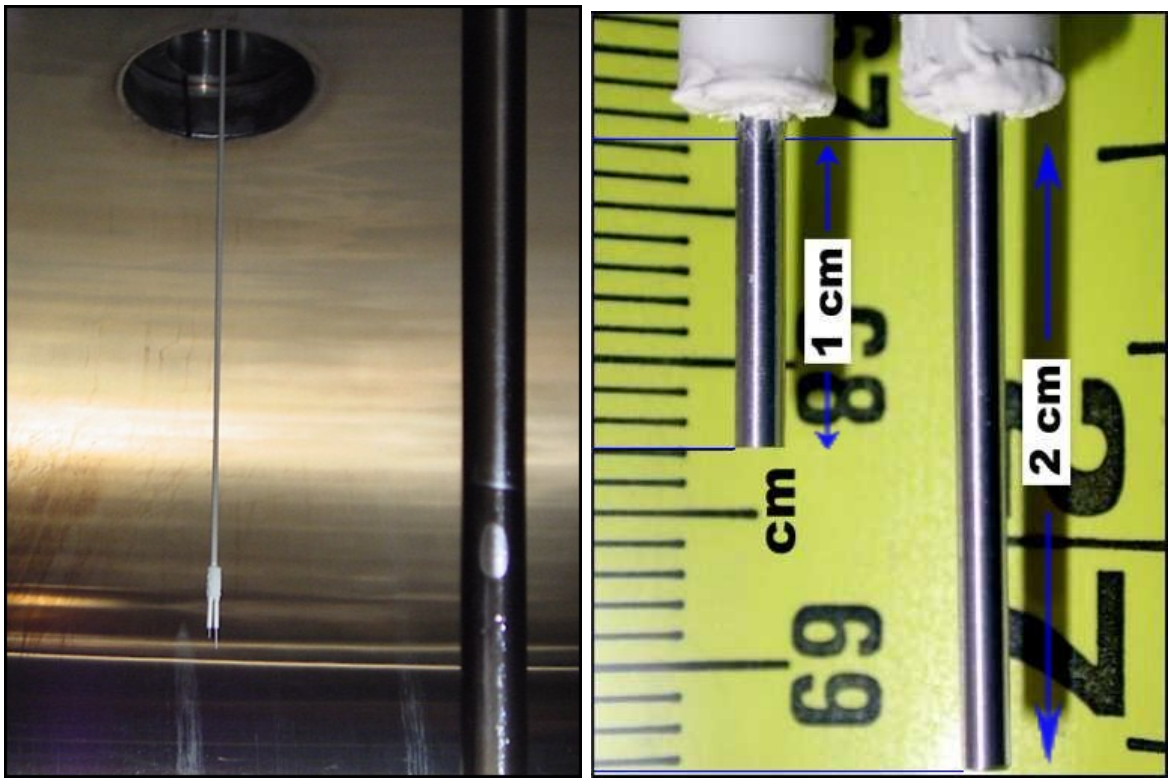

Figure 2-9: These first generation probe tips are long and narrow as shown above. These two probes perform separate functions. The shorter probe is swept while the longer probe has a 50 kΩ resistor in series and measures V_f.

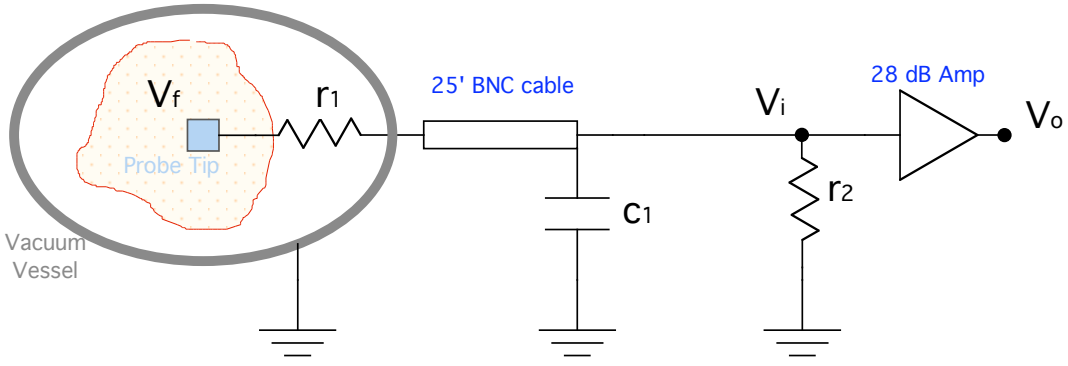

Figure 2-10: The circuit for the high-impedance floating potential measurements is shown above ($r_1 = 50$ kΩ, $r_2 = 50$ Ω, $C_1 \sim 450$ pF).

input impedance. The frequency range of these amplifiers is .1 to 500 MHz and the factory calibration curve for the amplifier shows a 28 dB power amplification for $f_{V_f} > 100$ kHz. Individual amplifier calibration curves performed in the lab can be found in the Appendix.

Analysis of the circuit in Figure 2-10 shows that the input voltage to the amplifier will be reduced by a factor of 1,000 for frequencies around 1 MHz. To obtain the calibration factor for the digitized signals the amplifier gain (28 dB power) must be included in the circuit analysis and this yields for a 1 MHz signal a total reduction factor of 1/40. In practice, a 5 dB attenuator is also used to protect the amplifier but this makes the reduction factor 1/70.

Mach Probe

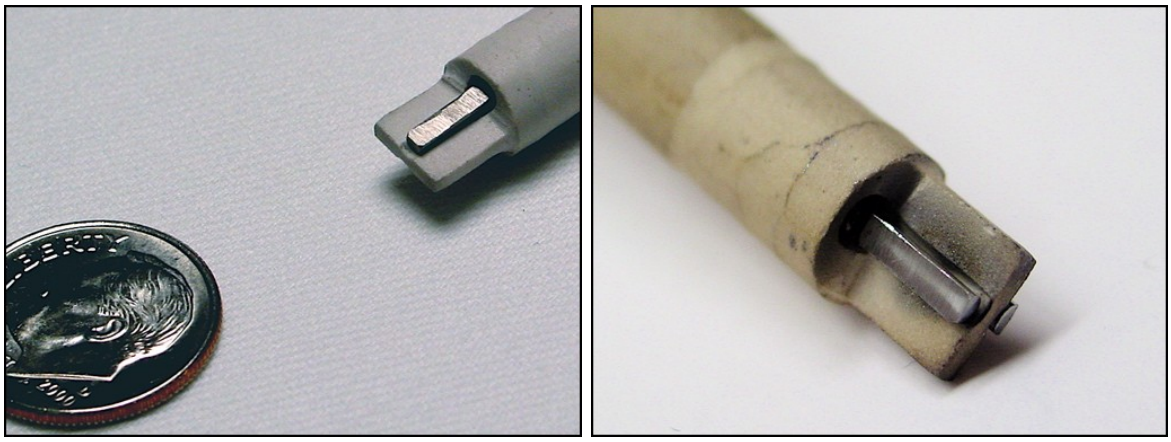

Figure 2-11: A mach probe was available during the 2004 runs. To the left we have the probe as it was before operation. On the right is the probe after it was removed in March 2005 displaying the effects of three effects of plasma exposure.

A Mach probe consists of two swept Langmuir probes separated by an insulated tip, see Figure 2-11. It can measure the differential plasma flow velocity because one of the probe tips measures the upstream current and the other one measures the downstream current. If a Maxwellian velocity distribution is assumed, the upstream probe will measure a higher current relative to a stationary plasma and vice versa for the downstream probe. As expected the downstream electrode collects less current. A comparison of the upstream and downstream currents determines the plasma velocity. The Mach number is simply the

natural log of the ratio of the two currents,

$$M = A \cdot \ln\left(\frac{I_{up}}{I_{dn}}\right) \tag{2.1}$$

where is A is a constant typically quoted as 1/2 [18, 24, 25].

2.2.2 Probe Motion System

The probe motion system is used to linearly reposition a single probe. It is composed of a probe stand, bellow, gate valve, motor, limit switches and optical encoder, see Figure 2-12. Depending on the orientation of the stand (vertical or horizontal) a probe tip can select a specific flux line near the plasma edge. Movement and positioning is controlled via a ladder logic PLC program and graphical user interface. The system is designed for motion in-between plasma shots but not during a shot.

Four probe motion systems have been built and installed on LDX. Three of these systems stand vertically on the upper 10 inch diagnostic ports. They are separated by 45° and each probe enters at $r = 136\,\text{cm}$ from the center of the vessel. The linear vertical motion can span a chord 30 cm long within the last closed field line of an F-coil only (supported mode) dipole plasma. Access to the plasma depends on the magnetic configuration. During a levitated shot, the outer closed field line moves closer to the top probe entrance port and therefore the span will be greater. The fourth probe enters horizontally on the NE lower mid-plane port. It is aligned with one of the vertical probe stands and is positioned below the midplane at $Z = -62\,\text{cm}$. This probe motion system has a longer bellows and greater access into the chamber or approximately 60 cm horizontal chord in from the last closed field line.

2.2.3 Additional Plasma Diagnostics

Additional plasma diagnostics include an interferometer, flux loops, Bp coils, Hall Effect sensors, a 4 channel X-ray PHA (pulse height analyzer), X-ray detector, hard X-ray camera, single visible diodes, multi-diode array, video cameras and Mirnov coils. Early results from several of these diagnostics are still being interpreted. This section describes those diagnostics which have contributed to supporting the conclusions of this thesis.

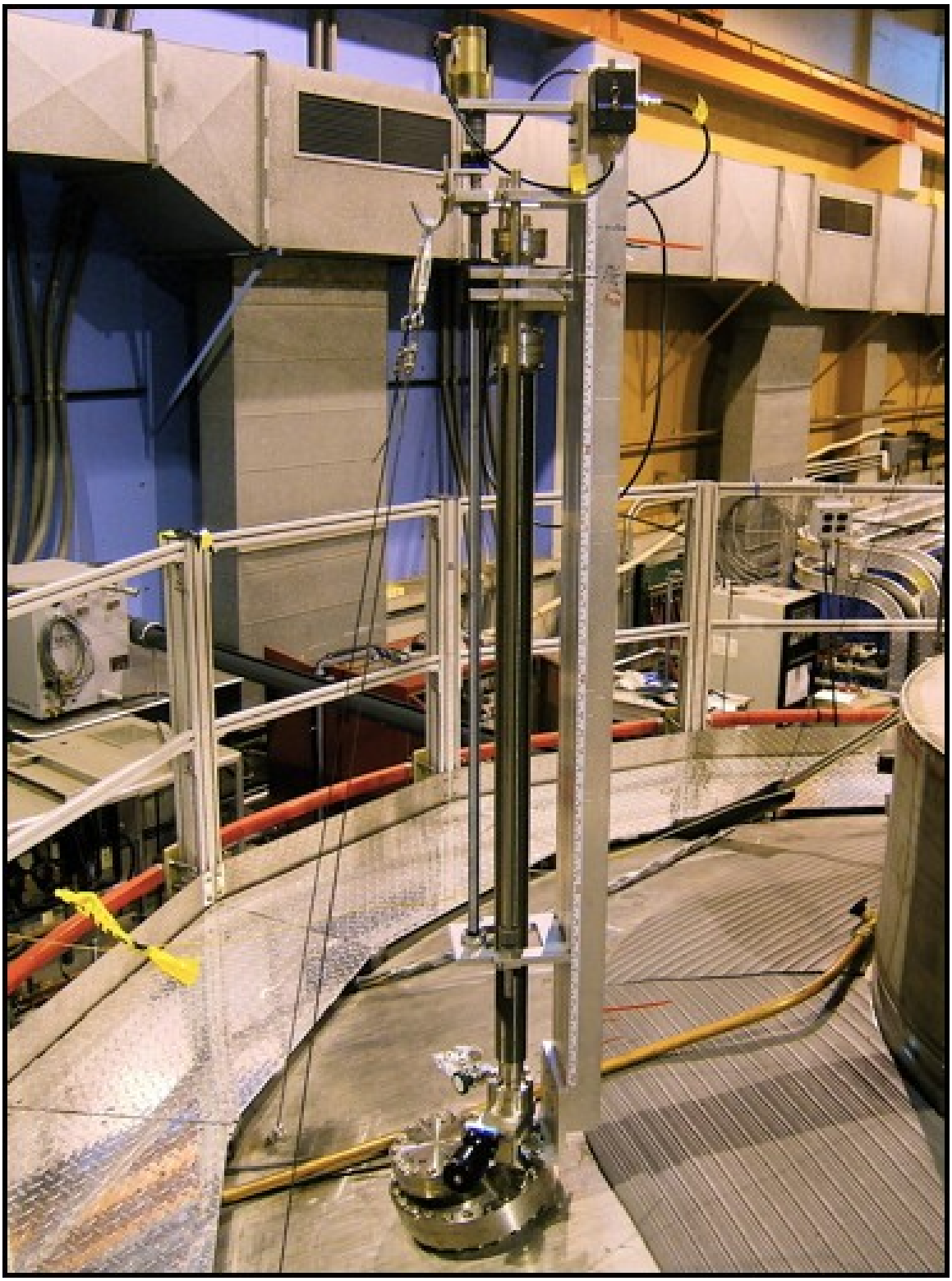

Figure 2-12: The probe motion system on LDX enables computer controlled linear motion. The stand is designed to allow in situ replacement of a probe tip without breaking the main vessel vacuum.

Magnetic

Eight magnetic flux loops and 16 Bp-coils, 8 $\perp$ and 8 $\parallel$ to the wall, have been installed along the outside of the vacuum vessel. Their positions have been optimized to yield the most sensitive information about the plasma equilibrium. Reconstruction of this equilibrium is a complex process and the topic of Karim's thesis [27]. The strongest signals are used in this thesis to compare magnetic data to other diagnostics. These correspond to flux loops labeled 5 and 7, and Bp coils labeled 2 and 5.

Eddy currents are excited by rapid changes to the plasma magnetic current. The estimated decay time for these eddy currents is 28 milli-sec. Unfortunately, these currents limit the Mirnov coil's ability to capture transient behavior during a major instability event. For LDX analysis to remove these eddy current affects from the magnetic signals has been done and is presented in the section 5.1.1.

Two Mirnov coils are used to study the transient behavior of the B-field during an instability. They are located inside the vacuum vessel and are separated by 45° and for the purpose of this study labeled 2 and 3. Eight mirnov coils will eventually be installed and equally spaced around the inside wall of the vacuum vessel.

Light Diagnostics

Two types of devices are used to detect the light emission from the plasma. The first device is a video camera. LDX has three video cameras operating during the shot. Two are black and white and fed directly directly to a computer and the third is a handheld color video camera. This last one records the entire run and the film is parsed and converted to movie files for storage in the main data computer. The second device is a photo diode. Two photo diodes have a broad view from the side and bottom visual ports. Additionally, a collimated photo diode array is also installed. This diagnostic has sixteen chords radially distributed starting at the F-coil edge. An Abel inversion of the video camera signals together with a correlation of the photo diodes has been used to identify important steady-state LDX plasma characteristics. Some of these results are presented in chapter 5.

X-ray Diagnostics

A single channel NaI (sodium iodide) hard X-ray detector has been used to detect bremsstrahlung in the plasma. It has an energy range of 10 keV–2 MeV and the electrical output is proportional to the X-ray intensity. The viewing chord of the NaI detector runs 10 cm off the F-coil shell. Occasional bursts of X-rays are used to trigger a window for fast digitizer measurements of the HEI instability. In addition, a video camera (on loan from PPPL) has observed anisotropy of the plasma. The camera itself is made up of a CsI (cesium iodide) crystal which converts X-ray photons to visible light. A special coating on the back side of the crystal converts this visible light to photoelectrons which are then electrically focused, intensified and imaged onto a 25 mm diameter phosphor display. The display is then filmed by a monochromatic CCD camera and digitized at 30 fps [11].

Interferometric Diagnostics

To measure the density of the plasma a single-channel microwave interferometer has been installed. It is a heterodyne interferometer with a center frequency of 60 GHz and with phase-shifts measured in quadrature. Future work will include adding three more channels to this system to obtain a density profile.

In addition a radiometer has been installed to detect the microwave radiation emitted by the plasma. The radiometer is composed of two parts: a V-Band (50–75 GHz) standard gain horn pointed at the F-coil and located on one of the side vacuum vessel windows and a crystal diode detector that converts the received microwave power to a measurable voltage.

2.3 Summary

The LDX experimental device consists of three circular and co-axial superconducting magnets (C-coil, F-coil and L-coil), a large cylindrical vacuum chamber, a glow discharge cleaning system, two microwave ECRH systems, and several plasma diagnostics. Experiments to date have achieved a high beta plasma during supported mode. They have also been used to develop the cryogenic procedures for the charging and discharging of the F-coil, demonstrated the performance of the ECRH power systems, tested the vacuum and puff systems, and verified the operation of diagnostics in preparation for future levitation experiments.

Chapter 3

Production of High Beta Plasma

LDX is the first laboratory dipole experiment to observe and sustain high beta plasma. This has been achieved at various dipole current levels. In addition, experiments have shown that creation of high pressure, high beta plasma is possible only when intense hot electron interchange (HEI) instabilities are stabilized by sufficiently high background plasma density. Results from initial experiments are reported here. Long-pulse, quasi-steady state microwave discharges are described that last more than 10 seconds and having peak beta greater than 20%.

3.0.1 LDX Plasma Regimes

Experiments show LDX plasma exist within one of three plasma "regimes". In most plasma discharges and when the neutral pressure is properly adjusted, the plasma state evolves in time and transitions occur between all three regimes. One example discharge is indicated in Figure 3-1. As indicated by the respective roman numeral these three regimes are: (i) an unstable low beta regime that results from under-fueling, (ii) a stable high beta plasma regime with occasional small relaxation events, and (iii) a quiescent afterglow that can last for many seconds when the ECRH power is switched-off. Each regime is characterized by how the plasma behaves in response to heating and fueling. For heated plasmas, hysteresis is observed in the transitions to and from high and low density regimes, a topic to be covered in chapter 5. The following summarizes the main characteristics of each regime.

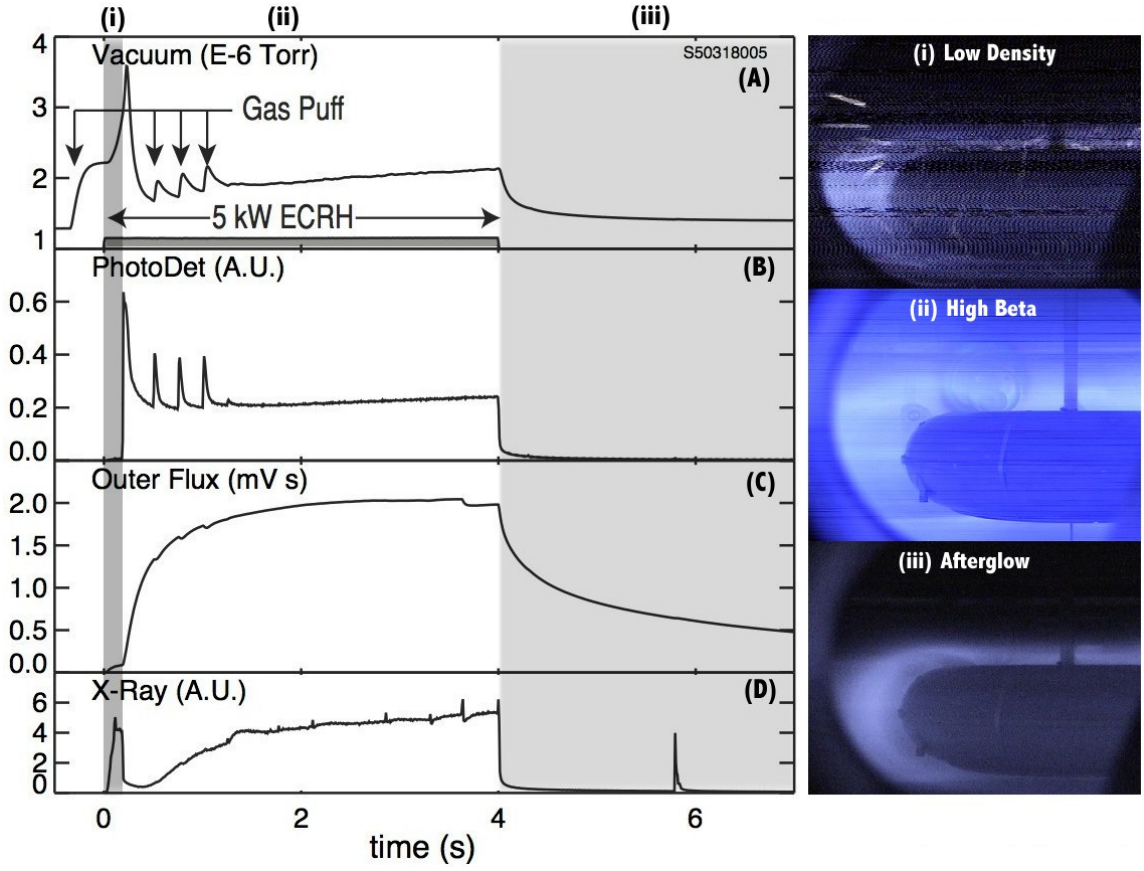

Figure 3-1: Example of a high beta plasma discharge created with 5 kW ECRH power and four gas puffs. From top to bottom the measurements shown are: (A) the deuterium background pressure, (B) light emission, (C) mid-plane diamagnetic flux, and (E) X-ray intensity. Shading distinguishes three operational regimes: (i) low density, (ii) high beta, and (iii) afterglow.

Low Density Regime

The low density regime (LDR) can be established and maintained by continuously underfueling the experiment. This occurs at a low vacuum pressure ($< 2 \times 10^{-6}$ Torr) and with properly conditioned vessel walls as discussed in chapter 2. It is characterized by small diamagnetism (~ 0.1 mV·s) and line-average density ($\sim 2.3 \times 10^{10}$ cm^{-3}). By viewing the dipole magnet from several directions it has been determined that X-rays result from plasma bremsstrahlung and from fast electrons driven inward to the dipole magnet. In addition, outward radial transport is observed from an electron current to a negatively biased probe ($V_{bias} = -150$ V, normally used to collect positive current for ion-saturation measurements) located at the outer mid-plane wall, see Figure 3-2. Visible light images show light emission as localized to the equatorial plane indicating the formation of a "disk" of deeply-trapped energetic electrons.

Analysis of high-speed data collected from electrostatic floating potential probes reveal frequencies resonant with the magnetic drift frequency of electrons in the energy range of 20–60 keV. Similar observations were previously detected using the Collisionless Terrella Experiment (CTX) [35, 41, 42, 57] under similar conditions. These fluctuations were identified as the low frequency HEI instability. During the LDR, dust and material scatter from the F-coil and/or F-coil supports. This has been associated with the quasi-continuous presence of the HEI instability forcing energetic plasma towards the F-coil and causing the 'sparks' seen in video images similar to the "Low Density" image in Figure 3-1. The X-ray data, ion-saturation probe data, and visual images all show that the LDR suffers from nearly continuous pressure driven instabilities which cause rapid inward and outward radial transport of energetic electrons. This observation is in agreement with studies conducted on the CTX.

High Beta Plasma Regime

The high beta plasma regime (HBPR) follows the LDR and is characterized by a large diamagnetic plasma current, typically 10–20 times larger than that found in the LDR. An equatorial outer diamagnetic flux detector senses 0.78 mV·s/kA for a current ring located at a 1 m radius, Figure 3-1 indicates several kA of equilibrium plasma current. The buildup of this diamagnetism takes about half a second but depends greatly on the fueling, vessel conditioning, and ECRH heating profile chosen. One constant appears to be the level of neutral

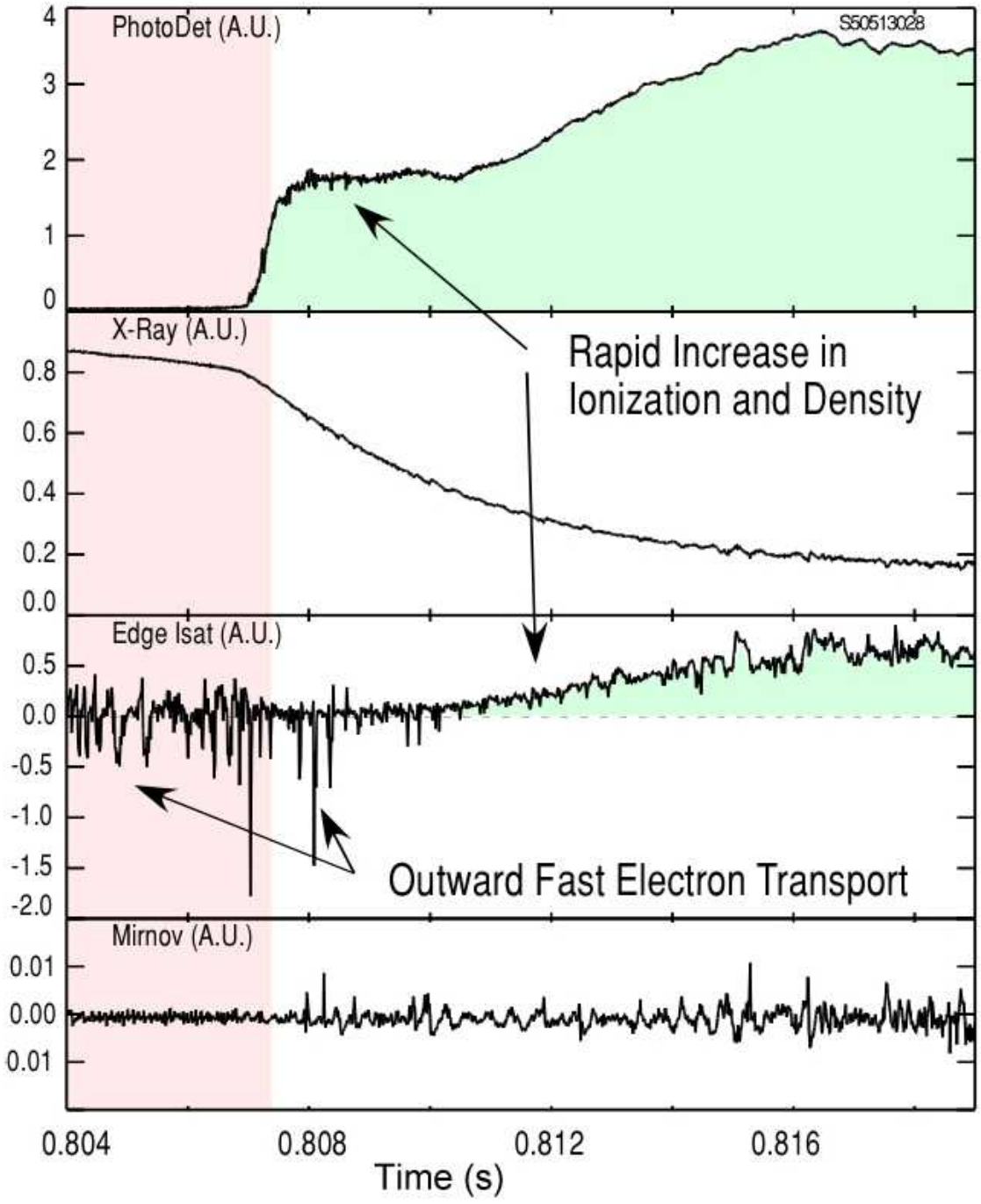

Figure 3-2: Close up example of the LDR shaded in pink. The entrance into a HBPR is marked by a rapid increase in density which is reflected by the accelerated increase in ionization seen on the photo-diode and gradual transition of the Edge Isat probe from negative to positive current.

gas pressure required for the transition to occur. A critical level of 2.5–3.5 μTorr of puffed deuterium gas has been observed for the most productive and highest beta experiments. The neutral gas pressure required for the transition increases with the level of microwave heating applied, although no obvious relationship has been found. Video images show that high beta plasmas do not cause 'sparks'. The three F-coil support rods become warm and glow, an indication that power deposition to the support rods increases during the HBPR.

The transition from LDR into a HBPR occurs whenever the deuterium pressure exceeds a threshold dependent upon the level of microwave heating power. A steady increase in neutral fueling past this critical point typically causes a rapid transition to occur. In a few milli-sec the LDR characteristics disappear. A bright flash lasting about 10 milli-sec preludes the event and coincides with the ionization of the background neutrals. Plasma density also increases an order of magnitude from what is observed in the LDR. The edge density probe measures a positive current and is no longer bombarded by energetic electrons as was the case in the LDR. The target X-ray intensity decreases by an order of magnitude consistent with a reduction of inward energetic electron flux to the F-coil. Floating potential probe measurements show that the pressure driven instability is stable after the transition into the HBPR. However, a related and more intense pressure driven instability may still result if the neutral pressure falls below a threshold.

The HBPR is grossly stable when compared to the LDR. However, infrequent and relatively short bursts fluctuations occur at a rate determined by the level of neutral fueling and microwave power [13]. Figure 3-1 gives a perfect example of how these small bursts are seen on the X-ray intensity signal and are sometimes accompanied by small drops in diamagnetism (t = 3.5 s). High beta plasma remain close to marginal stability and keeping it stable requires relaxing the pressure gradients and avoiding the high beta version of the previously mentioned instability. In addition, a lower frequency mode has been detected. It is typically below 5 kHz and not associated with radial transport.

Afterglow

After microwave power is switched off, the plasma evolves to an afterglow regime. With sufficient neutral pressure, this regime has been observed to last as long as 20 seconds. The background plasma density decays within 10-15 milli-sec. This fast decay of plasma density, as measured by the edge probes, indicates that a significant fraction of the injected power

goes into maintaining the density of the cooler background plasma.

The energetic trapped electron population decays much more slowly ($<$ 20 seconds), consistent with the pitch angle scattering rate of deeply trapped electrons. The concurrent slow decay in diamagnetism suggests that the bulk of the stored energy is contained in the energetic electron population. The superposition of an X-ray camera image over a video camera image (Figure 3-6) indicates that the energetic electron population is radially localized in the vicinity of the fundamental ECRH resonance. It is also vertically localized to the mid-plane, implying a significant anisotropy. Very intense fluctuations may appear depending on the level of neutral pressure in the afterglow.

3.1 Equilibrium Plasma Parameters

Langmuir probes operated using a sweep voltage power supply have been used to measure global plasma parameters just inside the confined plasma edge. The probes operate as expected during the HBPR, but fail to yield any useful information during the LDR due to high levels of noise produced by the large fast electron incidence on the probe. Values of 5 to 25 eV, –2 to –40 V, and 0.5 to 2.5 $\times$ 10^{10} particles per cm^{-3}, are measured for the HBPR electron temperature, plasma floating potential and plasma density, respectively.

This section explores three important experiments performed to measure equilibrium plasma parameters. First a probe scan is presented that attempts to capture radial information about the edge plasma. The plasma space potential (V_s) is related to the floating potential (V_f) and electron temperature (T_e) measurements according to Hutchinson [25],

$$V_f \approx V_s - 4.03\ T_e/q, \tag{3.1}$$

and shows that the plasma has a net positive charge relative to the vessel walls. Next probe density measurements are compared to interferometer line-average density measurements. Favorable agreement exists between the two diagnostics. In particular the piqueness, or ratio between these two density measurements, is consistent with expected plasma behavior for the different regimes. Finally, Mach probe measurements detect clockwise ion flow during the HBPR and can be explained by an outwardly pointing electric field near the confined plasma edge.

3.1.1 Probe Scan

A radial scan that measures equilibrium plasma parameters has been made on a high beta LDX plasma by adjusting the top moveable probe position over the course of five experiments. Data was collected along a vertical chord sampling different flux lines. Measurements from a fixed reference probe located at R = 220 cm (L = 3.86) are also included to show good experiment-to-experiment consistency during the scan. The results of the scan are presented in Figure 3-3 where the vertical flux line location has been mapped to the mid-plane and the corresponding R coordinate (and L-value [43]) has been used for easier interpretation of the results.

In Figure 3-3 each plot represents a different background plasma parameter during the scan. From top down the plots show the calculated plasma density, electron temperature, plasma space potential according to Equation 3.1 and the probe floating potential. Notice that the probe scan results are presented using a red line and the corresponding fixed reference probe measurements are shown as black circles. The fixed probe measurements were all taken at the same radius and should therefore all lie at that point, R = 220 cm. They are plotted relative to the probe scan R-axis measurements to conveniently show that although all experimental conditions were held constant, small experiment-to-experiment differences exist for each parameter. However, these differences are not large enough to prevent a global comparison of this probe scan.

The first plot at the top shows that the plasma density increases the further inwards the probe is moved. LDX therefore has a centrally peaked plasma density profile consistent with the ECRH heating mechanism used to transfer energy to the electrons at the resonance peak, R $\sim$ 75 cm (L $\sim$ 1.32). The second plot from the top shows the background electron temperature decreasing as the probe is moved outward. T_e is 11 eV well inside the outer plasma edge and drops down to 6 eV near the vessel wall, R = 250 cm (L = 4.39). The analysis of raw data that obtains these values assumes that the electrons are in thermal equilibrium. This in general is not true for LDX and therefore these measurements are very sensitive to the presence of fractional hot electron ($>$ 10 keV) components. We therefore consider these results more as upper limits to the actual background electron temperature. To fully nail down the actual background temperature additional diagnostic measurements can be combined. Spectroscopy and gridded particle detectors can give further insight on the types of ions and the fractional density of hot electrons contributing towards the background

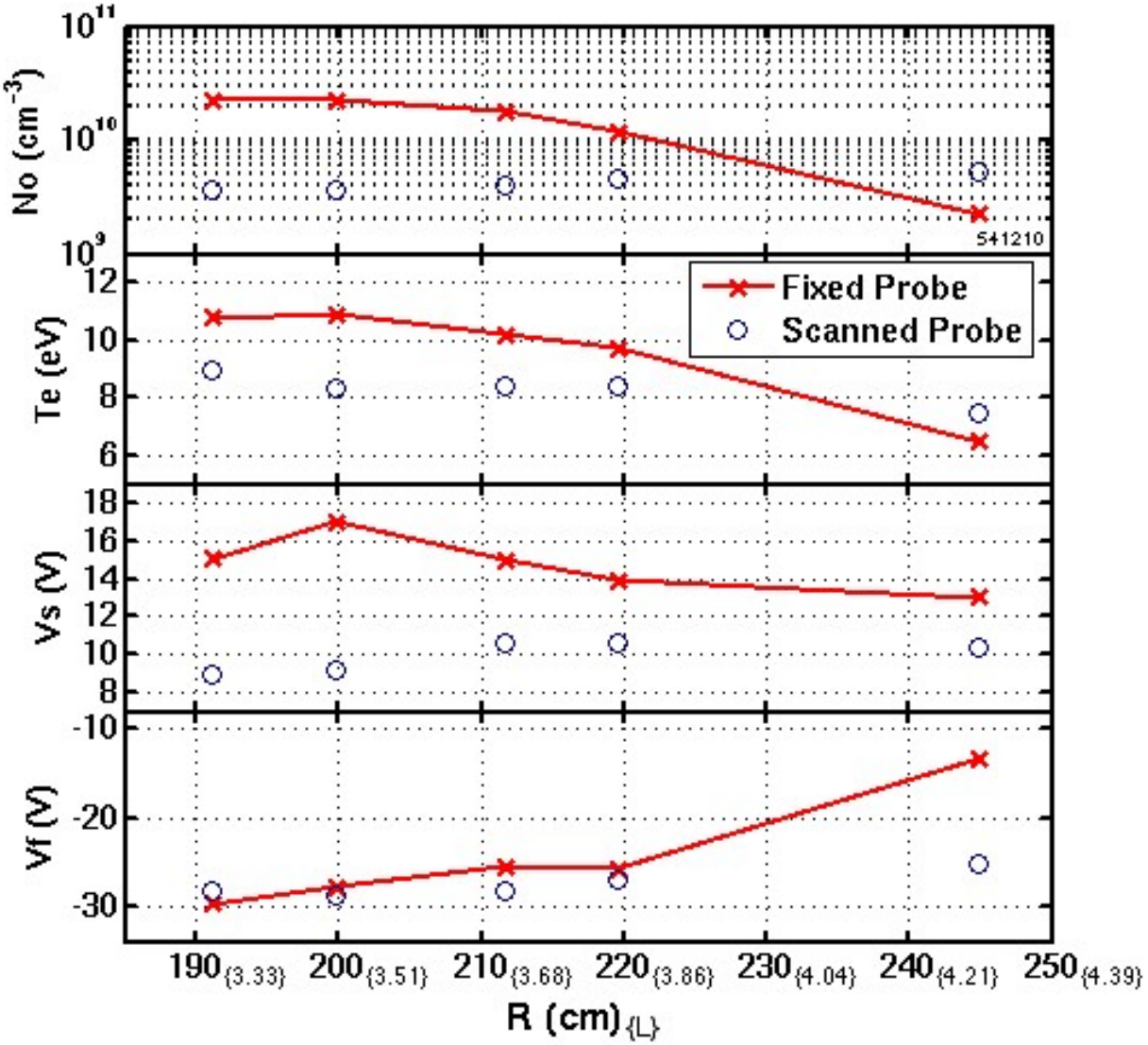

Figure 3-3: A probe scan reveals equilibrium plasma parameters near the edge. The vessel wall is located at R = 250 cm (L = 4.39 cm). The Fixed Probe results are also included to show a relative consistency over the five experiment probe scan.

numbers stated above. No independent confirmation of these values currently exists for LDX.

The third and fourth plots from the top display the plasma space and probe floating potentials, respectively. The first is derived from the probe floating potential and electron temperature measurements. As expected the floating potential is a negative value due to the higher mobility of the electrons assuming $T_e \geq T_i$. Also, a positive space potential shows that the overall net charge of the bulk plasma is positive relative the vacuum chamber walls. This makes sense again because of the higher mobility of electrons. The electrons tend to escape to the chamber walls at a faster rate than the ions. The result for the plasma is a slow increase in the net positive charge. As the plasma charges positively it becomes less energetically viable for the electrons to leave because the walls of the chamber are more negative than the plasma. Eventually, a steady state condition is reached in which the plasma potential is high enough that the loss rate of electrons decreases to the same level of ions. In this way the plasma retains its overall neutrality. The space potential plot also shows an outwardly decreasing space potential corresponding to an outward electric field present in the plasma. We will return to this point under the Mach probe results section.

3.1.2 Interferometer Density

A key characteristic of any plasma is density. Interferometers are great unobtrusive tools used to probe the line-average density of the plasma. For more localized measurements swept Langmuir probes work well but are limited by the physical characteristics of the probe and by the plasma characteristics as discussed above. Therefore, comparison of the two methods offers an improved measure of the density profile of a plasma and is common practice in plasma experiments whenever possible.

For LDX probes measure the density of the edge plasma during the HBPR without any problems, but fail to yield consistent values during the LDR and afterglow regime. On the other hand, the interferometer has been able to detect a line-averaged density in all three regimes, albeit, with mixed success. For this reason there are only a few experiments (to date) where the interferometer and probe density measurements can be compared. The following describes an example of such an experiment taken in the December 2004 campaign.

A comparison of the line-average density and edge probe density as well as the photo diode light and vacuum pressure is shown in Figure 3-4, and represents a case where all three

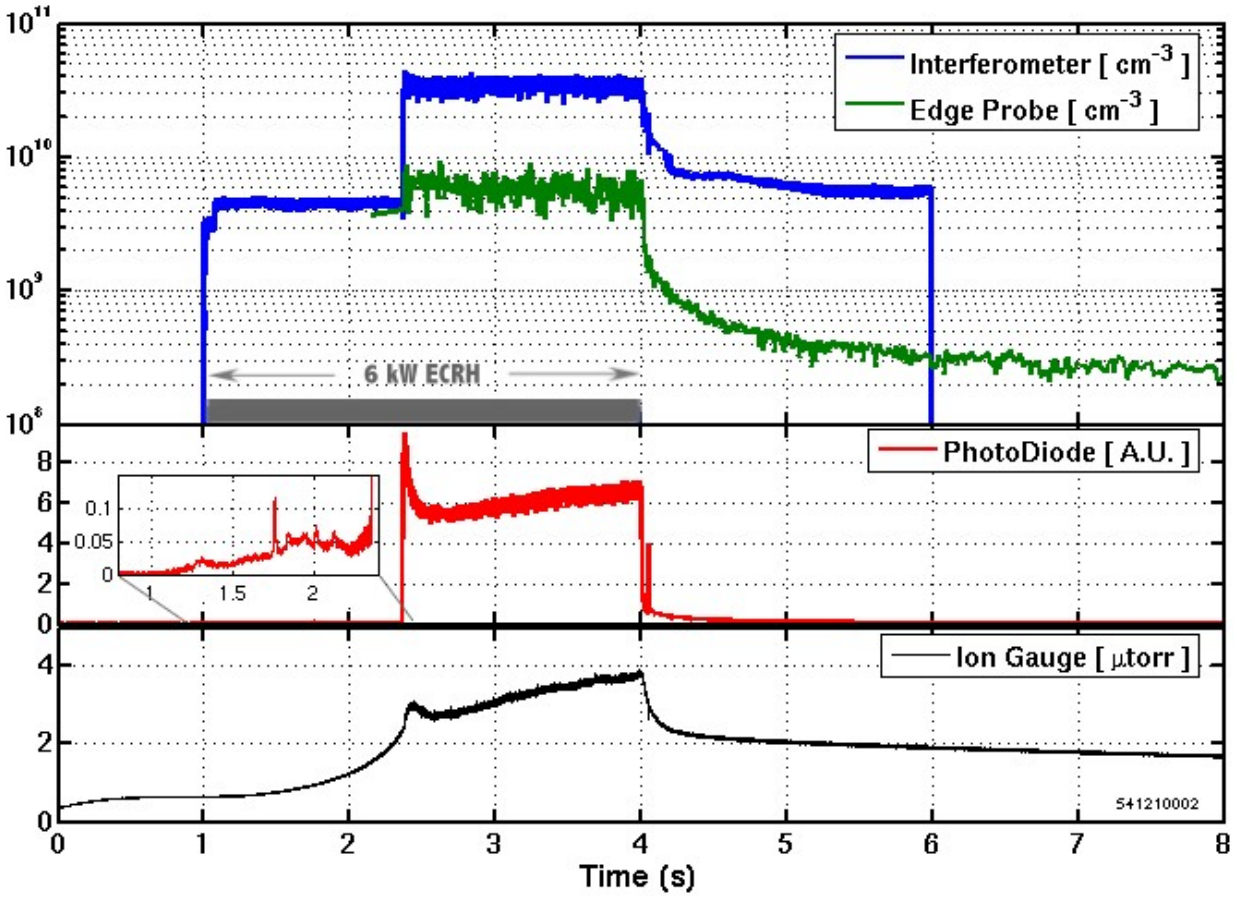

Figure 3-4: The interferometer's measure of line-average density is roughly proportional to the edge probe and photo-diode signal. Although the edge probe does not measure a density before ECRH ($0 < t < 1$ s), the interferometer still shows a line-average density.

diagnostics worked. S41210002, as one of the first experiments of the day, initially has a low vacuum pressure. Just before puffing the pressure is 3×10^{-7} Torr and after a 3 milli-sec pre-puff, the pressure rises to 6.5×10^{-7} Torr. A total of 5 kW of ECRH power from both sources is applied from $1 < t < 4$ s. A low density regime exists during $1 < t < 2.36$ s, and although the probe does not yield a density measure, the interferometer detects a plasma density on the order of 4×10^{9} cm^{-3}. The signal detected by the diode, according to Chen *et. al.* [8], is proportional to the light emitted by the dominant background plasma which in turn is proportional to the density. The level of the light, although measurable, is an order of magnitude lower than that measured later in the experiment and suggestive of a low density plasma. Both the interferometer and photo-diode detect the plasma during the LDR.

Once the critical level of deuterium fuel pressure is reached ($t = 2.45$ s), the plasma enters a HBPR and remains in this regime until heating shuts off. In the HBPR the light signal spikes and so does the interferometer density measurement. After spiking the line-average density settles an order of magnitude (3.2×10^{10} cm^{-3}) above that measured in the LDR. The edge probe also measures density in this regime (6.3×10^{9} cm^{-3}) and the ratio of these two density measures, referred to as the peakness, during the HBPR gives a value between 5 and 8. The peakness decreases in time as the diamagnetic current increases. This relationship between the edge probe and interferometer indicates that the central peak density grows as the edge background density remains relatively constant.

All three probes detect the slow decay in plasma density in the afterglow. In this regime the interferometer density at first drops by a factor of two and then slowly decays away. A similar behavior is observed for the probe and diode. In this regime the peakness varies between 12 and 18, increasing as the background plasma decays. Again, this is consistent with the observation that the cold outer plasma re-combines first and the hot electron ring continues to create a warm plasma close to the F-coil where the interferometer can still measure a line-average density. It would be great to have multiple radial cords to interpret how the density profile changes in the afterglow and better correlate the interferometer line-average density to the edge plasma density as measured by the probe.

3.1.3 Mach Number

The Mach probe has been used to measure the bulk plasma flow just inside the last closed field line. In this region the E x B plasma motion dominates bulk particle flow. In LDX by definition the B-field at the outer mid-plane points downward and the E-field points outward near the edge based on probe measurements presented above. The drift is then counter-clockwise (looking top down), in the direction of the electron grad-B drift. This section summarizes the Mach probe measurements for the HBPR, provides further evidence of an outward pointing electric field, and discusses the observation of a negative Mach number only during the LDR.

The LDX Mach probe enters the vacuum chamber vertically through the top South-East diagnostic port. The ceramic wall was oriented parrallel to the magnetic flux field line and the South-West side is defined as upstream electrode. In this setup the Mach probe measures cross field plasma flow. With a counter-clockwise ion flow (looking top down), the upstream electrode should measure a higher current than the down stream electrode, *i.e.* a positive Mach number as shown in Equation 2.1. In HBPR experiments the Mach probe yields positive Mach numbers between 0.05 and 0.25 when the probe was positioned near the confined plasma edge, R = 245 cm. The electric field must point outward to account for this flow.

In Figure 3-5 two similar experiments are overlaid to compare the behavior of the plasma flow near the edge. ECRH heating using both the 2.45 and 6.4 GHz sources was applied at 5 kW from t = $[0, 3.6]$ and t = $[0, 7.2]$ sec during experiments S40917012 (red) and S40917021 (black), respectively. Another difference in experimental parameters was the level of deuterium pressure at the beginning of the experiments: 2.3 μTorr (red) and 4.9 μTorr (black). As explained before, low initial fill pressure led to the clearly visible LDR for experiment S40917012 (red) during t = $[0, 0.15]$ sec. Measurable equilibrium diamagnetic flux reached similar levels after about 1 sec and the ion saturation and photo diode results show that the volume density was higher for the experiment with only a HBPR. The Mach probe position for both experiments was the same, R = 245 cm.

The plasma for experiment S40917012 (red), see Figure 3-5, begins with a short LDR. The corresponding Mach number was –0.075 and is evidence of a small clockwise flow during the LDR. The electric field must point inward to account for this flow. In contrast, experiment S40917021 (black) begins in a HBPR and correspondingly has a positive steady state Mach

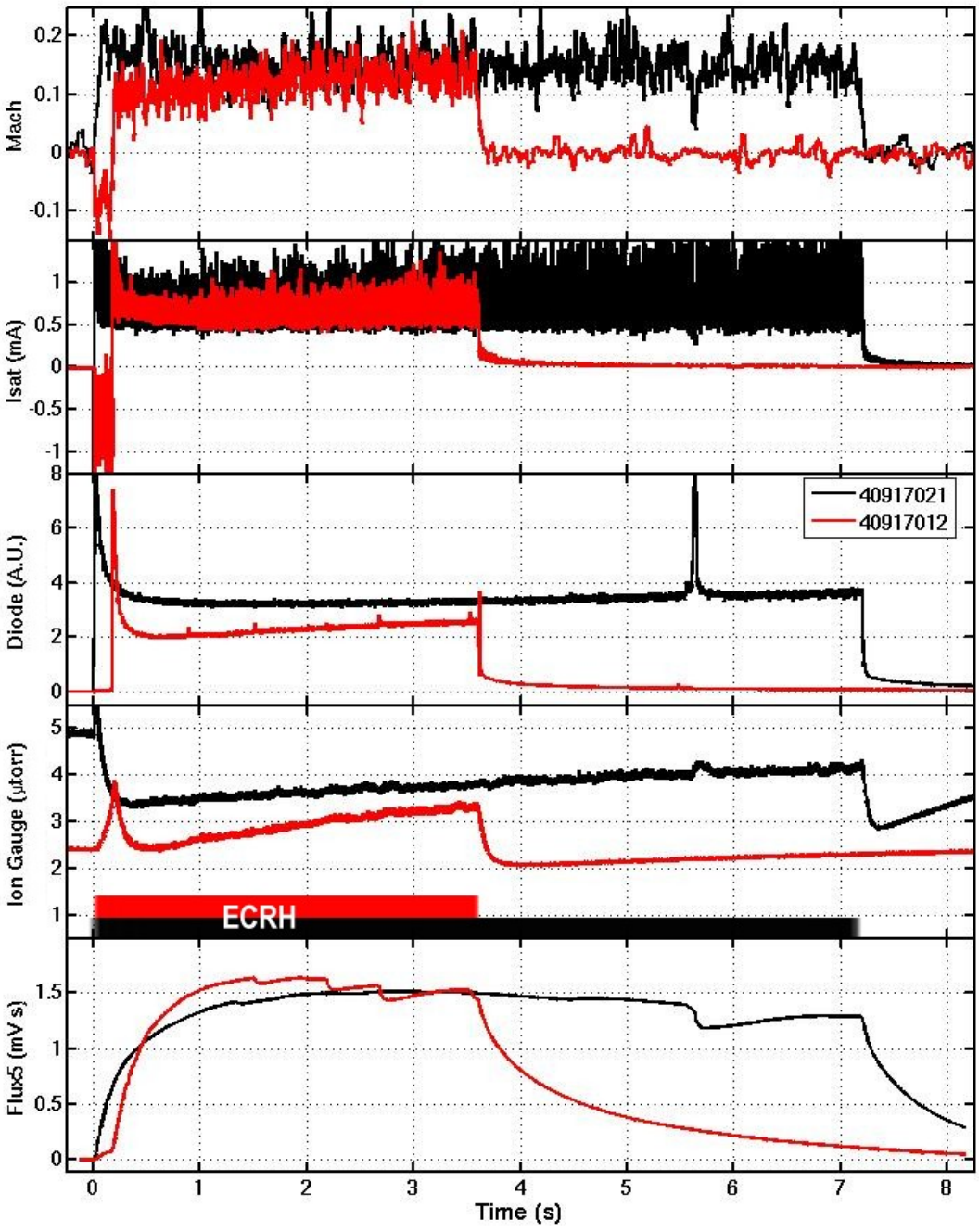

Figure 3-5: The Mach probe measures bulk plasma flow at the edge. Two experiments during the September 2004 run are shown above, S40917021 and S40917012. During the LDR in experiment S40917012, the Mach number was negative and quickly changes to positive as the plasma enters the HBPR (t = 0.18 s).

number value of 0.15. The brief event at t = 5.6 sec (this was a pressure relaxation event to be covered in more detail in Chapters 4 and 5) results in a temporary decrease in the Mach number. As the plasma recovers, so does the Mach number quickly returning to its previous HBPR steady state value.

3.2 Highest Peak Beta

Creating plasma that aims to maximize beta and diamagnetic current requires multiple-frequency ECRH heating and careful programming of the deuterium fuel puffing rate. The high beta current is mostly carried by a population of fast electrons, with mean energies above 50 keV, created by the ECRH power and localized to the resonance zone. Magnetic measurements of this current determine the value of beta achieved by a given experiment. An equilibrium magnetic reconstruction uses these signals to estimate beta for a given experiment.

Magnetic equilibrium reconstruction uses a simple model which takes into account the anisotropic diamagnetic current and uses a peaked pressure profile. This model holds the flux constant in the superconducting dipole and has four unknowns including: the peak pressure, peak major radius, profile steepness and anisotropy. The peak major radius can be approximated using X-ray camera images (overlaid to extract position from a visible camera image as in Figure 3-6) as these demonstrate localization and anisotropy of the fast electrons.

The LDX record high beta experiment (S50513029) was achieved using optimal gas fueling and a heating profile that combined both sources and avoided entering a LDR. To calculate the beta for this experiment the following parameters are set: a peak pressure radius fixed at 75 cm from the center of the chamber, a peak pressure estimate of 200 Pa, a measured edge pressure of 0.01 Pa, and an estimate of 5 for the anisotropy ratio. The magnetic equilibrium fit then gives a total energy of 330 J with 5 kW of input power. This yields an effective τ of around 65 milli-sec with a peak local beta of 20% [13].

3.3 Summary

LDX is the first dipole experiment to create and sustain high beta (peak local beta of 20%) plasma in the lab. Experiments discussed in this thesis have been conducted as long-

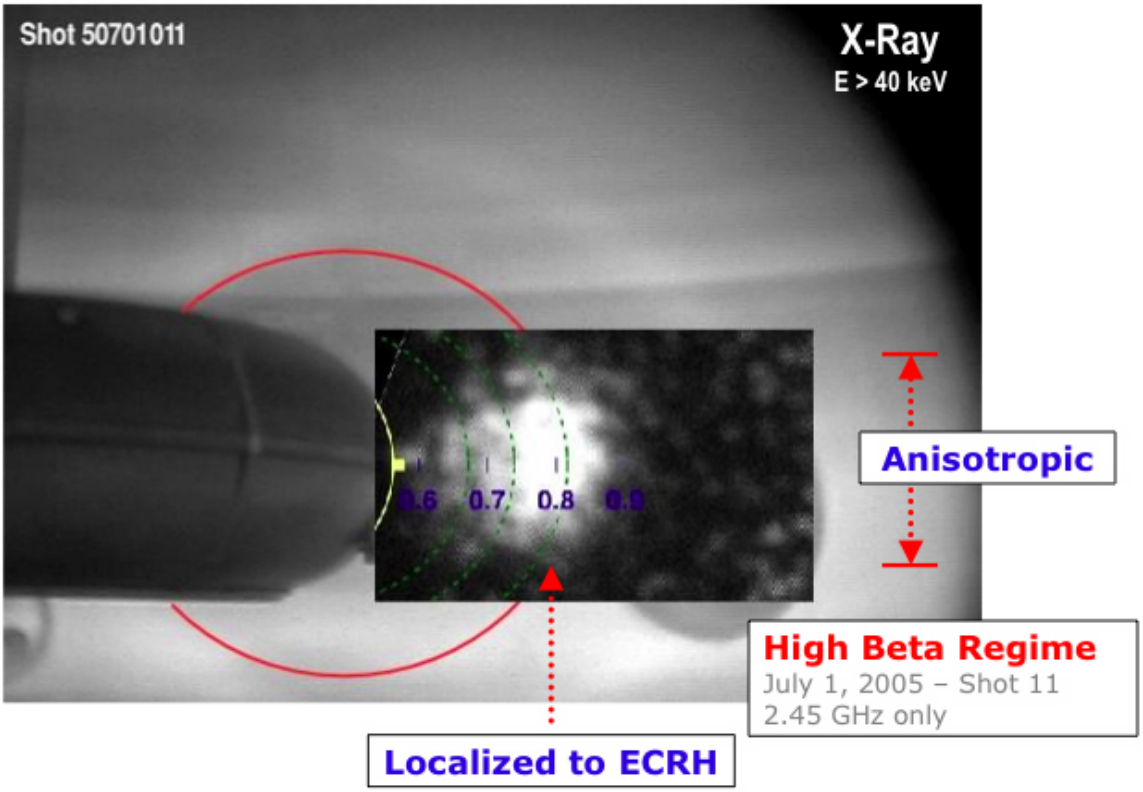

Figure 3-6: The X-ray camera image has been overlaid over a video image to be used to estimate the radius at which the pressure peaks. Notice the localization and anisotropy of the fast electrons.

pulse, quasi-steady state microwave discharges confining plasma about a supported dipole magnet for more than 10 seconds. Three regimes of operation have been observed: (1) a low-density plasma regime, (2) a high beta plasma regime, and (3) an afterglow plasma regime. Measurements of plasma equilibrium parameters during all three regimes have been reported and include edge density, edge temperature, edge plasma flows and line-average interferometer density.

Achieving a high beta plasma state requires stabilizing a pressure driven instability by properly adjusting the deuterium fuel and heating profile. The use of programmed gas puffs has proven to be an experimental control knob for determining when to enter and how long to remain in the high beta plasma regime. With insufficient neutral gas pressure the plasma will become unstable to the hot electron interchange instability. The next chapter introduces the HEI instability, presents new high beta observations of this instability, and discusses an observed hysteresis in the threshold of neutral fueling required for stability.

Chapter 4

The High Beta HEI Instability

The Hot Electron Interchange (HEI) instability has been observed in low beta plasma experiments with dipole magnetic field topologies and ECRH power. However, unlike the previous experiments, in LDX the HEI instability has been observed during both low and high beta plasmas. As such the remainder of this thesis will center around observations of the HEI instability in the high beta plasma regime.

This chapter describes the LDX high beta HEI instability. After giving a physical description of the modes, the three conditions under which the HEI instability has been observed are identified and the instability behavior for each compared. Instability behavior also varies depending on the plasma regime and selected fueling and heating parameters. Unique spectral characteristics of the high beta HEI have been identified for different combinations of heating and fueling and are presented.

4.1 HEI Instability

In a dipole magnetic geometry plasma flute instabilities result from the interchange motion. When this plasma is created using ECRH heating an intense hot electron population forms near the resonance peak. The hot electron plasma interchange motion can become unstable and give rise to the HEI instability. This instability is modified by wave/particle interactions caused when the rotating interchange mode resonates with magnetic drifts of trapped particles. The hot electrons drift resonate with the azimuthally propagating plasma instability. The low-frequency HEI instability, first described by Krall [31], was predicted to occur when,

$$-\frac{d \ln \bar{n}_{eh}}{d \ln \mathrm{V}} > 1 + \frac{m_{\perp}^2}{24} \frac{\omega_{dh}}{\omega_{ci}} \frac{\bar{n}_i}{\bar{n}_{eh}}, \tag{4.1}$$

where ω_{dh} is the magnetic drift frequency, ω_{ci} is the ion cyclotron frequency, $\mathrm{V} = \oint \mathrm{d}l/B$ is the differential volume of a magnetic flux tube, $m_{\perp}$ is the total perpendicular wave number [42], and $\bar{n}_{eh}$ and $\bar{n}_i$ are the line-averaged hot electron and ion densities, respectively. Examination of Equation 4.1 indicates that the hot electron density gradient is limited most severely at low hot electron energy (since $\omega_{dh} \propto E_{eh}$) and at high hot electron fraction ($\bar{n}_{eh}/\bar{n}_i$). In a low beta CTX plasma the HEI appears with low azimuthal mode numbers, a global mode structure, and a complex, time-evolving frequency spectrum [35]. Intense bursts of this instability caused chaotic radial transport [57], and nonlinear frequency sweeping was evidence for the inward propagation of "phase-space holes" [39].

LDX has been able to reproduce similar low beta HEI instability results as those observed on CTX. For example, during the LDX unstable low beta plasma regime nearly continuous pressure driven HEI instabilities cause rapid inward and outward radial transport of energetic electrons and severely limit the trapped electron beta. On the other hand, when LDX transitions into the high beta plasma regime, interesting new instability behaviors are observed. The remainder of this chapter presents these new observations.

4.1.1 Capturing the HEI Instability

Two high impedance probes, one mounted radially near the outer equatorial mid-plane and one inserted vertically closer to the pressure peak, have been used to capture electrostatic fluctuations created by the HEI instability. Two Mirnov coils, mounted near the equatorial mid-plane and separated by 45° on the inner vessel wall, have taken the first measurements of magnetic fluctuations during the high beta HEI instability. In previous experiments low beta plasma current did not provide enough signal for Mirnov coils to detect HEI edge magnetic fluctuations. LDX, on the other hand, excites instabilities at very high beta and the magnetic field changes are easily detected. Both magnetic and electrostatic probes have detected fluctuations that resonate with ω_{dh} of the fast electrons.

Figure 4-1 shows what a typical HEI instability looks like when captured by the high impedance probes and Mirnov coils. The top signals, (A), last approximately 10 milli-sec and show the dramatic change that occurs during the instability. This particular instability

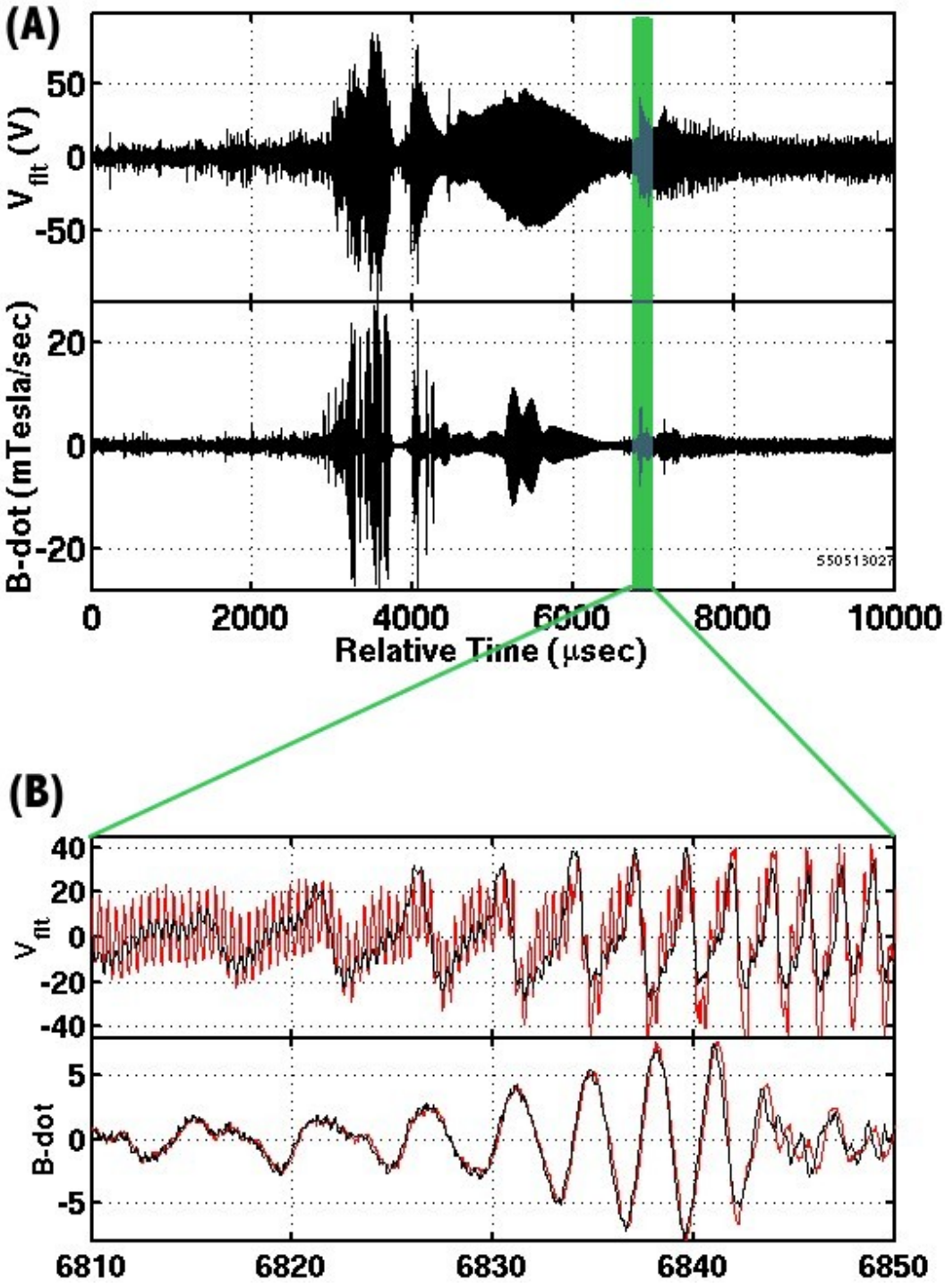

Figure 4-1: Floating potential and Mirnov signals of the drift-resonant instability on different time scales. (A) A long time scale shows a high beta instability burst during heating. Zooming in, (B), reveals the non-sinusoidal waveforms and phase.

was captured during plasma heating and at a very high ($\sim 20\%$) peak local beta. Typically, for the high impedance probes a voltage fluctuation of at least $\pm$ 25 V persists throughout the instability. However, during an early phase very intense fluctuations are measured with amplitudes saturating at a level between $\pm$ 75–125 V. During this same phase the Mirnov coils detect $\pm$ 5 to 25 milli-Tesla/sec fluctuating magnetic fields at the wall. In general the Mirnov signal ranges between $\pm$ 5 milli-Tesla/sec during the HEI.

Focusing on the smaller region highlighted in green, Figure 4-1 (B), one can examine phenomena that occur on a faster time scale. In this example the signals from both floating potential and both Mirnov coils are plotted for comparison. Fluctuations are observed to be non-sinusoidal, changing in time, and sometimes have a non-zero phase difference (although not shown in this particular segment). Multiple modes exist concurrently with independently evolving frequencies. At least two modes are discernible from this floating potential plot. One is a high frequency mode (2.5 MHz) that changes very slowly in time and the other a new rising mode (150–600 kHz) with a rapidly evolving frequency.

that probe location matters.

4.2 Conditions for HEI Instability Excitation

The local stability condition for the HEI mode is given by Equation 4.1. Instability occurs only when the energetic electron density gradient exceeds a threshold beyond the usual MHD stability limit for an anisotropic Maxwellian pressure profile. There are two populations of electrons in LDX, anisotropic energetic electrons ($p_\perp \gg p_\parallel$) equatorially trapped near the ECRH resonance and cold electrons more uniformly distributed along the field lines. The energetic electrons form a "disk" encircling the floating coil and are immersed within the larger quasineutral cold plasma [58].

This simple model for stability can be plotted to understand the conditions under which the HEI instability is excited. Figure 4-2 (A) shows Krall's condition for a 40 keV hot electron population. The y-axis is the hot electron density gradient and the x-axis is the fraction of hot electrons to total density. The blue line represents the threshold for stability with values above being unstable and below stable. Initially, when the ECRH is turned on the cold plasma begins in a low density regime. Energetic electrons ($T_e \sim 40$ keV) build up very quickly and a steep hot electron gradient drives the HEI mode unstable. Since the cold

plasma is still in low density, we expect a high fraction of hot electrons to exist. In Figure 4-2 (A) this low beta HEI instability corresponds to a hot electron density gradient above the threshold around $\bar{n}_{eh}/\bar{n}_i = 0.5$ where there is little room for stability. A stable transition into high beta can be achieved via increased fueling to provide a steady source of cold background plasma and therefore reduce the hot electrons fraction. At a lower hot electron fraction the stability limit is higher and the plasma is less likely to be unstable. Without further fueling the plasma is unstable to the HEI mode and remains in a low density regime.

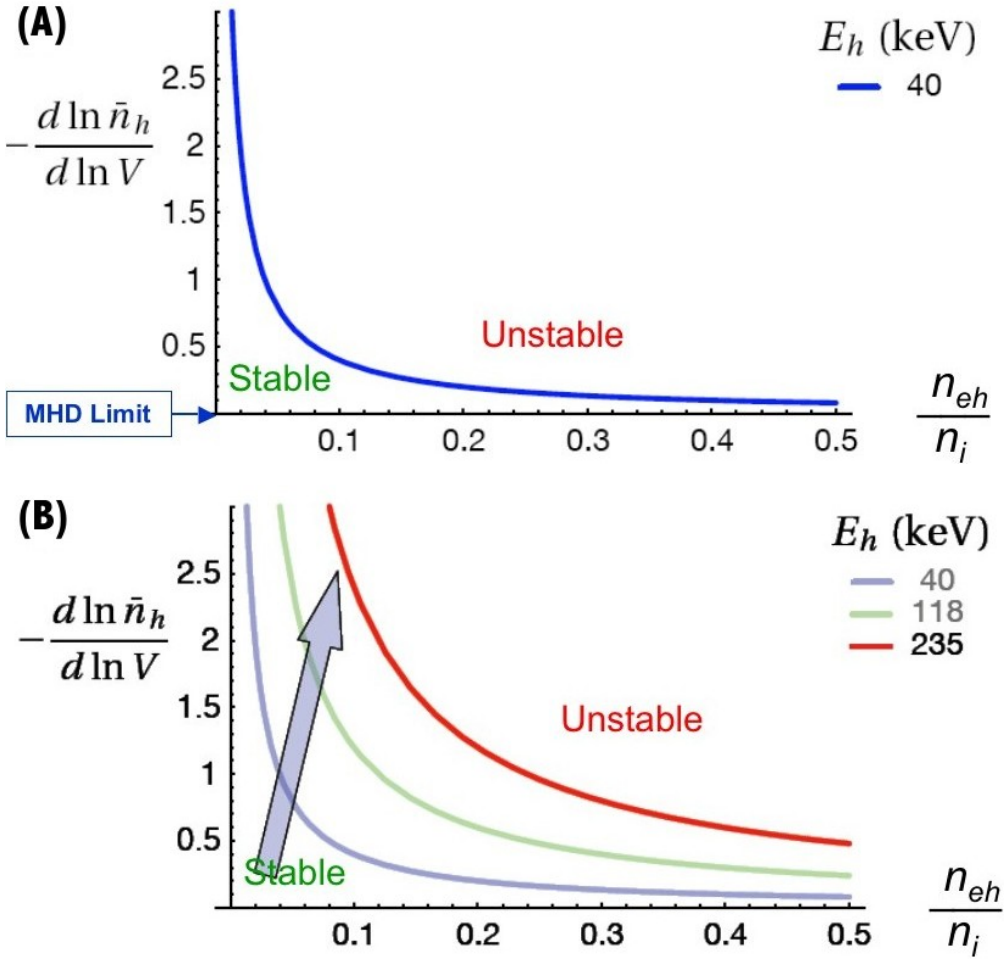

Figure 4-2: The local stability condition for the HEI mode first obtained by Krall [31] is plotted above for: (A) the low density regime and (B) the stable transition into a high beta regime.

If the fueling is properly applied a stable transition occurs between the low density and high beta regime. In this new regime the background cold plasma density remains high. Continued ECRH power heats up the energetic electron population without exceeding the stability limit. In this mode beta increases and the fast electron pressure rises by more than a factor of ten. Energetic electrons also heat the bulk plasma and a higher stability limit ($\sim$235 keV) can be achieved, Figure 4-2 (B). With continuous gas injection, quasi-stationary high beta plasma discharges can be maintained for the length of the microwave heating pulse. Nevertheless, the HEI mode can still be unstable if the hot electron density gradient approaches the new broader stability limit. When it does, we call this the HEI instability in high beta. The next three sections cover the three conditions under which the HEI instability appears in LDX.

4.2.1 Low Density Regime HEI

Figure 4-3 shows the floating potential, diode, ion saturation and X-ray intensity signals for a low density regime HEI event. By not providing sufficient gas fueling these low beta discharges can be driven indefinitely in an unstable state. The small diode signal indicates that the background density is very small. The large fluctuations on the floating potential signal represent a nearly continuous sequence of HEI instability bursts with a mode amplitude of at least $\pm$ 10 V. These bursts are observed to limit plasma buildup by causing enhanced radial transport both inward and outward. Negative current on a negatively-biased Langmuir probe shows the outward transport while a large target X-ray emission from electron impact with the dipole coil is evidence of inward transport.

4.2.2 Local High Beta Relaxation Events

Figure 4-4 shows the floating potential, diode, ion saturation and X-ray intensity signals for a small relaxation event occurring during the high beta plasma regime. Small relaxation events cause minor outward motion of the plasma diamagnetic current without a significant loss of stored energy. The diode signal at first rises and then remains higher suggesting an increase of the background plasma resulting from this motion. A broadening of the 'warm' electron population eases the hot electron density gradient enough to allow the plasma to temporarily drop back below the stable limit. The mode amplitude peaks at around $\pm$ 45 V and unlike

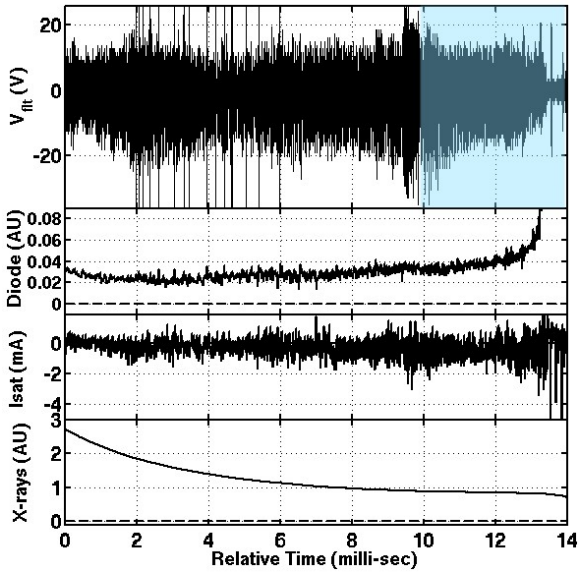

Figure 4-3: Floating potential, diode, ion saturation and X-ray signals during a low density regime HEI.

the previous case, no transport is seen by the edge probe or the X-ray diagnostics. In fact, the mode has only been detected by the top probe and is believed to be highly localized.

4.2.3 Global Intense HEI Bursts

Figure 4-5 shows the floating potential, diode, ion saturation and X-ray intensity signals for a large relaxation event occurring during the high beta plasma regime. Large global relaxation events occur in high beta discharges when the neutral pressure drops below some critical pressure ($\sim$ 1 μTorr). Intense drift-resonant fluctuations cause a rapid and nearly complete loss of fast electron energy. The stored energy loss can occur in a very short time period $\sim$ 0.1 milli-sec. Outward fast electron transport is indicated by the large electron current to a negatively-biased Langmuir probe at the plasma edge, and inward transport is deduced from X-ray bursts created as fast electrons strike the dipole coil. The diode signal spikes a short time after outward radial transport is detected and returns to a lower level once transport ends. The plasma returns to the unstable low beta regime if heating is on or just completely fades away if this event occurs during the afterglow. The HEI mode fluctuation amplitude exceeds $\pm$ 80 V and is easily observed on both top and side probes

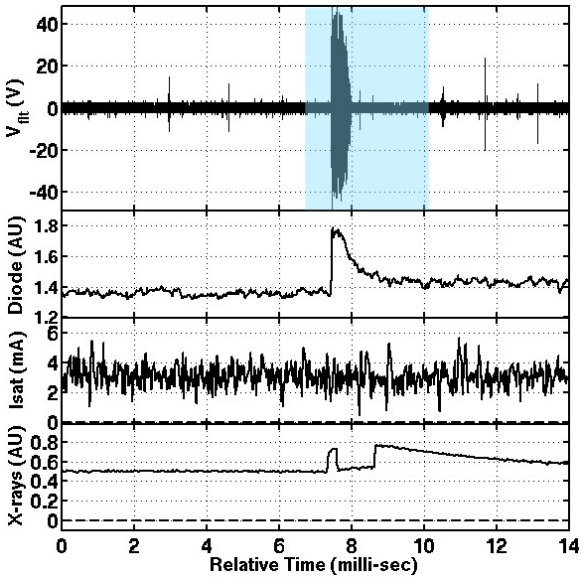

Figure 4-4: Floating potential, diode, ion saturation and X-ray signals for a small relaxation event occurring during the high beta regime.

suggesting a global mode structure during the high beta regime.

In review the HEI mode becomes unstable under three conditions on LDX. First, in the low density regime when the background density is too low to support a growing hot electron population. Here, the instability appears as brief repetitive rising frequency bursts. Second, HEI instabilities appear in the high beta regime when locally driven by a rising hot electron pressure gradient. In this case the instability appears as a short-lived, broadband frequency burst. Finally it appears again in the high beta regime as an intense global event associated with a large energy loss. It triggers a complex, time-varying frequency spectrum characterized by rising tones. The spectral characteristics of the HEI modes are significantly different for these three conditions. The remainder of this chapter focuses on spectral characteristics and the new variations observed in high beta plasma.

4.3 Spectral Characteristics

A Fourier transform over a finite window can determine a constant frequency of a digitized waveform. The HEI, on the other hand, often times has a rapidly changing mode frequency

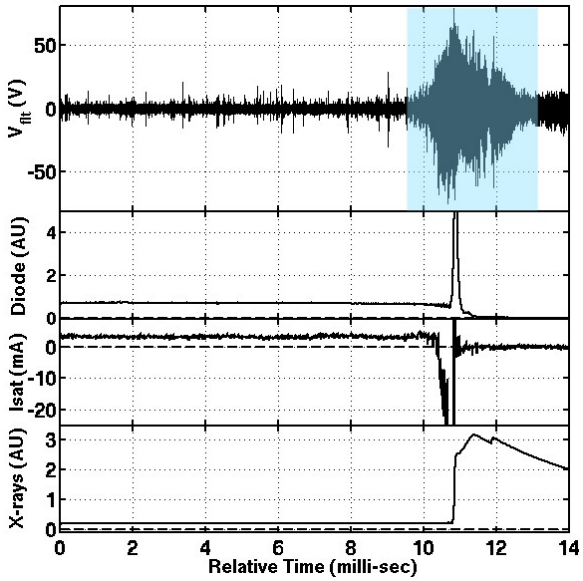

Figure 4-5: Floating potential, diode, ion saturation and X-ray signals for a large relaxation event occurring during the high beta regime.

and a single Fourier transform would not capture time-frequency evolution information. This information can be captured using a time-frequency domain (TFD) signal representation. This two-dimensional spectrum is computed using short-time Fourier transforms with a continuously moving Hamming window. The time windows can be longer for slower evolving mode frequencies allowing for better identification of mode frequencies. This tool has previously been used to study the HEI in dipoles [13, 34–36, 39, 47, 58, 60].

Three time-frequency spectrograms of the HEI instability variations in LDX are shown in Figure 4-6. The spectrograms correspond to the blue shaded areas of the floating potential signals in Figures 4-3, 4-4, and 4-5, respectively. A relative time scale has been used to allow for easy comparison between plots.

The spectral characteristics of the HEI mode are significantly different for the three conditions described above. In the low density regime HEI instability spectrogram, (A), repetitive burst of rapidly rising frequency chirps dominate the spectrum. New modes rise every hundred micro-secs or so and this rapid mode evolution makes it difficult to properly identify the mode frequency. Nevertheless, the observed lower order mode frequencies are significantly less than 1 MHz and correspond to drift-resonant electrons between 10–60 keV.

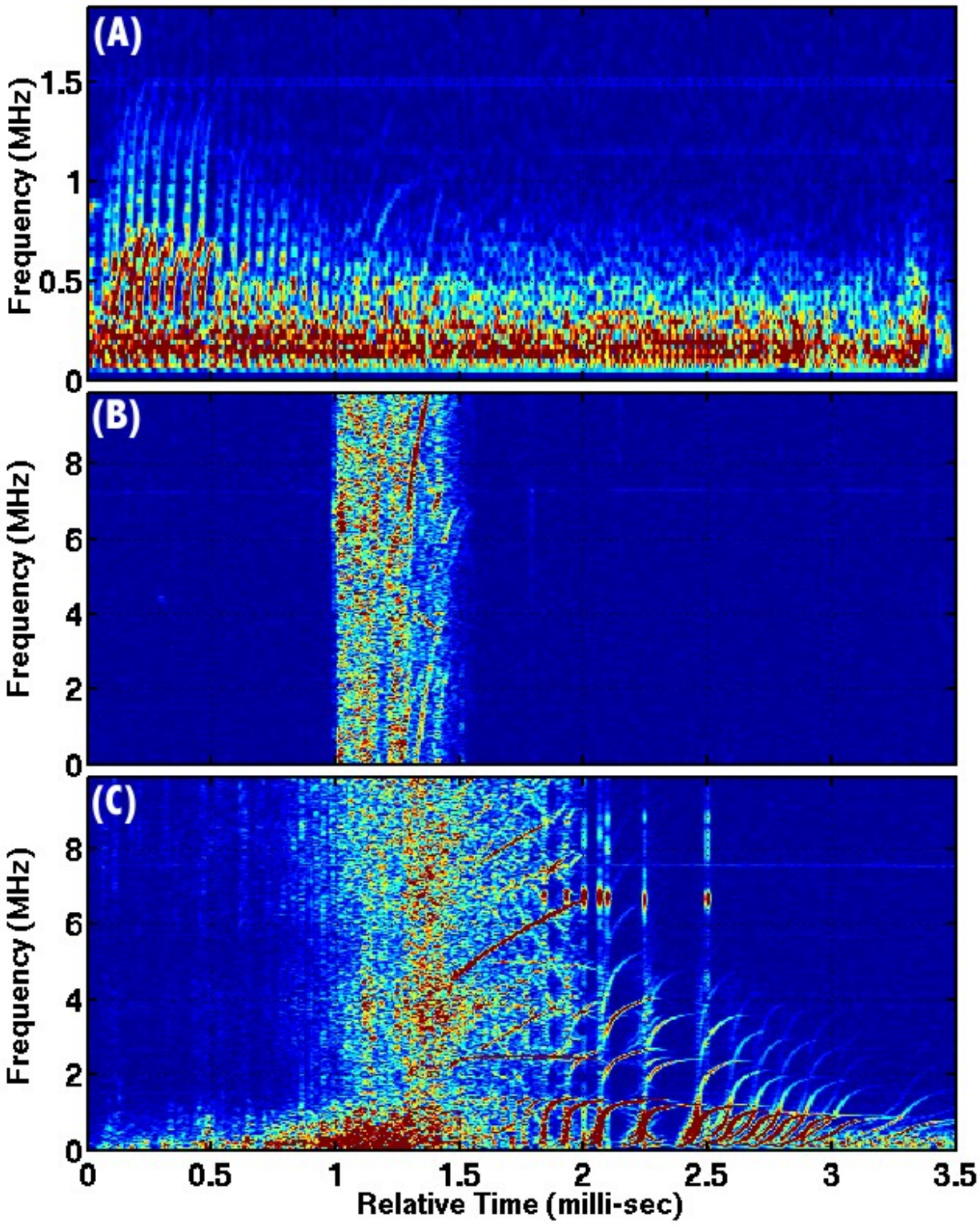

Figure 4-6: From top to bottom the HEI instabilities excited in LDX are: (A) as continuous bursts in low density unstable plasma, (B) minor relaxation event during the stable high beta plasma, and (C) intense burst associated with a collapse of high beta plasma.

The local high beta relaxation HEI instability spectrogram, (B), exhibits intense continuous bursts with a broadband characteristic followed by coherent chirps in the 1–10 MHz frequency range. The drift-resonant electrons have energies between 100–400 keV. These local events occur throughout the high beta interval and typically last less than 0.5 milli-sec.

The large high beta relaxation HEI instability spectrogram, (C), begins with 0.1–1.5 MHz narrowband fluctuations, quickly transitions into intense broadband fluctuations and transitions into coherent high frequency (2–40 MHz) fluctuations. The initial narrowband fluctuations are associated with outward radial transport while the broadband fluctuations are associated with both inward and outward transport. The intense fluctuations lead to a rapid loss of plasma density. The coherent chirping modes initially rise quickly in frequency and later fall over until a new mode takes its place.

4.4 Unique Characteristics of the High Beta HEI

The high beta HEI instability has been observed while using various combinations of fueling and heating power. Most of these observations are of the intense complete energy loss variety. We have already seen how this HEI instability leads to a complete destruction of energetic electron confinement and loss of trapped energy. While this is a constant for this type of HEI, spectrograms for the various input parameters show that the spectral characteristics vary depending on selected heating and fueling profiles. This section takes a closer look at some of these variations and at multiple probe analysis of the HEI.

4.4.1 Afterglow HEI

Excitation of an afterglow HEI instability depends upon the level of neutral pressure. If the neutral pressure decreases, a very intense HEI instability appears. Figure 4-7 shows the spectrogram for two cases: the top case is for plasma created using 2.5 kW of 6.4 GHz ECRH only power and the bottom case is for plasma created using 5 kW of combined 2.45 and 6.4 GHz ECRH power. The diamagnetic flux at the time of the HEI is twice as large for the bottom HEI. The two frequency axis are different in each spectrogram.

In the top afterglow spectrogram the broadband fluctuations rise instantaneously and last for only a milli-sec before coherent frequency chirping begins. Initially very large (1–10 MHz)

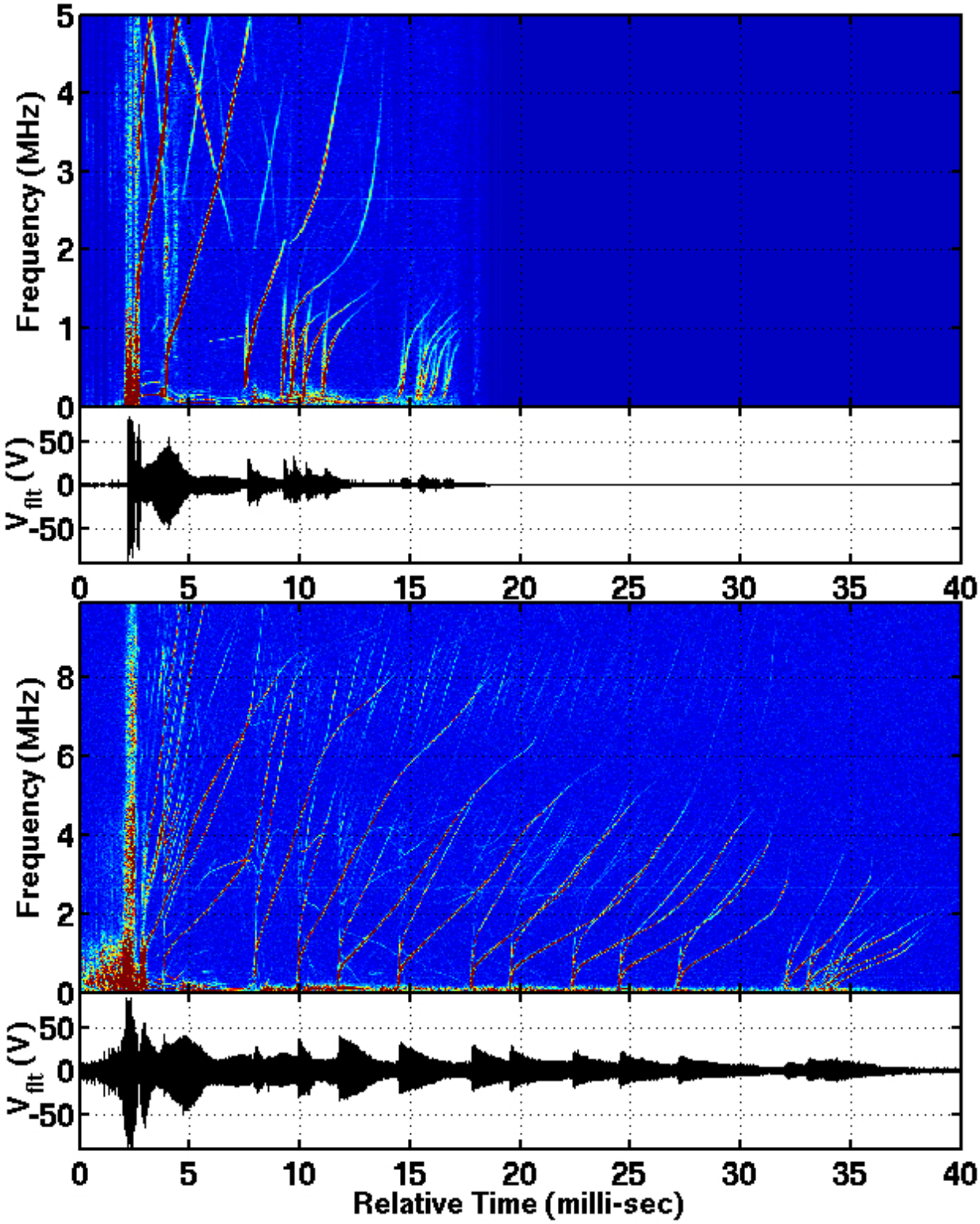

Figure 4-7: Two examples of an afterglow HEI instability. The top case occurs while using 2.5 kW of 6.4 GHz only ECRH power while the bottom case used 5 kW of combined 2.45 and 6.4 GHz power.

frequency fluctuations take control and aliasing occurs because the sample frequency for the digitizer was set too low. Eventually the mode amplitude drops from ± 50 V to around ± 10 V and the frequency chirping rolls over at 1.5 MHz. The large amplitude broadband fluctuations saturate at ± 100 V in both cases. In the bottom afterglow spectrogram the initial wide-band fluctuations last longer and begin with a 2 milli-sec period of low 0.1–1.5 MHz narrowband fluctuations followed by the broadband fluctuations. Coherent frequency chirping follows with frequencies reaching 1–20 MHz and remaining at this high level for tens of milli-sec. Individual modes fork from a single chirping source and overlap each other. Multiple modes with different azimuthal m numbers do not appear to be harmonically related but co-exist near the 1–8 MHz range. The lowest frequency, $m = 1$, mode usually has the strongest intensity and its harmonic's intensity rapidly decreases with increasing frequency. Both afterglow events end with a small cluster of low m number and low frequency chirping. The total duration for the two afterglow HEI events is 15 and 40 milli-sec for top and bottom, respectively.

4.4.2 Fueling Variations

The ability to control the fueling profile is an experimental knob used to control the plasma operating regime and improve stability. The fueling profile on LDX has evolved into a mixture of two types of puffing techniques. At first only a single pre-puff was given to the plasma before turning on the ECRH power. It was observed from these experiments that the plasma quickly "pumps" the background neutral pressure during the initial phase of the high beta plasma regime and this limits the attainable beta. A background periodic fueling puff was added to supplement the initial puff and keep a desirable level of neutrals in the experiment. This refined puffing technique has been shown to improve stability, reduce the risk of the very large HEI instability and maximize beta.

Through fueling experimentation it has been observed that a small increase in the level of fueling causes the spectral characteristics of an HEI instability to change. Figure 4-8 shows two examples where the experiment has been fueled to a point just beyond the high beta threshold. In both cases a single pre-puff fueling profile was used in which gas was injected a few milli-sec before ECRH heating takes place. For these shots the pressure after puffing and before ECRH power was 3.53 and 6.91 μTorr for the top and bottom plots, respectively.

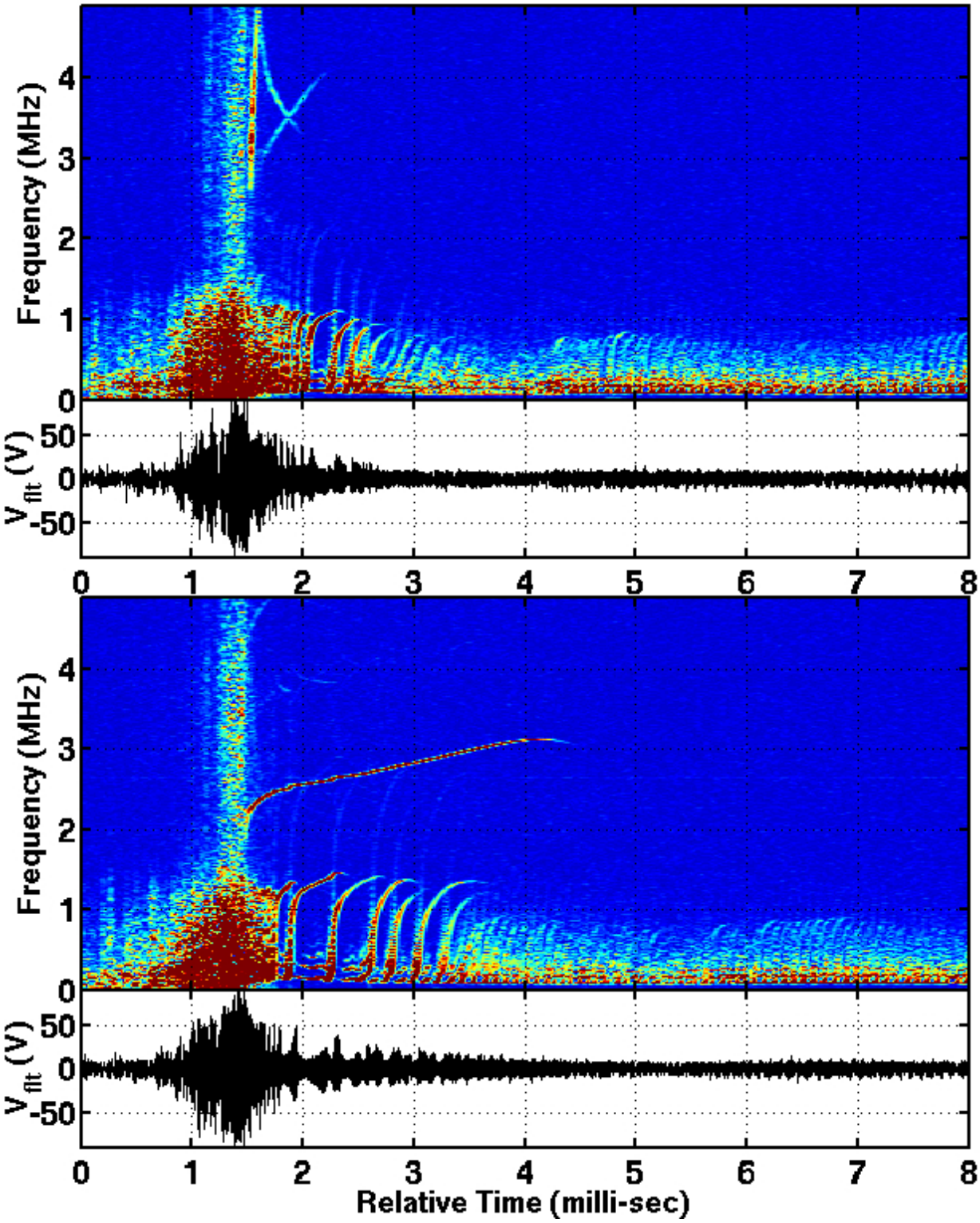

Figure 4-8: Two examples of an the same HEI instability occurring with different fueling levels. The top case had a 10 milli-sec puff before the shot while the bottom one had a 20 milli-sec puff.

At these level of fueling the experiment immediately enters a high beta plasma regime. The plasma "pumps" out the neutrals and the pressure drops to 1.01 and 1.12 μTorr right before the HEI instability forms. At this point the diamagnetic flux levels and heating profiles are the same. The spectrograms show that the instability develops similarly in both cases. After the broadband fluctuations end, coherent frequency chirping begins. In the case where less fueling is applied the coherent chirps quickly rise, turn over and fade away around 1.0 MHz while in the higher fueled plasma the chirps go up to 1.5 MHz before fading away. This indicates that the increase in fueling has indirectly lead to the creation of a more energetic electron population even when the diamagnetic flux level remains the same. After the high frequency chirping ends, both experiments return to low frequency repetitive fluctuations as the plasma transitions from a high beta to a low density regime.

4.4.3 Multiple Probe Analysis

The global mode structure of the low beta HEI instability was first determined by Levitt [35, 36] on CTX. Five movable high impedance floating potential probes located at various positions in the plasma were used to do this. These probes reconstructed the mode structure using cross-correlation analyses of probe pair combinations and a fixed 'reference' probe. In LDX only one fixed 'reference' probe and a second movable probe were used. Therefore, the same cross-correlation analyses could not be extended to study the mode structure of the high beta HEI mode. Nevertheless, a study of observations made by these two probes new and interesting characteristics of the high beta HEI mode.

Recalling from chapter 2, LDX has two floating potential probes measuring fluctuations. One is fixed on the outer mid-plane and the other, a moveable probe, enters the plasma from a top diagnostic port and can sample different flux lines depending on the selected incursion depth. The probes are azimuthally separated by 45° but the top probe was set to lie on a flux line with the same flux value as the fixed one. In theory, assuming infinite conductivity along a field line, if the two probes were azimuthally aligned they would measure the same potential. In practice they are not aligned and measure different potentials.

Local and global approximations can be made about the plasma behavior by comparing the two separated probes. One example, already discussed in the local high beta relaxation event section, shows that the small relaxation events are solely recorded on the top probe.

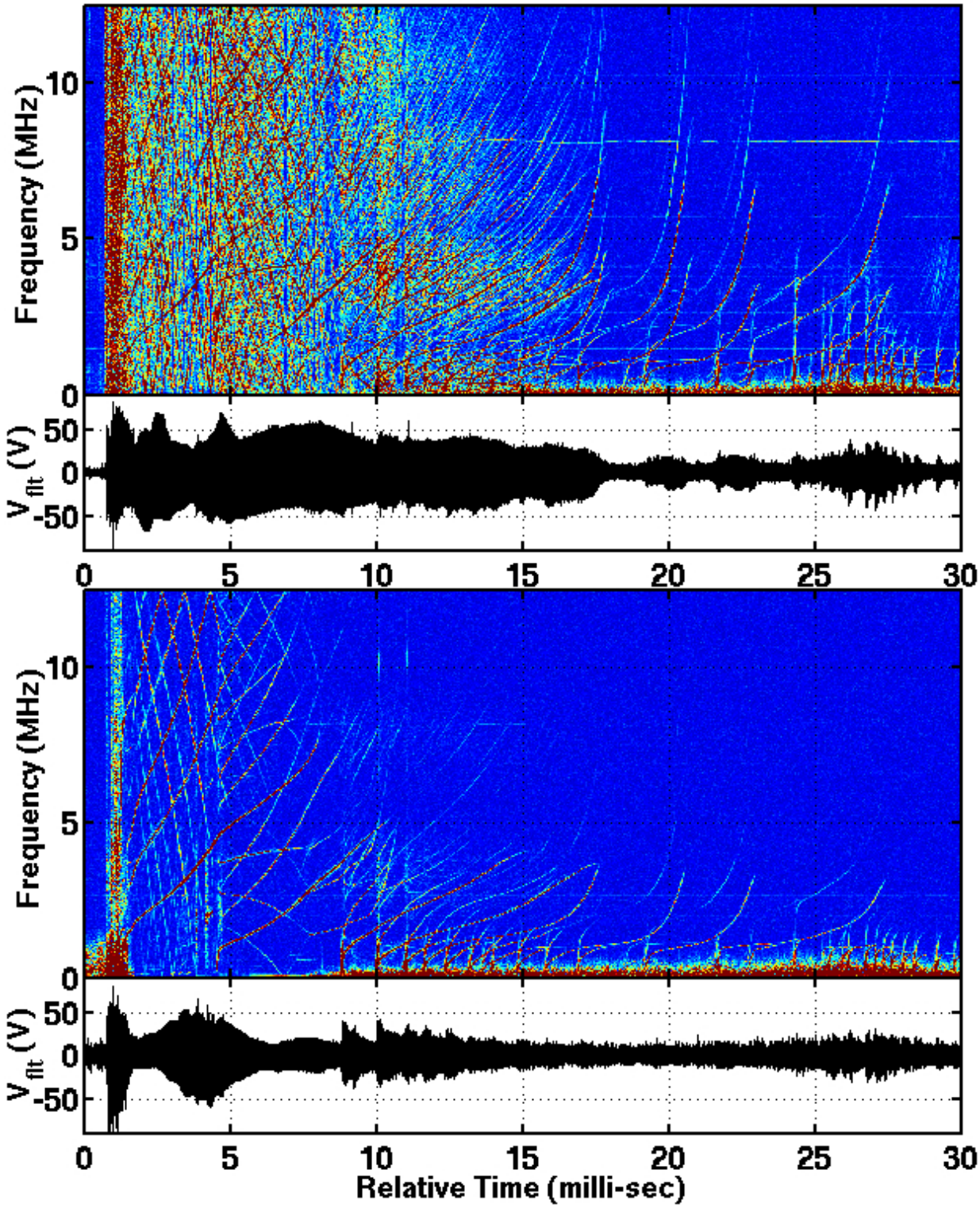

Figure 4-9: The two spectrograms show the same instability for a 2.5 kW, 6 GHz ECRH power shot. The top case is taken from the top moveable probe and the bottom case is from the fixed side probe.

This observation, combined with the fact that plasma flux drops only marginally during these events, is suggestive of localized events in which a minor rearrangement of the hot electron density gradient occurs. Moreover, these local events have only been measured on the top probe indicating a toroidal angle localization.

Another example is the observation that the top probe couples better to higher frequencies of the HEI instability. Figures 4-9 and 4-10 show spectrograms of the two probes during an HEI instability. The top spectrogram corresponds to the top probe and reveals a greater density and longer tracking of higher frequency modes. In fact, the raw signal plots also show a higher fluctuating potential measured by the top probe. Since the probe tips and frequency response are identical for both probes, the top probe detects more energetic electrons as they drift resonate past the probe tip.

The early spectral characteristics of instability are another difference between the top and side probe spectrograms. The top probe appears to jump right into a broadband high frequency particle transport phase while the side probe records a short-lived 0.1–1.0 MHz narrowband phase followed by a broadband phase. During this narrowband phase the side probe first observes a significant flux of electrons after which both probes see an increase of electron flux during the broadband phase.

4.4.4 ECRH Power Variations

Another experimental knob used to control the plasma operating regime and improve stability is the ECRH power profile. Several power experiments have shown that the LDX high beta plasma is more likely to become unstable when 2.45 GHz ECRH is applied by itself or concurrently with 6.4 GHz ECRH power. In light of this fact a special 2.45 GHz profile has been implemented to ensure that the plasma does not become unstable. This profile uses a delayed 2.45 GHz ECRH power injection after the 6.4 GHz ECRH has been used to enter a high beta plasma. A rapid rise in beta occurs when the 2.45 GHz source comes on and the highest beta shots have been created using this combined profile.

Before the new profile was used the high beta HEI instability was mostly commonly recorded during a combined power profile where both sources were initiated concurrently. Only in a couple of instances, Figures 4-7 and 4-9, did the 6.4 GHz ECRH only profile yield HEI instabilities. This does, however, reveal unique spectral characteristics when compared

to the combined power HEI instabilities. Unfortunately, no high beta HEI instabilities were captured using a 2.45 GHz only ECRH power profile.

The spectrogram in Figure 4-9 can be compared to the spectrogram in Figure 4-10 since both occur during the ECRH. The data from Figure 4-9 was captured during a 2.5 kW, 6.4 GHz ECRH only power profile. The data from Figure 4-10 was captured during a 5 kW, combined 2.45 and 6.4 GHz ECRH power profile. Spectrograms from both cases begin with the wide-band fluctuations lasting less than 1 milli-sec. In both cases several coherent modes rise very rapidly in frequency well beyond 20 MHz. This persists longer for the 6.4 GHz only spectrogram where the lowest m number mode lasts at least 8 milli-sec. In contrast, the entire high beta HEI for the combined heating case lasts only 6 milli-sec. Remember that the combined heating plasma has a higher energy hot electron population and twice the beta. A higher beta therefore does not translate into a longer HEI instability event or more complex chirping behavior. The duration of the chirping on the other hand is tied to the distribution of the energetic electron density, the transport of this population, and intensity of the bursts.

Another difference between the two spectrograms is in the individual mode development. The combined heating spectrogram shows modes which begin flat at 0.1 MHz frequency before sharply rising and then falling over and fading away. In contrast, the 6.4 GHz spectrogram shows a single mode which quickly rises and forks into two new modes. The two new modes continue to evolve in frequency. Both the afterglow and heating 6.4 GHz spectrograms show that the new modes undergo another sharp rise before fading away.

In general, the duration (and even appearance) of the 6 GHz HEI resembles that of the afterglow spectrograms presented earlier, Figure 4-7. Afterglow and 6.4 GHz only HEI maintain a long-lasting, complex and beautiful chirping behavior unlike the other cases. Whether or not heating with the 2.45 GHz source adversely affects the chirping behavior during the high beta HEI instability is still an open question. One study by Masklovsky does find that applying an rf field of sufficient intensity and pulse-length can suppress coherent interchange fluctuations and eliminate frequency sweeping [40]. It may be that 2.45 GHz ECRH yields similar results when applied to the high beta HEI instability in LDX.

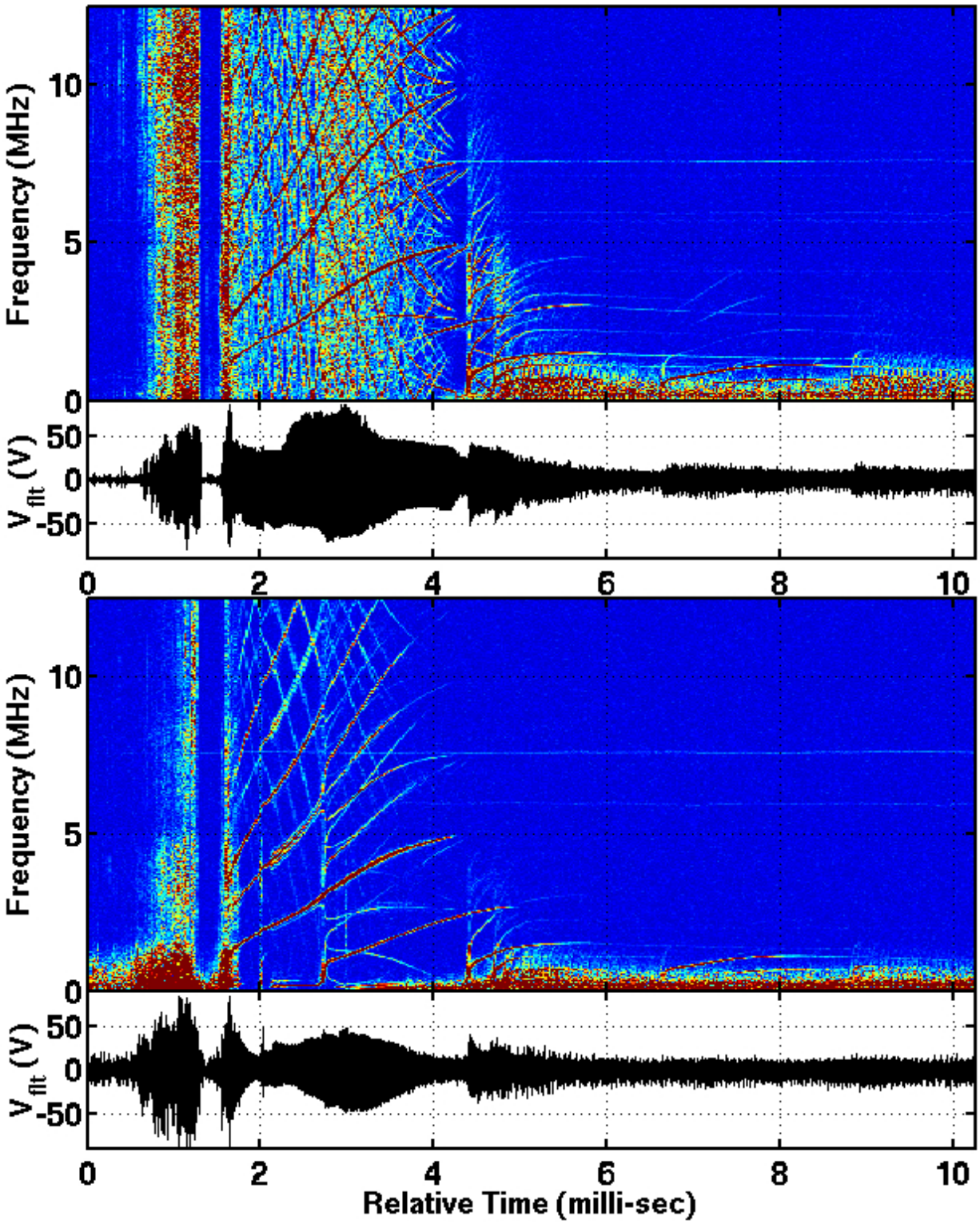

Figure 4-10: The two spectrograms show the same instability for a 5 kW, both sources shot. The top case is taken from the top moveable probe and the bottom case is from the fixed side probe.

4.5 Summary

In this chapter the Hot Electron Interchange (HEI) instability in LDX was presented. HEI instabilities are excited by energetic electrons that are trapped in the dipole magnetic field and exhibit complex, coherent spectral characteristics and frequency sweeping. In LDX this instability is excited in both low and high beta regimes. LDX is the first experiment to observe the high beta HEI instability which was found to occur under three conditions: during the low density regime, as local high beta relaxation events and as global intense energy relaxation bursts. The spectral characteristics of the HEI were determined using time-frequency domain spectrogram plots. The spectrograms of this interchange instability reveal unique characteristics of the high beta HEI instability which include: long lasting afterglow HEI instabilities, affects on the creation and spectral characteristics of the HEI instabilities due to level of fueling, the presence of both local and global HEI during high beta plasma, and differences in the quantity, timing and spectral characteristics of the HEI instabilities due to different ECRH heating power profiles.

Chapter 5

High Beta HEI Plasma Transport

The high beta HEI mode has been introduced and measurements of electrostatic fluctuations using high impedance probes have revealed the spectral characteristics of the instability. In this chapter the high beta HEI instability is examined in greater detail and new results are introduced, which relate directly to the transport of hot electrons. Since the HEI disturbs and rearranges the high beta electrons in physical space it causes changes in the diamagnetic current, which can be detected by Mirnov coils providing the first non-perturbing, high-speed diagnostic of the HEI-induced transport. The conditions under which HEI induced transport occur and the consequence of this transport to the stability of HEI are also discussed.

This chapter is organized into four sections. LDX is the first experiment to capture the HEI instability with fast magnetic diagnostics. Unfortunately, rapid changes in the magnetic fields cause eddy currents in the walls, which become a source of unwanted noise in these signals. The first section covers how to analyze the raw data and filter out the eddy current noise. The second section looks at measurements of the rapid changes in diamagnetic current. During intense instabilities the magnitude of the magnetic fluctuations significantly exceeds the magnitude of the equilibrium field generated by the high beta electrons and the confinement ends in less than 100 μsec. In the third section observations of wave-induced, chaotic, radial transport of energetic electrons in the low beta plasmas in CTX [58] are compared to radial transport results of the high beta HEI instability in LDX. For high beta plasmas the increase in the flux of energetic particles at the wall is well correlated with the presence of fluctuations that meet the condition for global chaos. The fourth section describes the observed hysteresis in neutral gas fueling required to stabilize and maintain a

high beta plasma due to the radial transport induced by the HEI instability. High neutral fueling is required to create a high beta plasma, but, once stabilized, lower neutral fueling is needed to maintain the high beta state.

5.1 Correcting for Eddy Currents

In a high beta plasma when the diamagnetic current rapidly changes in LDX, eddy currents are induced in the vacuum vessel. If these induced currents remain in a fixed position for periods lasting tens of milli-sec they resistively decay. Since the magnetic diagnostics detect both the total field (i.e. from the plasma and f-coil) and the fields due to eddy currents, understanding the time-scale and structure of the eddy currents aids in the interpretation of magnetics data. In this analysis the vacuum vessel is assumed to be a uniform sphere. The eddy currents are expanded in terms of spherical harmonics. Each spherical mode is characterized by an eddy-current decay rate. Using these eddy-current eigenmodes LDX magnetic diagnostics can be correctly discussed.

5.1.1 Representing Eddy Currents

If the eddy currents flow on a sphere of radius b then the magnetic fields from the eddy currents can be expressed in terms of the gradient of a magnetic potential,

$$\mathbf{B}(\mathrm{r},\theta,\phi) = \begin{cases} \nabla\chi_i, \text{ if r} < \text{b} \\ \nabla\chi_o, \text{ if r} > \text{b}. \end{cases} \tag{5.1}$$

Since $\chi_{i,o}$ satisfies Laplaces equation, it can be represented in spherical coordinates as

$$\chi_i = \sum_{l,m} A_{lm} \left(\frac{r}{b}\right)^l Y_{lm}(\theta,\phi) \tag{5.2}$$

$$\chi_o = \sum_{l,m} B_{lm} \left(\frac{r}{b}\right)^{-(l+1)} Y_{lm}(\theta,\phi) \tag{5.3}$$

When the eddy currents are expanded in a similar fashion, the boundary conditions at $r = b$ are easily incorporated. Surface eddy currents are defined to be $\mathbf{J} = \hat{r} \times \nabla K$, and satisfy

the boundary conditions with

$$\hat{r} \cdot \nabla[\chi_o - \chi_i] = 0 \tag{5.4}$$

$$\hat{r} \times \nabla[\chi_o - \chi_i] = \mu_o \hat{r} \times \nabla K. \tag{5.5}$$

The first condition, continuity of the radial field, gives $B_{lm} = -A_{lm} l/(l+1)$. Using Ampere's Law, Equation 5.5,$\mu_o K_{lm} = -A_{lm}(2l+1)/(l+1)$ and the control current is

$$\mathbf{J} = \left(\hat{\phi} \frac{1}{b} \frac{\partial}{\partial \theta} - \hat{\theta} \frac{1}{b \sin\theta} \frac{\partial}{\partial \phi} \right) \sum_{l,m} K_{lm} Y_{lm}(\theta, \phi). \tag{5.6}$$

K_{lm} has units of A/m, and $\mathbf{J}$ is a surface current with units of A/m^2.

Plasma Field

The time-varying plasma fields at the vessel wall are assumed to be due to currents near the magnetic axis, $r \ll b$. The far-field of these currents can be expanded like Equation 5.3, with $\mathbf{B} = \nabla \chi_p$, and

$$\chi_p = \sum_{l,m} P_{lm} \left(\frac{r}{b} \right)^{-(l+1)} Y_{lm}(\theta, \phi). \tag{5.7}$$

Equilibrium plasma currents are represented by spherical harmonics with mode number, $m = 0$. Instabilities cause non-axisymmetric currents with $m \neq 0$. For up-down symmetric current, an accurate representation of the field results by including only the dipole ($l = 1$) and quadrupole ($l = 3$) components.

Faraday's Law

Faraday's law of induction and Ohm's law are used to describe the induction of eddy currents due to time-changing plasma currents and the resistive decay of the induced eddy currents. Faraday's law is given by

$$\nabla \times \mathbf{J} = -\sigma \nabla \left(\frac{\partial \chi_{wall}}{\partial t} + \frac{\partial \chi_p}{\partial t} \right). \tag{5.8}$$

The surface conductivity is $\sigma \equiv \delta/\rho$; the ratio of the wall thickness to its resistivity. In LDX $\sigma = 2.6 \times 10^4\ \Omega^{-1}$ with $\delta = 0.75$ inch and $\rho = 7.2 \times 10^{-7}\ \Omega \cdot m$.

Substituting Equation 5.6 into Equation 5.8, the eddy currents are found to be

$$K_{lm}(t) = -\frac{b\,\sigma}{l}\frac{\partial}{\partial t}[P_{lm}(t) + B_{lm}(t)]. \tag{5.9}$$

Then by applying the boundary conditions we obtain

$$\frac{\partial A_{lm}}{\partial t} + A_{lm}\left(\frac{2l+1}{\mu_o \sigma b}\right) = \left(\frac{l+1}{l}\right)\frac{\partial P_{lm}}{\partial t} \tag{5.10}$$

$$\frac{\partial B_{lm}}{\partial t} + B_{lm}\left(\frac{2l+1}{\mu_o \sigma b}\right) = -\frac{\partial P_{lm}}{\partial t}. \tag{5.11}$$

Here the eddy current decay rate, $1/\tau_{lm} \equiv (2l+1)/(\mu_o \sigma b)$, is independent of the mode number, m. For the dominant dipole moment, $l = 1$, the decay rate is 1/28 milli-sec^{-1}. For the next moment, $l = 3$, the decay rate is faster, 1/12 milli-sec^{-1}. An interesting mathematical result confirms that if the spherical wall was a perfect conductor, $\sigma \to \infty$, then B_{lm} would equal $-P_{lm} = -A_{lm}l/(l+1)$, $\mu_o K_{lm} = -(2l+1)P_{lm}/l$ and the magnetic field, $\mathbf{B}$, would be zero outside the wall as expected.

Magnetic diagnostics respond to either the time derivative of the magnetic field (e.g. Mirnov coils) or to the magnetic field strength (e.g. Hall probes). Sometimes the data from such diagnostics is recorded after passing through a high-precision integrator so that the signal from a coil or loop becomes proportional to the field or to the flux.

For a magnetic coil or loop outside the vacuum vessel, the plasma current is determined from

$$P_{1,0}(t) \propto \int_0^1 dt' V(t') + \tau_{1,0} V(t') \tag{5.12}$$

where $\tau_{1,0} \approx 28$ milli-sec is the dominant, low-order eddy-current decay time and where $V(t) \propto d(P_{1,0} + B_{1,0})/dt$.

For a magnetic coil inside the vacuum vessel (measuring B_θ), the plasma current is determined from

$$P_{1,0}(t) \propto \int_0^1 dt' V(t') - 2\tau_{1,0} V(t') \tag{5.13}$$

where $V(t) \propto d(P_{1,0} + A_{1,0})/dt$, and the factor of two results from $(l+1)/l = 2$ for $l = 1$. For short times relative to the decay rate, the *local* poloidal field just inside the wall is about 3 times *larger* than it would be in a vacuum without eddy currents. The magnetic

signals are easy to correct using an IDL or MATLAB procedure. All of the data from magnetic diagnostics presented in this thesis has been corrected for eddy current effects unless specifically stated otherwise.

5.2 Nonperturbing High Speed Diagnostic

The HEI instability disturbs and rearranges the high beta carrying trapped hot electrons. Experimental evidence shows that hot electron particles move outward towards the wall during the instability (presented in chapter 4). An indirect measurement of this particle transport can be achieved by studying fast data collected from Mirnov coils. Since Mirnov coils measure the rapidly changing magnetic field at the inner wall of the vessel, a dramatic change in this signal can give a better understanding of how quickly the particles escape from the hot electron ring in the plasma center to the walls. This section presents the various fast magnetic probe results and how the particle transport is observed using these probes.

Global Intense HEI

As the particles move outward a temporary increase in the magnetic field is expected. The perturbed fast electron pressure creates large perturbations to the diamagnetic current detected as fluctuations in the Mirnov coil signal. These fluctuations are caused by hot electron plasma radially rearranging itself during the instability. As the particles hit the walls, the magnetic fluctuations should decrease in amplitude and eventually, with no more hot particles to support it, go away.

An integration of the Mirnov signal can be compared to poloidal field measurements from a B_p coil at the wall. One example is shown in Figure 5-1, which shows the magnetic signature of an intense HEI instability associated with a rapid transition from high to low beta. Figure 5-1 shows five signals including the mid-plane ion saturation probe (top), mid-plane electrostatic floating potential probe (bottom) and three different magnetic probes: internal Mirnov coil, external mid-plane outer flux loop, and external mid-plane outer poloidal coil.

A closer look at this Figure shows how the magnetic signals respond to the instability and gives a better understanding of when and how quickly particles are lost to the walls. The data begins during a stable high beta plasma. The ion saturation current, normally a positive number since the probe is biased negative to attract ions, is proportional to the edge

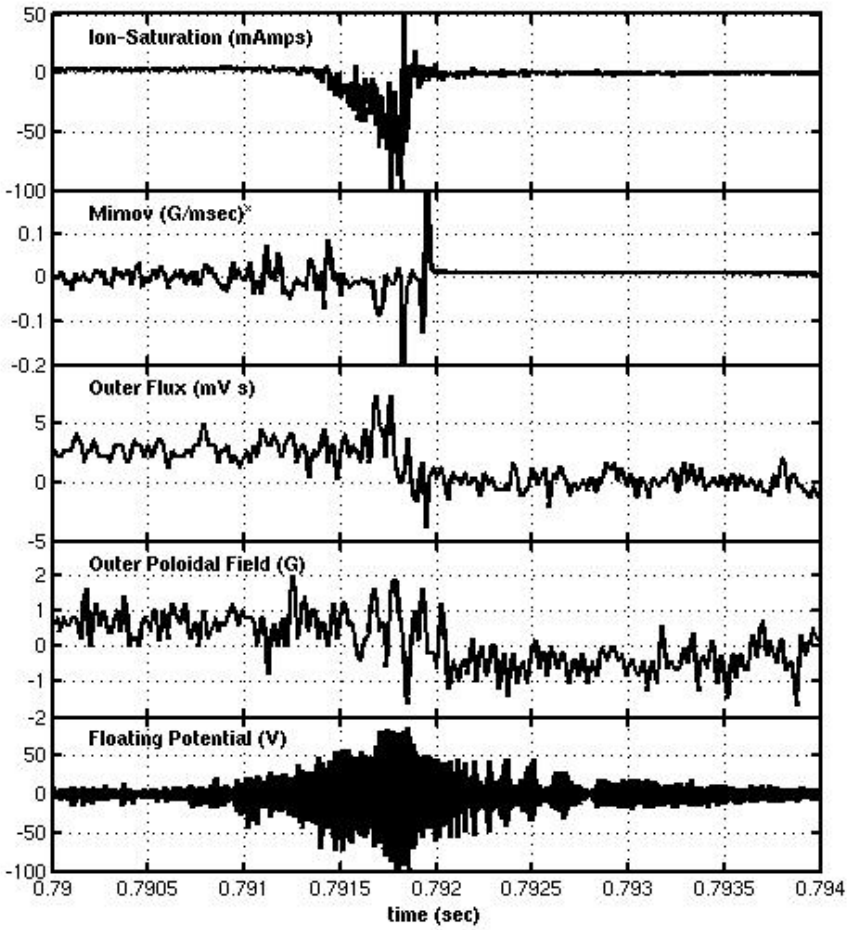

Figure 5-1: From top to bottom: edge ion saturation probe, Mirnov signal, outer mid-plane flux loop, outer local poloidal field, and floating potential. Eddy current effects have been subtracted from the magnetic signals. The intense HEI causes an abrupt loss in diamagnetic current and non-axisymmtric magnetic fluctuations.

plasma density. Before the HEI instability is excited the probe remains positive displaying five milli-Amps of current and a stable and decent edge plasma. The floating potential probe shows a typical background fluctuation level (>10 V) during this high beta plasma. Then, as the HEI instability is excited, t<.791 sec, it grows and the magnetic fluctuation levels exceed the typical background values. A strong negative current is coincidentally detected by the ion-saturation probe as hot electrons move radially outward, overcome the probe potential barrier, and overwhelm the probe's ability to collect ions. An initial increase in all magnetic signal fluctuation levels accompanies this large flux of hot electrons to the ion saturation probe. Corresponding non-axisymmetric fluctuations measured by Mirnov coils rise to at least five times the equilibrium diamagnetic field fluctuations when compared to the preceding stable interval.

Once the flux of hot electrons to the ion-saturation probe dies down, the magnetic diagnostic fluctuations return to normal values and the plasma enters a low beta state. Unfortunately, the Mirnov signal saturated at t=.792 sec and the diagnostic no longer yields reliable information. An abrupt decrease in the diamagnetic (outer) flux and outer poloidal field follows and based on estimates of beta from the outer flux loops, we observe a 90% drop in confined high beta electrons. In this intense high beta collapse event, confinement of the bulk of the hot electrons ends in less than 100 μsec and, if (not shown here) this occurs during heating, a buildup of beta will occur again but on a much slower 100 milli-sec time scale which can also lead to the stabilizing of the HEI mode. When instability occurs during the afterglow it is clear that without heating the remaining hot electron population will continue to interchange and its motion will lead to long periods of the frequency chirping.

Local Relaxation HEI

In the previous chapter we learned that not all high beta HEI events are created equal. A look at the magnetic signature of the localized HEI instability is shown in Figure 5-2. As before the analysis begins by looking at the ion saturation probe. Note that the axis has been re-scaled relative to Figure 5-1 and the Floating Potential signal is from the top moveable probe. Observe that no large scale hot electron flux is detected by the probes prior to, during or after the instability. The fluctuation levels remain constant, albeit, with occasional blips of plasma that momentarily drive the current negative, but have no correlation to the magnetic or electrostatic probes.

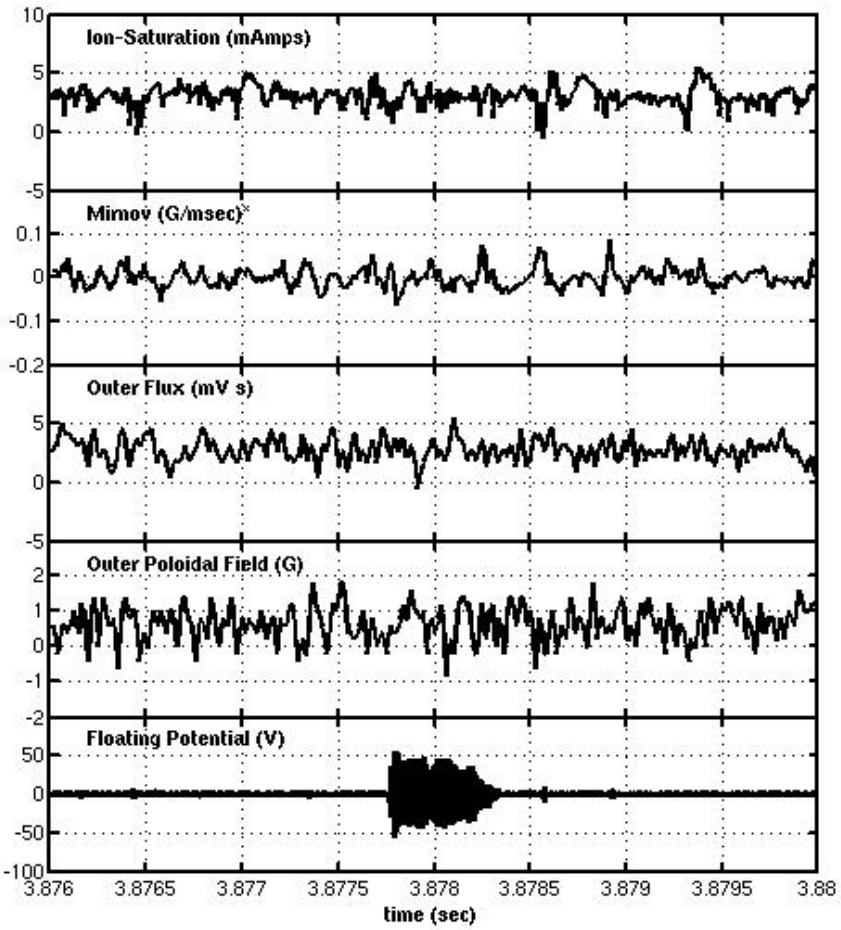

Figure 5-2: From top to bottom: edge ion saturation probe, Mirnov signal, outer mid-plane flux loop, outer local poloidal field, and floating potential. The localized HEI instability does not cause an abrupt loss in diamagnetic current and magnetic fluctuations remain about their high beta levels.

The magnetic probes do not exhibit any major changes either and appear to remain at their steady state high beta global fluctuation levels. Even the Mirnov coil, which can detect more localized instability behavior, does not change. This may be because there are no Mirnov coils located near the upper floating potential probe that detected the localized HEI event. Therefore, nothing too exciting happens during this local pressure re-arrangement HEI instability and large scale transport is not detected.

Low Beta HEI

Low beta plasma in LDX has no discernible magnetic signature as can be seen in Figure 5-3. Initially, the ECRH adds energy to a highly peaked plasma ring. For under-fueled plasma conditions the low beta HEI appears as quasiperiodic bursts that drive hot electrons outward. The ion-saturation probe detects a negative current with a highly fluctuating amplitude. The diamagnetic field is so small that the outer flux loop barely measures any steady state flux. The Mirnov coil fluctuations are virtually non-detectable. The floating potential does measure a fairly strong fluctuation level and the constant particle flux to the ion saturation probe shows that the radial extent of hot electron transport associated with the quasiperiodic bursts remains strong even during the low beta ECRH period. In fact, this is true until the experiment enters into a stable high beta regime, as described in chapter 4, or the HEI mode is stabilized and no longer dominant.

5.3 HEI Wave-Induced Particle Transport

In this section the relationship between the observed fluctuations and particle transport will be investigated. For charged particles in a strong magnetic field the equations of motion describe the energetic wave-particle interactions of the experimentally observed electrostatic fluctuations and shed light on the radial transport properties. It will be shown that the amplitude, frequency and azimuthal mode number of certain HEI instabilities meet the conditions for the onset of chaotic particle motion. Chaos induced by the wave activity of the high beta HEI mode can lead to broad radial transport of hot electrons during very intense HEI instability events but not during relaxation events.

The interaction between the HEI drift-resonant electrostatic waves and the energetic

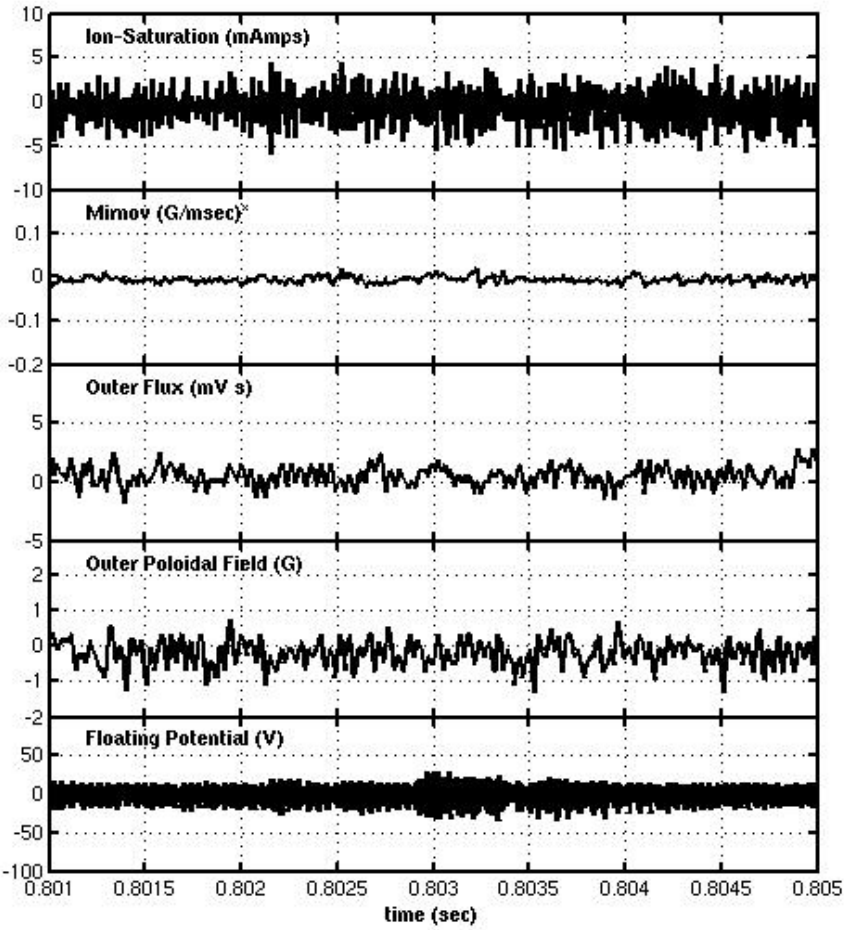

Figure 5-3: From top to bottom: edge ion saturation probe, Mirnov signal, outer mid-plane flux loop, outer local poloidal field, and floating potential. The low-beta HEI instability occurs during low levels of diamagnetic current and the corresponding magnetic fluctuations are barely noticeable when compared to the high beta plasma fluctuations.

electrons observed in the lab can be described by the guiding center drift Hamiltonian [6],

$$H(\rho_\parallel, \psi, \varphi, \chi) = \frac{1}{2}\frac{m_e c}{e}\rho_\parallel^2 B^2 + \frac{\mu}{e}cB - c\Phi = \frac{\mu}{e}cB - c\Phi, \tag{5.14}$$

where e, m_e, and μ are the charge, mass, and magnetic moment of the electron and Φ is the electrostatic potential. This form is appropriate since the observed electrons are non-relativistic. For the dipole, curl-free magnetic field, the canonical coordinates of the guiding center drift Hamiltonian (ψ, φ) are essentially the magnetic coordinates defined by $\mathbf{B} = \nabla\varphi \times \nabla\psi = \nabla\chi$. The relevant functions in spherical coordinates are $\psi = M\sin^2\theta/r$, which is proportional to the magnetic flux bounded by a field line, and $\chi = M\cos\theta/r^2$, which is related to the distance along a field line, where M is the magnetic dipole moment given in chapter 2.

For an anisotropic ($p_\perp \gg p_\parallel$) equatorially trapped electron population particle motion is confined to the midplane of the magnetic field where $\rho_\parallel \equiv v_\parallel/B \approx 0$, $B = B(\psi)$, $\psi = M/r$ and the magnitude of the magnetic field is $B = M/r^3$. Thereby the equations of motion become only two-dimensional:

$$\frac{\partial\varphi}{\partial t} = \frac{\partial H}{\partial\psi} = \frac{\mu}{e}c\frac{\partial B}{\partial\psi} - c\frac{\partial\Phi}{\partial\psi} = \omega_d - c\frac{\partial\Phi}{\partial\psi} \tag{5.15}$$

$$\frac{\partial\psi}{\partial t} = -\frac{\partial H}{\partial\varphi} = c\frac{\partial\Phi}{\partial\varphi}. \tag{5.16}$$

For equatorial hot electrons the magnetic precessional drift frequency is:

$$\omega_d = \frac{3c\mu B}{e\psi}. \tag{5.17}$$

The fluctuations present during the HEI instability are modeled as a sum of traveling waves,

$$\Phi(\varphi, t) = \frac{\Phi_\circ}{\sqrt{\wp}}\sum_{l,m}^{N} a_{lm}\ cos(m\varphi - \omega_l t + \varphi_l), \tag{5.18}$$

where $\wp = \sum_{lm}|a_{lm}|^2$. The relative amplitudes, azimuthal mode numbers, frequencies and phases are determined from Fourier analysis of the measured electrostatic probe signals.

For a single electrostatic wave the island half-width, $\triangle\psi$, at the resonant surface defined

by $\omega_l - m\omega_d(\mu, \psi^r_{lm}) = 0$, is given by the solution to the equation,

$$(\triangle\psi)^2 \left[1 + \frac{\triangle\psi}{3\psi^r_{lm}}\right] - \frac{2\Phi_\circ \psi^r_{lm}}{\omega_d} = 0. \tag{5.19}$$

Each wave in the series forms a drift island of width $\triangle\psi_l \simeq (2\Phi_\circ \psi^r_{lm}/\omega_d)^{1/2}$, where ψ^r_{lm} is the resonant drift surface. When multiple drift-resonant waves with sufficiently large amplitude are present islands will overlap and lead to chaotic radial transport [58].

5.3.1 Global Chaos During HEI events

An examination of the fluctuation spectrum used to model the electrostatic potential as in Equation 5.18 will yield the necessary conditions to study the topological properties of the particle trajectories. This analysis can easily be performed using an HEI instability electrostatic fluctuation signal and the results compared to contributions from other diagnostics to confirm the existence (or absence) of global chaos.

We take a look at three types of HEI events in LDX: the intense high beta HEI instability, the localized high beta relaxation HEI instability, and the low beta HEI instability. Specifically, we break down the signals into a wave spectrum and apply the island width analysis from above. Then we determine if the conditions for the onset of global transport occur for the various HEI events.

Analysis of Intense HEI events

Figure 4-6 (c) shows the time-frequency spectrogram of an intense high beta HEI instability. Both coherent and incoherent fluctuations are clearly present during the instability. Initially, a period of incoherent fluctuations dominate the spectrum. Concurrently, a strong negative current is measured at an edge probe. The presence of this large current suggests that hot electrons have made it from inside the plasma to the wall. Afterward a period of coherent frequency sweeping takes over and the strong negative current declines. For the intense high beta HEI instability two separate analysis are done since we suspect global transport for one period and not the other.

To represent the conditions of the coherent phase a series of ten waves, modeled from experimental data obtained from Figure 5-4 and representing a snapshot during frequency

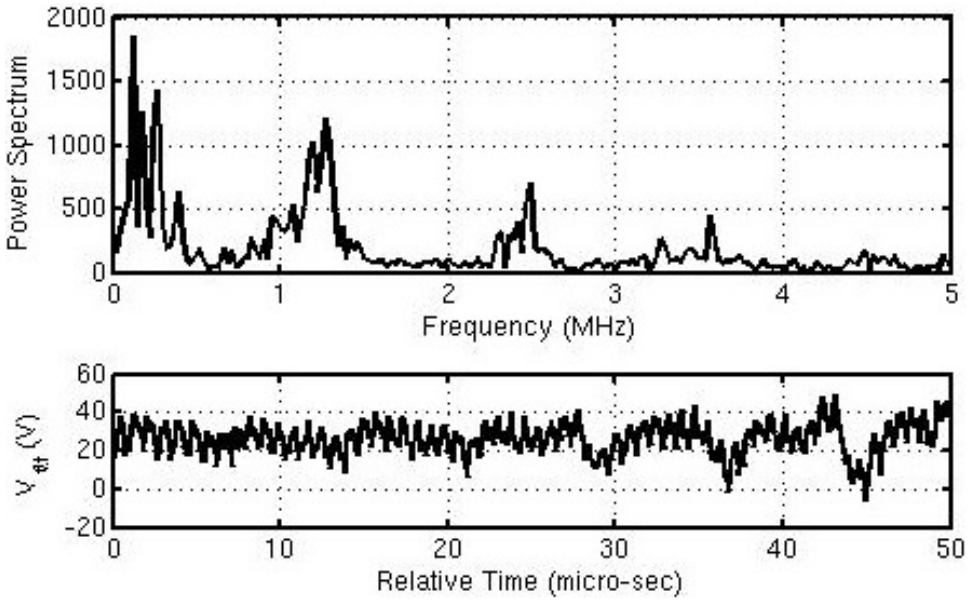

Figure 5-4: The electrostatic signal and power spectrum for the coherent period of the intense high beta HEI instability, previously presented in Figure 4-6. Also note the discrete frequency signal corresponding to coherent frequency chirping.

l	$f_{l,m=1}$ (kHz)	Amplitude $m=1$	Amplitude $m=2$
1	147	1818	1432
2	225	1090	636
3	1215	545	114
4	1340	1045	319
5	1410	1205	682

Table 5.1: Selected frequencies from the wave spectrum in Figure 5-4. The relative amplitudes for both $m = 1$ and $m = 2$ modes are recorded to reconstruct the potential in the form of Equation 5.18.

chirping, are chosen for drift island analysis. The values in Table 5.1 are taken directly from the figure and the amplitudes are later normalized per Equation 5.18. The wave amplitude is considered to be a constant 40 V. Using Equation 5.17 and the lowest order mode frequency from Table 5.1 we calculate that for electrons with energies above $E = \mu B_0$ =13.5 keV this wave spectrum leads to resonant wave-particle interactions.

According to Equation 5.19 this spectrum of waves leads to island overlaps centered around the hot electron ring. Therefore chaos is present in ψ but limited to the pressure peak region and does not extend to the outer wall unless the wave amplitude is very large. In addition, for a given amplitude the chaotic region extends farther in radius in the presence of lower frequency waves as these increase the island width. Experimentally, it is observed that frequency chirping is dominated (both during heating and in the afterglow) by high frequency waves (typically larger than 1 MHz), causing the resonance region to move inward localizing the chaotic region away from the walls and preventing global transport. Thus, the observed wave spectra is consistent with the absence of transport as indicated by a lack of negative current to the ion saturation wall probe during frequency chirping in the intense high beta HEI events.

On the other hand, before frequency chirping begins in the intense high beta HEI events, there does exist a period of lower frequency dominated wave spectra in which incoherent waves appear. Figure 5-5 shows the electrostatic signal and power spectrum of the chaotic period of the intense high beta HEI instability. This raw signal has a large amplitude and the frequency spectrum is clearly dominated by the sub-MHz frequencies. The azimuthal mode number for this portion of the instability is clearly dominated by $m = 1$ and this is true in most experimentally observed cases. To model the spectral content of this event, the frequencies and relative amplitudes of the ten largest peaks from Figure 5-5 are used to construct the potential in the form of Equation 5.18. For this spectrum of waves, drift-resonances exist for electrons with energies below 10 keV and span the radius from the pressure peak to the edge of the plasma. Analysis of the island width shows that this spectrum leads to chaos in ψ over the radial extent of the plasma as long as the amplitude remains above 20 V. This is consistent with the observations of transport from the negative current measured by the ion saturation probe (see Figure 5-1) during the period just before frequency chirping begins.

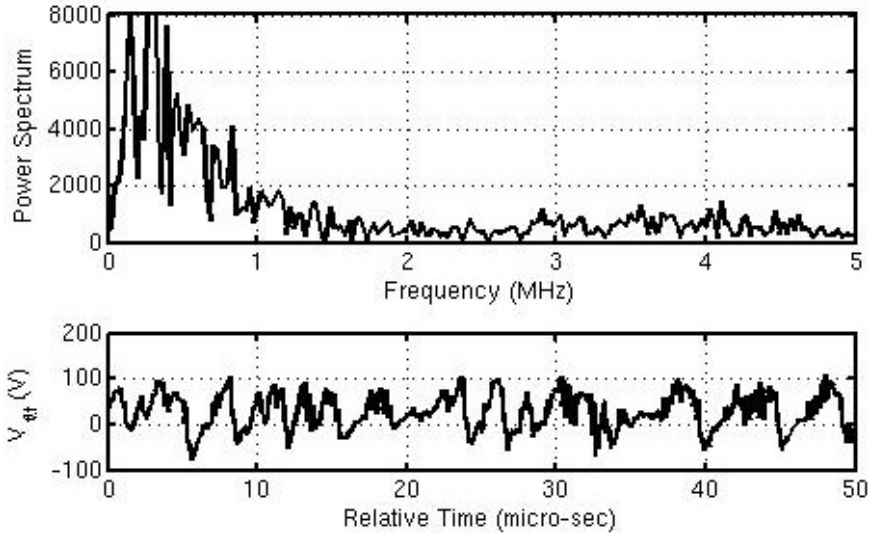

Figure 5-5: The electrostatic signal and power spectrum for the period just before frequency chirping of the intense high beta HEI instability, previously presented in Figure 4-6. This signal has a large amplitude and is dominated by sub-Mhz frequencies.

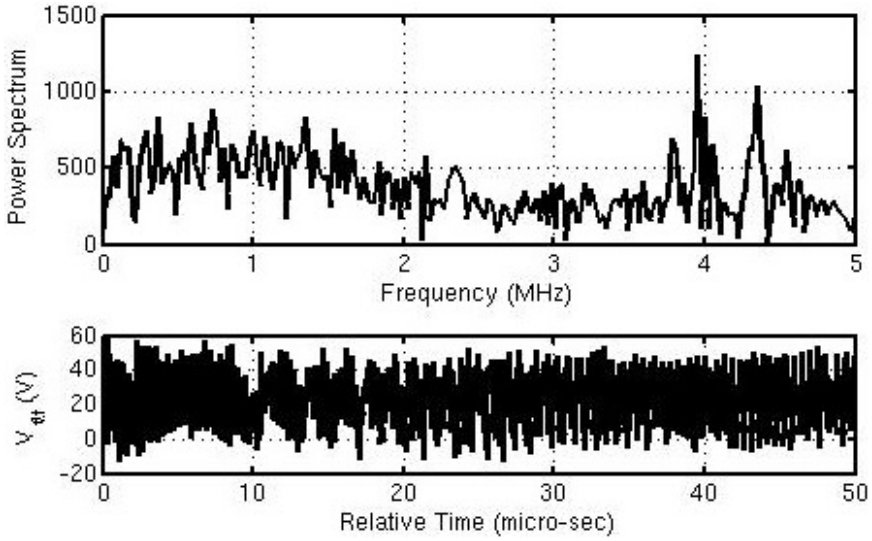

Figure 5-6: The electrostatic signal and power spectrum for the localized high beta HEI instability. High frequency azimuthal modes dominate the spectrum and small wave amplitudes prevent chaos bands from reaching the walls not allowing global transport.

Analysis for Relaxation HEI events

An important point to remember about the relaxation HEI events is that they only appear on the top probe and nothing dramatically changes for any of the mid-plane edge probes. Therefore, before doing an analysis the expectation is that the conditions for global transport will not be met. This is in fact true as can be seen from the wave spectra in Figure 5-6. The presence of higher frequency waves confines chaotic particle motion to narrow regions of phase space, mostly close to the pressure peak. These modes would require larger wave amplitudes in order to stretch out the chaos bands and allow for large scale particle transport. Nevertheless, these HEI events are extremely short-lived and not coincident with any detectable particle transport to the walls.

Analysis for Low Beta HEI events

Finally, we look at the low beta HEI events and compare these to the high beta events and to previous results from CTX. A model fluctuation spectra constructed from Figure 5-7 would clearly be dominated by $m = 1$ modes but would also include $m = 2$ modes. This spectra resembles the incoherent spectra from the intense high beta HEI instability and island width analysis shows that the conditions for global transport are met. This is consistent with the measurements by edge probes, which detect a small negative current during the low beta HEI instability. The quasiperiodic bursts observed during this unstable plasma prevents the plasma from entering into a high beta state. In general, for under fueled plasmas the lower the background pressure the higher the wave amplitude of the instability and this leads to chaotic global transport inhibiting the confinement of particles and the buildup of beta. The relationship between observed fluctuations and particle transport for the low beta HEI instability was covered in detail by Warren [57–59]. His conclusions were: (1) chaos induced by the wave activity in the afterglow is limited in radial extent and consistent with the absence of a wall particle flux, (2) the quasiperiodic bursts observed during ECRH lead to chaotic motion that extends throughout the experimental device, (3) dominant frequency content of the fluctuation is below 2 MHz, (4) azimuthal mode number is limited to m=1 and (5) wave amplitudes greater than 50 V meet the condition for global transport [60].

The conclusions from the analysis of similar fluctuations during the low beta HEI instability in LDX mostly agree with Warren. Yet, some of the points change slightly, specifically

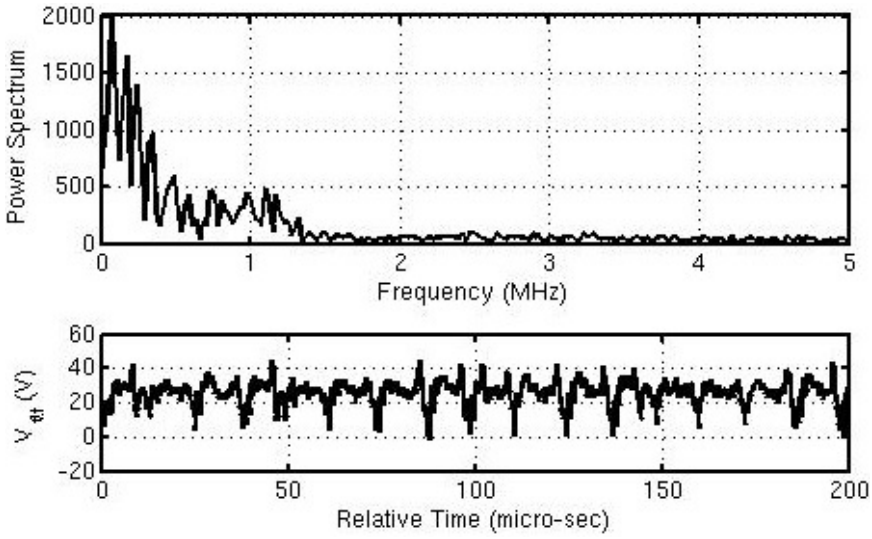

Figure 5-7: The fluctuation spectrum of low beta HEI lead to chaos in ψ over the radial extent of the plasma. In this case $\mu B_0 < 10$ keV but the wave amplitude is sufficient to lead to global transport and prevents the plasma from entering a high beta state.

the values for observed wave amplitudes. For example, the wave amplitude need only be greater than 20 V for the condition of global transport to be met. Higher azimuthal mode numbers contribute to the global chaos but mostly only at higher wave amplitudes. Lastly, with the help of higher background pressure the HEI instability stabilizes and the low beta ECRH plasma evolves into a stable plasma, where the presence of chaotic global transport rapidly declines until it no longer exists.

5.4 Hysteresis in Observed Background Fueling

The HEI instability appears in the three LDX regimes of operation. From Figure 3-1 these are: the unstable low-beta regime, a stable high beta regime, and an afterglow regime when the ECRH power is switched-off. The primary control mechanisms for entering and exiting these three regimes is the level of gas fueling and microwave power applied. A hysteresis in the level of background fueling appears in the transition between a stable high beta plasma and the low-beta regime when the level of heating is maintained constant but the gas fueling

is varied. This hysteresis is described below and occurs as a consequence to the presence of transport during the HEI instability.

Control of the neutral gas pressure has proven to be essential to the achievement and maintenance of high beta discharges in LDX [13]. Experimental results from LDX confirm that trapped electron beta is limited by the 'low-frequency' hot electron interchange instability as cited in other experiments [31, 35, 57]. When the neutral gas is programmed so as to maintain the deuterium gas pressure between about $1-3\times10^{-6}$ Torr, the HEI instability is grossly stable and the fast electron pressure increases by more than a factor of ten. With continuous gas injection, quasi-stationary high beta plasma discharges can be maintained for the length of the microwave heating pulse.

On the other hand, if the experiment is allowed to consume the fuel beyond a critical point (without additional fueling) an intense HEI instability burst will occur leading to a rapid loss of plasma density and causing the plasma to re-enter a low-density regime. Figure 5-8 shows a plasma discharge where low levels of neutral gas fueling lead to five transitions between a low and high beta regime. From top to bottom: (a) shows the vacuum pressure in milli-Torr, the photo diode signal (proportional to background density), the outer flux signal, and the an x-ray intensity detector. Immediately, you can see from the vacuum pressure signal that the plasma enters and exits a high beta state at distinct background pressure levels.

Radial transport induced by the instability creates hysteresis in the neutral gas fueling required to maintain sufficient density to stabilize the high beta HEI mode. Once the pressure threshold is exceeded, the plasma density and visible light abruptly increase and the HEI mode immediately stabilizes. The hysteresis caused by the relationship between plasma density and fast electron stability is shown in Figure 5-8 (b). This pressure threshold depends upon the ECRH power level. At 2 kW, the HEI is stabilized and transition to high beta occurs at a pressure just above 2×10^{-6} Torr. At 4 and 5 kW, the transition pressure are 2.8 and 3.2×10^{-6} Torr.

Once the plasma enters a high beta regime the high beta electrons remain grossly stable so long as the neutral pressure remains above 1×10^{-6} Torr. When the pressure drops below the threshold, the fast electron confinement is destroyed and the plasma density and beta essentially disappear within a few milli-sec. At high beta, the HEI fluctuations can resonate with the drift motion of electrons with high energies $E_h > 100$ keV, whereas at low beta, the fluctuations resonate with lower energy electrons $E_h < 10$ keV.

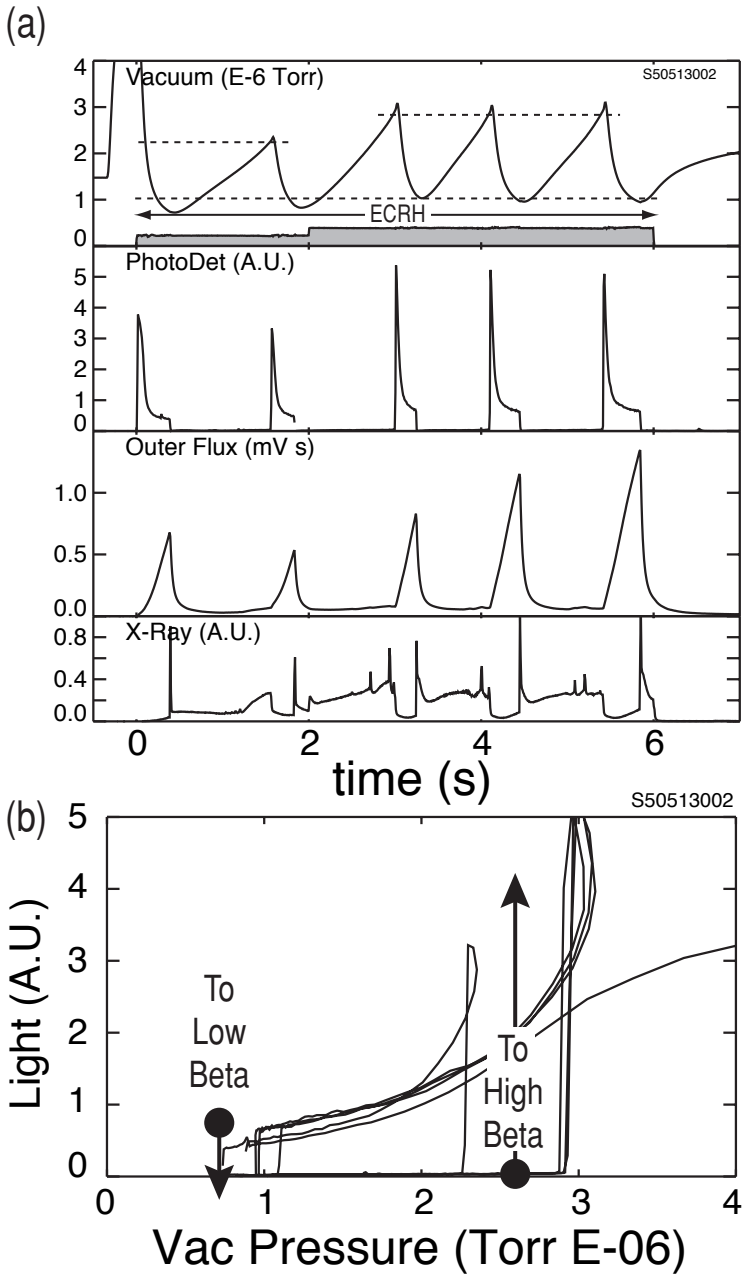

Figure 5-8: In (a) discharge 50513002 is shown in which a series of transitions between high beta and low density operation are caused by the HEI instability. Vacuum pressure, visible light, diamagnetism and x-ray signals are shown. In (b), the evolution of three discharges are shown: one, with higher fueling, is always stable; two, with less fueling has transitions to stability (at $2-3\times10^{-6}$ Torr) and unstable HEI transitions to low beta (at 1×10^{-6} Torr).

5.5 Summary

Plasma transport in the high beta LDX dipole experiment is studied using magnetic and electrostatic diagnostics. Magnetic diagnostics, unfortunately, are affected by eddy currents driven in the experiment's walls. We present a correction for these and apply it to reveal the true rapidly changing magnetic signals. Mirnov coils capture the intense high beta HEI instability and serve as a non-invasive high speed diagnostic for particle transport. Analysis of the Mirnov and corresponding magnetic signals reveals that the magnitude of the fluctuations at the edge significantly exceed the magnitude of the equilibrium field generated by the high beta electrons. Energetic electron confinement ends during the intense high beta HEI instability in under 100 μsec. The interaction between the electrostatic wave and high beta particles is described via a guiding center drift Hamiltonian and the electrostatic waves are modeled as sum of traveling waves. The motion of the particles is analyzed to determine if the condition for chaotic particle motion leads to global transport for a given wave spectrum. During the intense high beta HEI instability the condition for global chaotic transport is met during the incoherent phase, but not during the frequency chirping phase. In addition, local relaxation events do not meet the criterion for global chaotic transport. On the other hand, the low beta HEI instability compares favorably with the CTX results of the same instability although there are a few differences. The wave amplitude necessary for the chaotic global transport condition to be met need not be as high as was found in the CTX results, and multiple modes exist even during the quasiperiodic bursts, albeit, all within a low frequency range. Finally, one of the consequences of the observed high beta transport is the presence of hysteresis in the neutral gas fueling required to stabilize and maintain the high beta plasma. High neutral fueling is required to create a high beta plasma, yet once stabilized, the plasma survives in a high beta state using a lower level of neutral fueling.

Chapter 6

Analysis and Interpretation

The high beta HEI instability has been studied using both electrostatic and magnetic probe diagnostics, which have revealed many new and interesting phenomena. For low beta plasmas a self-consistent, nonlinear, numerical simulation code has been shown to reproduce many key aspects of the HEI instability [36]. This nonlinear simulation was adapted to observe the high beta HEI instability on LDX by setting the proper conditions for LDX parameters, systematically varying the hot electron fraction, and adding a magnetic module that attempts to replicate the observed magnetic diagnostic results.

This chapter is divided into three sections. First, the dispersion relation is calculated for the HEI instability. The results from these calculations are used to interpret experimental observations and simulation results. Second, the nonlinear simulations are interpreted and compared with experimental observations. This represents the first time the code has been run for LDX and the results compared to the high beta HEI instability. Third, the perturbed magnetic response is obtained from the nonlinear simulation code. The theory behind these calculations and initial results are presented.

6.1 MHD Interchange in a Dipole

The original theory, done by Rosenbluth and Longmire [48], described the interchange instability in a linear, cylindrical, axisymmetric geometry with a plasma confined along the axis and periodicity in the $z-$direction. This section adapts this theory for a dipole geometry. We start with basic MHD equations and the equation of state

$$nM_i \frac{d\mathbf{V}}{dt} = -\nabla P + \mathbf{J} \times \mathbf{B} \tag{6.1}$$

$$\frac{\partial n}{\partial t} + \nabla \cdot n\mathbf{V} = 0 \tag{6.2}$$

$$\mathbf{E} + \mathbf{V} \times \mathbf{B} \approx \mathbf{0} \tag{6.3}$$

$$\nabla \cdot \mathbf{J} \approx 0 \tag{6.4}$$

$$\frac{d}{dt}\left(\frac{P}{n^\gamma}\right) = 0. \tag{6.5}$$

Here d/dt is the convective derivative and the plasma pressure is assumed to be isotropic, $P = nkT$. Equation 6.5 represents a "local" adiabatic closure. The plasma current from Equation 6.1 is

$$\mathbf{J} = \frac{\mathbf{B} \times \nabla P}{B^2} + \frac{nM_i}{B^2}\mathbf{B} \times \frac{d}{dt}\left(\frac{\mathbf{B} \times \nabla \Phi}{B^2}\right). \tag{6.6}$$

The first term in Equation 6.6 is called the diamagnetic current and the second is the polarization current.

For low-frequency interchange motion the perturbed electric field is taken to be related to the electrostatic potential, $\Phi(\psi, \varphi)$, which is constant along a field line. $\Phi(\psi, \varphi, t)$ is a measure of the rate of cross-field plasma flow, $\mathbf{V}$. Equation 6.3 implies

$$\mathbf{V} = -\frac{\nabla \varphi}{|\nabla \varphi|^2}\frac{\partial \Phi}{\partial \psi} + \frac{\nabla \psi}{|\nabla \psi|^2}\frac{\partial \Phi}{\partial \varphi} \tag{6.7}$$

Which gives a divergence of the flow of

$$\nabla \cdot \mathbf{V} = -\frac{\partial \log B^2}{\partial \psi}\frac{\partial \Phi}{\partial \varphi}. \tag{6.8}$$

Therefore, axisymmetric flow is always incompressible, and non-axisymmetric flow is always compressible. Following Mauel's [42] method, a local approximation for the perturbed potential is

$$\Phi(\psi, \varphi, t) \approx \Re\left\{\Phi_m e^{-j(\omega t - m\varphi)}\left(1 - \frac{(\psi - \psi^*)^2}{(\Delta\psi)^2} + ...\right)\right\} \tag{6.9}$$

where $\Delta\psi \equiv 2\psi^*/k_L L$ is a measure of the radial width of the perturbed potential, and ψ^* is the radial location of the potential peak, and L is the equatorial radial position of the resonant flux surface.

Since interchange motion in a dipole is two-dimensional it is useful to define the number of particles on a flux-tube, $N(\psi, \varphi, t) \equiv \langle n \rangle \delta V$, where $\langle A \rangle$ is the flux tube average of A defined in the Appendix, Chapter 8. Continuity, Equation 6.2, can then be rewritten as

$$\frac{\partial N}{\partial t} - \frac{\partial}{\partial \varphi}\left(N\frac{\partial \Phi}{\partial \psi}\right) + \frac{\partial}{\partial \psi}\left(N\frac{\partial \Phi}{\partial \varphi}\right) = 0 \tag{6.10}$$

If the density is axisymmetric and the number of particles on the flux tube is constant then any interchange motion leaves N unchanged.

The flux-tube integral of $\nabla \cdot \mathbf{J}$ transforms Equation 6.4 into

$$\begin{aligned}\delta V \langle \nabla \cdot \mathbf{J} \rangle = &-\frac{\partial}{\partial \varphi}\left(\delta V \frac{\partial P}{\partial \psi}\right) + \frac{\partial}{\partial \psi}\left(\delta V \frac{\partial P}{\partial \varphi}\right) \\ &- \frac{\partial}{\partial \varphi}\int \frac{d\chi}{B^2}\epsilon_\varphi \nabla\psi \cdot \frac{d}{dt}\left(\frac{\mathbf{B}\times\nabla\Phi}{B^2}\right) \\ &+ \frac{\partial}{\partial \psi}\int \frac{d\chi}{B^2}\epsilon_\psi \nabla\varphi \cdot \frac{d}{dt}\left(\frac{\mathbf{B}\times\nabla\Phi}{B^2}\right)\end{aligned} \tag{6.11}$$

where the appropriate components of the plasma dielectric constant are $\epsilon_\varphi/\epsilon_0 = (\omega_{pi}^2/\omega_{ci}^2)$ $|\nabla\varphi|^2$ and $\epsilon_\psi/\epsilon_0 = (\omega_{pi}^2/\omega_{ci}^2)|\nabla\psi|^2$. Since $\omega_{pi}^2/\omega_{ci}^2 \gg 1$, the polarization current induced by a relatively small fluctuating potential can cancel the perturbed diamagnetic current as required by the MHD approximation.

MHD instability is analyzed by linearizing Equations 6.5, 6.10, and 6.11 using the local approximation for Φ in Equation 6.9. The perturbed density is

$$N_m \approx \frac{m}{\omega}\Phi_m \frac{\partial N}{\partial \psi}. \tag{6.12}$$

The MHD condition on the perturbed current is found by taking a linear form for the convective derivative, $d/dt \approx \partial/\partial t$. This gives

$$\frac{\partial}{\partial t}\left(\frac{\partial}{\partial \varphi}\bar{\epsilon}_\varphi \frac{\partial \Phi}{\partial \varphi} + \frac{\partial}{\partial \psi}\bar{\epsilon}_\psi \frac{\partial \Phi}{\partial \psi}\right) = -\frac{\partial}{\partial \varphi}\left(\delta V \frac{\partial P}{\partial \psi}\right) + \frac{\partial}{\partial \psi}\left(\delta V \frac{\partial P}{\partial \varphi}\right) = \frac{\partial \delta V}{\partial \psi}\frac{\partial P}{\partial \varphi}. \tag{6.13}$$

Notice that $\partial\delta V/\partial\psi = 2\langle\kappa_\psi\rangle\delta V$ where $\hat{b}\cdot\nabla\hat{b} = \kappa_\psi\nabla\psi$ is the magnetic curvature.

Assuming a reasonable density profile (example $n/\langle n\rangle \propto \sin\theta$) the dielectric functions in Equation 6.13 are

$$\begin{aligned}\bar{\epsilon}_\varphi &= 0.57\epsilon_0\left(\frac{\omega_{pi}^2}{\omega_{ci}^2}\right)_0\frac{\delta V}{L^2} \propto \frac{N}{\psi^4}\\ \bar{\epsilon}_\psi &= 1.5\ \epsilon_\varphi\psi^2 \propto \frac{N}{\psi^2}\end{aligned}$$

where $\epsilon_0(\omega_{pi}^2/\omega_{ci}^2)_0$ is the plasma dielectric constant at the equatorial midplane.

Using the local approximation for Φ, Equation 6.9, Poisson's equation is

$$-m^2\bar{\epsilon}_\varphi\Phi_m + \bar{\epsilon}_\psi\frac{\partial^2\Phi_m}{\partial\psi^2} \approx -\frac{m}{\omega}P_m\frac{\partial\delta V}{\partial\psi},$$

which is equivalent to

$$\Phi_m \approx \frac{m}{m_\perp^2}\frac{P_m}{\omega\bar{\epsilon}_\varphi}\frac{\partial\delta V}{\partial\psi}, \tag{6.14}$$

where $m_\perp^2 \equiv m^2 + (\bar{\epsilon}_\psi/\bar{\epsilon}_\varphi)(k_L L)^2/(2\psi^*)^2$. Equation 6.14 expresses the perturbed electric field that results from an azimuthal pressure perturbation, mP_m, and the dipole's magnetic field curvature, $\partial\delta V/\partial\psi$.

The condition for linear MHD instability requires knowledge of the closure condition relating the perturbed pressure and the perturbed density. For this derivation assume that the interchange motion in a dipole occurs slowly so that the pressure remains isotropic. That is particles, especially electrons, bounce rapidly enough along a field line to keep both n and P constant along the field line. Therefore the local adiabatic closure in Equation 6.5 can be replaced by the "flux-tube" condition, $d(P/\bar{n}^\gamma)/dt = d[P/(N/\delta V)^\gamma]/dt = 0$. Then the linearized closure condition for ideal MHD in a dipole is

$$P_m = \frac{\gamma P}{\bar{n}}\bar{n}_m = \frac{\gamma P}{N}N_m. \tag{6.15}$$

The pressure increases when the number of particles within a flux tube increases. Therefore, MHD instability in a dipole is determined by the condition, obtained by combining

Equations 6.12, 6.14, and 6.15,

$$\omega^2 = \frac{m^2}{m_\perp^2 \bar{\epsilon}_\varphi} \frac{\gamma P}{N} \frac{\partial N}{\partial \psi} \frac{\partial \delta V}{\partial \psi}$$

$$= \frac{m^2}{m_\perp^2 \bar{\epsilon}_\varphi} \frac{1}{\delta V^\gamma} \frac{\partial}{\partial \psi} (P \delta V^\gamma) \frac{\partial \delta V}{\partial \psi}. \tag{6.16}$$

Here, a negative frequency, ω, implies the plasma is unstable to MHD interchange modes whereas a positive frequency implies stability. The sign of ω is determined by the product of $\partial \delta V / \partial \psi$ and $\partial (P \delta V^\gamma)/\partial \psi$. For a dipole $\partial \delta V / \partial \psi = -4 \delta V / \psi^* < 0$ and is always negative due to the dipole's inherent bad curvature. The stability of the plasma therefore depends on the sign of $\partial (P \delta V^\gamma)/\partial \psi$. When $P \delta V^\gamma$ increases in the $-\hat{r}$ direction the plasma is stable to MHD interchange modes. These results were first stated for a dipole by Gold [16].

If we let $P \delta V^\gamma \propto (\psi/\psi^*)^\alpha$ (equivalently, if $P(L) \propto 1/L^{4\gamma+\alpha}$), then Equation 6.16 becomes

$$\omega = \pm j 2\sqrt{\alpha} \frac{m}{m_\perp} \frac{C_s}{L}, \tag{6.17}$$

where $C_s^2 = P/\bar{n} M_i$ is the sound speed. MHD interchange instabilities grow rapidly at a rate proportional to the sound transit time across a dipole plasma. The rapid growth of MHD interchange in a dipole plasma is consistent with MHD orderings. Ideal MHD is associated with large electric fields, which are equivalent to small gyro radii and near sonic flows.

6.2 The HEI Dispersion Relation

The HEI instability occurs in "two-component" plasmas; that is plasmas that contain a population of magnetically-trapped hot electrons in addition to their background electron population with $T_e \sim T_i$. The HEI mode has been examined in detail, and good agreement has been found between theory and measurement. The HEI instability was first described mathematically by Krall [31] who used a "gyrokinetic-like" approach. From this approach two important physical effects are observed to occur: (1) the interchange mode acquires a real frequency, and (2) the traveling-wave instability resonates with particle drift motion. The following summarizes derivations for the HEI dispersion relation found in References [35,42].

The starting point for the derivation of the HEI is the gryokinetic equation for collision-

less, deeply trapped electrons interacting with low-frequency flute-modes.

$$\frac{\partial F}{\partial t} + \frac{\partial}{\partial \varphi}\left(\omega_d(\mu, J, \psi) - \frac{\partial \Phi}{\partial \psi}\right) F + \frac{\partial}{\partial \psi}\left(\frac{\partial \Phi}{\partial \varphi} F\right) = 0 \tag{6.18}$$

Here, $F(\mu, J, \psi, \varphi, t)$ is the trapped electron distribution function. Equation 6.18 describes the drift dynamics of the electrons on times scales that are long compared with the particle's bounce period. The first two adiabatic invariants, μ and J, are constant as the particle drifts from field-line to field-line. In fact the hot electrons are so deeply trapped we can set $J = 0$ and look only at dynamics in the equatorial plane. The motion of the anisotropic electron is described in a two-dimensional phase-space, (ψ, φ) and the electron distribution has been treated as a "disk" with F $\propto \delta(J)$. The magnetic drift frequency is $\omega_d \approx (\mu/e)\partial B/\partial \psi$, and is independent of J.

Given that the pressure is localized to the dipole equator, the diamagnetic current is constrained to flow within the equatorial plane. The "diamagnetic surface current" is $\mathbf{K} \equiv \int d\chi \mathbf{J}/B^2$. The components of $\mathbf{K}$ (with $\theta = \pi/2$) are

$$K_\varphi = -|\nabla \psi| \int d\mu dJ \mu \frac{\partial F}{\partial \psi} \tag{6.19}$$

$$K_\psi = |\nabla \varphi| \int d\mu dJ \mu \frac{\partial F}{\partial \varphi}. \tag{6.20}$$

The equilibrium currents from $\mathbf{K}$ are sufficiently weak so that the field from the point-dipole dominates. The derivation below assumes low $\beta_\perp$.

The linear dispersion relation for low-frequency, flute-like modes in a hot electron dipole plasma can be derived using several simplifcations. First, the electron distribution function is assumed to be separable, $F = F_\circ + \tilde{F}$, with a fractional density of energetic electrons. Secondly, solutions to Poisson's equation are restricted to be traveling waves localized on a flux surface where $\partial \Phi/\partial \psi \approx 0$ [42]. With these assumptions the unperturbed electron distribution function $F_\circ$ takes the form

$$F_\circ(\mu, J, \psi) = N_{i\circ}(\psi)[1 - \alpha_h(\psi)]\delta(\mu)\delta(J) + N_{i\circ}(\psi)\alpha_h(\psi)G(\mu)\delta(J). \tag{6.21}$$

$\alpha_h(\psi)$ is the fraction of energetic electrons, $(1 - \alpha_h)$ is the fraction of cold electrons, and

$N_{io} = N$ is the number of ions per unit flux tube. Similarly, the number of electrons on a tube of unit flux is $N_e = \int d\mu dJF$. $G(\mu)$ is the distribution of electron energies, given as

$$G(\mu) = \frac{\mu^{l-1} l^l}{\mu_0^l \Gamma(l)} \exp(-\mu l/\mu_0),$$

where l is a positive integer. $G(\mu)$ becomes a delta function (mono-energetic) for $l \to \infty$ and a Maxwellian distribution of energetic electrons at $l = 1$. For any integer value of l, $\int d\mu \, \mu G = \mu_0$.

The divergence of the induced electron current results from linearization of Equation 6.18 and the unperturbed electron distribution function in Equation 6.21. The time harmonic form is

$$\frac{\partial \tilde{N}_e}{\partial t} \to -j\omega \tilde{N}_e = -j\omega \int d\mu dJ \tilde{F} = -jm\Phi_m \frac{\partial N}{\partial \psi} - jm\Phi_m \frac{\partial N_h}{\partial \psi} \int d\mu \frac{m\omega_d G(\mu)}{\omega - m\omega_d}$$

and

$$\tilde{N}_e = \frac{m}{\omega} \Phi_m \frac{\partial N}{\partial \psi} + m^2 \Phi_m \frac{\partial N_h}{\partial \psi} \int d\mu \frac{\omega_d G(\mu)}{\omega(\omega - m\omega_d)} \tag{6.22}$$

where the local approximation, in Equation 6.9, is used and $N_h = \alpha_h N$. The first term on the right hand side is the background density gradient term. The second term is the hot electron interchange drive term, exhibiting the drift-wave resonance in the denominator.

The magnetic drift motion of the energetic electrons causes a "charge separation" to occur in the presence of a fluctuating electric field. The ion and electron currents induced by $\mathbf{E} \times \mathbf{B}$ motion no longer cancel. The MHD constraint $\nabla \cdot \mathbf{J} = 0$ becomes

$$\langle \nabla \cdot \mathbf{J} \rangle = \langle \nabla \cdot \mathbf{J}_{pol} \rangle + \langle \nabla \cdot \mathbf{J}_{\mathbf{E}} \rangle = 0 \tag{6.23}$$

where $\mathbf{J}_{pol}$ is the polarization current and $\mathbf{J}_E$ is the net current caused by $\mathbf{E} \times \mathbf{B}$ drifts and where

$$\delta V \langle \nabla \cdot \mathbf{J}_{pol} \rangle = \frac{\partial}{\partial t} \left(\frac{\partial}{\partial \varphi} \bar{\epsilon}_\varphi \frac{\partial \Phi}{\partial \varphi} + \frac{\partial}{\partial \psi} \bar{\epsilon}_\psi \frac{\partial \Phi}{\partial \psi} \right). \tag{6.24}$$

The continuity equation, Equation 6.2, gives the divergence of the ion $\mathbf{E} \times \mathbf{B}$ flow,

$$-\delta V \langle \nabla \cdot \mathbf{J}_E \rangle = e \left(\frac{\partial \tilde{N}_i}{\partial t} - \frac{\partial \tilde{N}_e}{\partial t} \right). \tag{6.25}$$

After some algebraic manipulation of Equation 6.23 the HEI dispersion relation is found to be

$$-m^2\bar{\epsilon}_\varphi\Phi_m + \frac{\partial}{\partial\psi}\bar{\epsilon}_\psi\frac{\partial\Phi_m}{\partial\psi} = em\Phi_m\frac{\partial N_h}{\partial\psi}\int d\mu\frac{m\omega_d G(\mu)}{\omega(\omega - m\omega_d)}. \tag{6.26}$$

For cold electrons $G(\mu) = \delta(\mu)$ and the charge separation term on the right hand side vanishes. Since $\partial\Phi_m/\partial\psi = 0$ at ψ^*, the HEI dispersion relation is Equation 6.26 evaluated at $\psi = \psi^*$,

$$D(\mu, m, m_\perp, \psi^*) = 1 + \frac{m^2}{m_\perp^2}\frac{e}{\bar{\epsilon}_\varphi}\frac{\partial N_h}{\partial\psi}\int d\mu\frac{\omega_d G(\mu)}{\omega(\omega - m\omega_d)}. \tag{6.27}$$

For reasonable profiles, $e/\bar{\epsilon}_\varphi \sim 1.5\omega_{ci}\psi/N$ [42]. Following Krall [31], a particularly useful form of Equation 6.27 results when $G(\mu) = \delta(\mu - \mu_\circ)$ and $\omega_d = (\mu_\circ/e)\partial B/\partial\psi$. Then,

$$\omega = \frac{m\omega_d}{2} \pm j\frac{m}{m_\perp}\sqrt{\Gamma_h^2 - \frac{m_\perp^2\omega_d^2}{4}}, \tag{6.28}$$

where the hot electron interchange drive, Γ_h, is defined as

$$\Gamma_h^2 = 1.5\omega_{ci}\omega_d\frac{\psi}{N}\frac{\partial N_h}{\partial\psi}.$$

The high frequency of the HEI causes a strong stabilizing polarization current. Instability results when density (and pressure) gradients exceed a threshold steeper than the usual MHD condition. Instability requires $\Gamma_h^2 > m_\perp^2 w_d^2/4$, or

$$\frac{\psi}{N}\frac{\partial N_h}{\partial\psi} > 0.17m_\perp^2\frac{\omega_d}{\omega_{ci}}. \tag{6.29}$$

If $N_h \propto \psi^\alpha$, so that $\bar{n}_h \propto 1/L^{4+\alpha}$ and $P_\perp = B\int d\mu dJ\mu F = \mu B\bar{n}_h \propto 1/L^{7+\alpha}$, then the condition for instability is $\alpha > 0.17m_\perp^2\omega_d/\omega_{ci} \times (N/N_h)$. When the fractional density of fast electrons is small, then the electrons remain stable even when they are radially localized. For profiles that are marginally unstable, the $m = 1$ mode is always the most unstable mode. For strongly unstable plasmas $\Im(\omega) \sim m/m_\perp$, and the HEI grows as

$$\omega \sim \frac{m\omega_d}{2} \pm j1.2\sqrt{\alpha}\frac{m}{m_\perp}\frac{C_s}{L}\sqrt{\frac{N_h}{N}}, \tag{6.30}$$

where $C_s/L = \sqrt{\omega_d\omega_{ci}}$. Equation 6.30 and the usual MHD condition show that the growth

rate for the strong HEI instability is *slightly reduced* relative to the usual MHD growth rate, Equation 6.17, by the factor $\sqrt{N_h/N}$.

The HEI instability is different from the MHD interchange instability since it propagates in the direction of the electron drift. Hot electrons on field lines $L \sim \sqrt{2}L^*$, where L^* is the equatorial radius of the resonance peak, drift resonate with the instability's circulation since $\omega_d(\mu, \psi) \propto \psi^2$. Realistically, $G(\mu)$ is not narrowly peaked, and drift resonance is present radially across the plasma. Drift resonance strongly influences the nonlinear development of the HEI.

The HEI instability can saturate quasilinearly through drift-resonant wave-particle trapping. The adiabatic release of hot electron energy is converted to electrostatic (or "convective") energy. Berk *et. al.* [5] describe the occurrence of spontaneous frequency sweeping after a period of explosive growth of the resonant particle instability near threshold [31]. Resonant particle instabilities with linear growth rates that are only marginally larger than their rates of non-resonant dissipation exhibit unexpected behaviors at saturation. When the dynamics of the resonant particles are sufficiently collisionless, Berk's kinetic simulations showed the spontaneous formation of phase-space structures or "holes" and "clumps" [5]. The rising and falling tones are attributed to each, respectively.

In the following section the time evolution of the HEI instability is simulated using HEISIM, a nonlinear, self-consistent simulation code developed by Mauel [42] for CTX and later adapted for LDX parameters. The simulation explicitly solves for the cold ion and energetic electron number densities and the electrostatic potential $\Phi(\psi, \varphi)$. Plasma E $\times$ B, ion polarization and energetic electron magnetic drifts determine particle dynamics, and Poisson's equation in magnetic coordinates determines the nonlinear evolution of the potential. A complete explanation of the model equations used and numerical procedures applied to solve the simulation code is given elsewhere [35, 36, 39, 41, 42]. In the following section only the relevant LDX initial conditions and results from the simulation will be discussed and compared with measurement.

6.3 Nonlinear Simulation of the HEI Instability

A self-consistent, nonlinear, gyro-kinetic numerical simulation has been used to model the HEI instability. The simulation results can be used to explain the strong spatial modulations

of resonant electrons and frequency sweeping. The simulation reproduces nonlinear frequency sweeping and the radial structure of the modes. It also illustrates spontaneous creation and inward propagation of phase-space "holes" during the saturation process.

6.3.1 Scaling Results

The adapted HEISIM code for LDX can be used to study the HEI instability under various plasma conditions. For example, the relationship between plasma volume and the instability is explored by varying the boundary conditions. Results for a full and reduce sized plasma are presented below in Figures 6-1 and 6-2. The initial conditions are 25% hot electrons, peak temperature of 25 keV, and a radially-localized density profile peaked near the peak of the energetic electron density $R_o = 77.5$ cm (c). Both runs are highly unstable and demonstrate interesting nonlinear behavior.

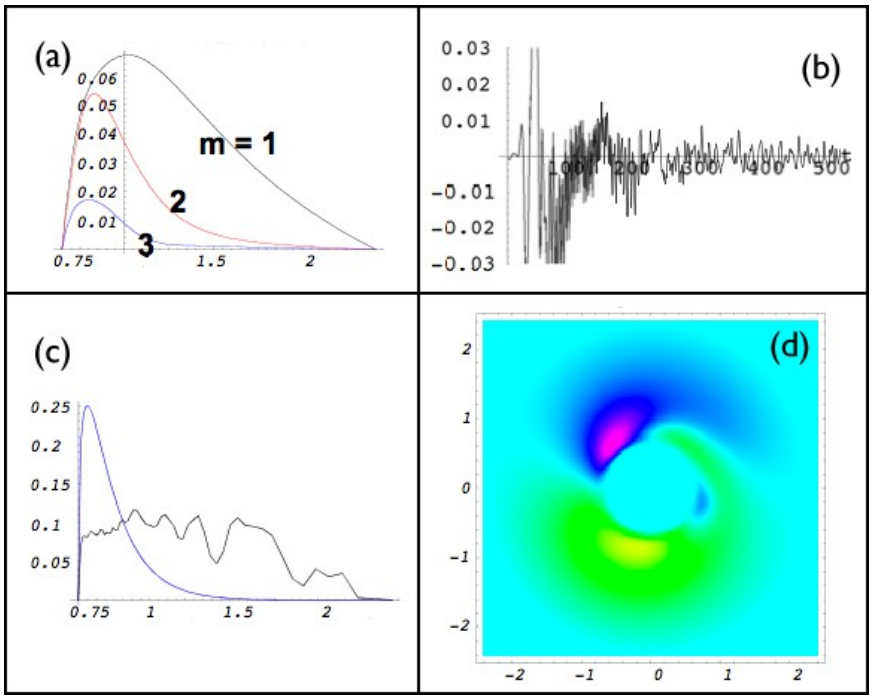

Figure 6-1: Simulation results for a full sized plasma with 25 keV hot electrons. (a) HEI radial mode structure, (b) electrostatic potential, (c) initial and final N_h, and (d) instability potential contour.

In the full sized plasma simulation the modeled density profile extends to the walls of the vacuum chamber as is visible in Figure 6-1 (c). The simulation shows that frequency chirping resonates with the drift motion of the hot electrons occurs as the instability develops. In this full sized plasma the growth rate of the chirping frequency is very fast and the mode saturates before disappearing by 400 μsec (b). The mode structure of the instability is dominated by $m = 1$ mode as is clearly evident from (a) and (d). The end result of this instability is to flattened out the peaked hot electron density profile in (c), re-distributing the hot electrons across outer and inner flux tubes.

In the reduced sized plasma the modeled density profile extends half way to the vacuum chamber wall as is shown in Figure 6-2 (c). The resulting instability is now dominated by an $m = 2$ mode as is seen from (a) and (d). Frequency chirping is again detected in (b) but the growth rate is much smaller than before. In fact, the instability continues to chirp at 500 μsec but at a lower frequency than observed for the full-sized plasma case. Again the peaked density profile becomes flat (c) as a result of the instability.

From these simulation comparisons it is clear that the plasma size matters when it comes to the nonlinear behavior of the HEI instability. For smaller plasma size the higher order modes seem to dominate, the growth rates of the instability are smaller and the overall frequency level appears to be lower. Although experiments for the full sized plasma confirm the observation that the $m = 1$ mode dominates, no HEI instabilities were captured during smaller plasma sized experiments. It is possible, though, to explore these relationships further through experiment by using the LDX Helmholtz shaping coils, a topic for further research.

6.3.2 Hot Electron Fraction Results

Earlier a gyrokinetic dispersion relation for the HEI mode was derived for the case when the electron distribution function, $F_0(\mu, J, \psi)$, was separable into an adiabatic part and a part that varied only in ψ. For this case, the local stability condition for the HEI mode, first obtained by Krall [31], was given by Equation 4.1 and is now plotted below in Figure 6-3. Instability only occurs when the energetic electron density gradient exceeds a threshold beyond the usual MHD stability limit for an isotropic and Maxwellian pressure profile.

From Figure 6-3 we see that the stability of the hot electron component depends on the

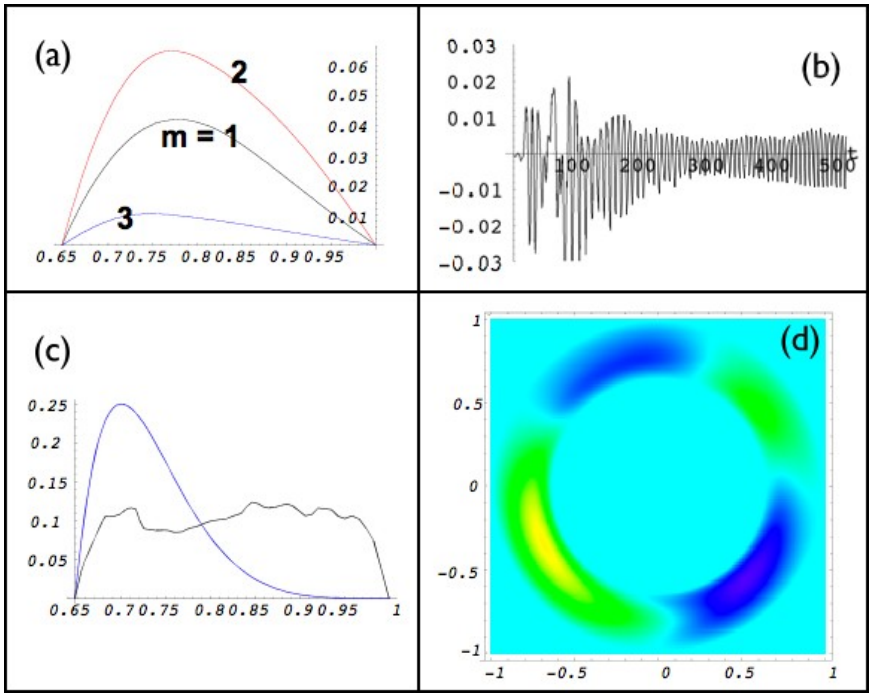

Figure 6-2: Simulation results for a reduced sized plasma with 25 keV hot electrons. (a) HEI radial mode structure, (b) electrostatic potential, (c) initial and final N_h, and (d) instability potential contour.

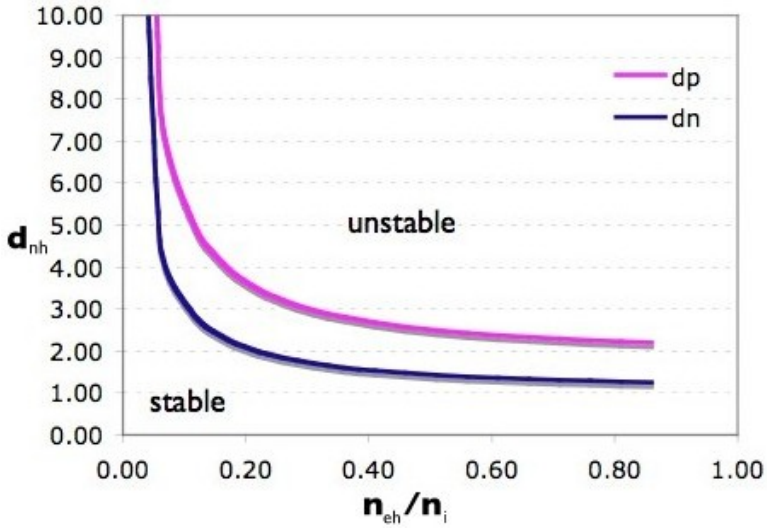

Figure 6-3: Krall stability solution for $\omega_{ci}/\omega_{dh} = 2.2, \eta = 0.75$ and $m = 1$. In the graph above the gradient of the hot electron density is plotted as a function of the fraction of hot electrons to give a marginal stability frontier defined by Equation 4.1.

density ratio of the warm to the hot electron plasma or hot electron fraction, n_{eh}/n_i, as well as the hot electron density gradient, $d_{nh} \equiv -d\ln n_h/d\ln V$. For a sufficiently high hot electron fraction the HEI mode can be excited. Next we take a look at four cases in which the hot electron fraction is varied as an input to the simulation code.

Figure 6-4 shows the initial and final states of the highly steeped density profiles, peaked at the 2.45 GHz resonance, for the four simulated cases each representing a different hot electron fraction. The selected cases are (a) 35%, (b) 45%, (c) 55% and (d) 75%. The four simulation are done assuming a 300 A charge in the F-coil and a 50 keV hot electron energy, typical values from the experiment.

Three important results can be seen from the simulation of these four cases. First, Figure 6-6 shows a plot of the electrostatic potential of the plasma during the HEI instability. At 75% hot electron fraction the mode is characterized by a rapid growth rate and very high frequency chirping. Yet at 35% hot electron fraction the HEI mode barely changes. The growth rate of the mode (*i.e.* how quickly frequency sweeping rises) increases with the hot electron fraction.

Second, Figure 6-5 shows the log amplitude for each case. The solid plotted line is the

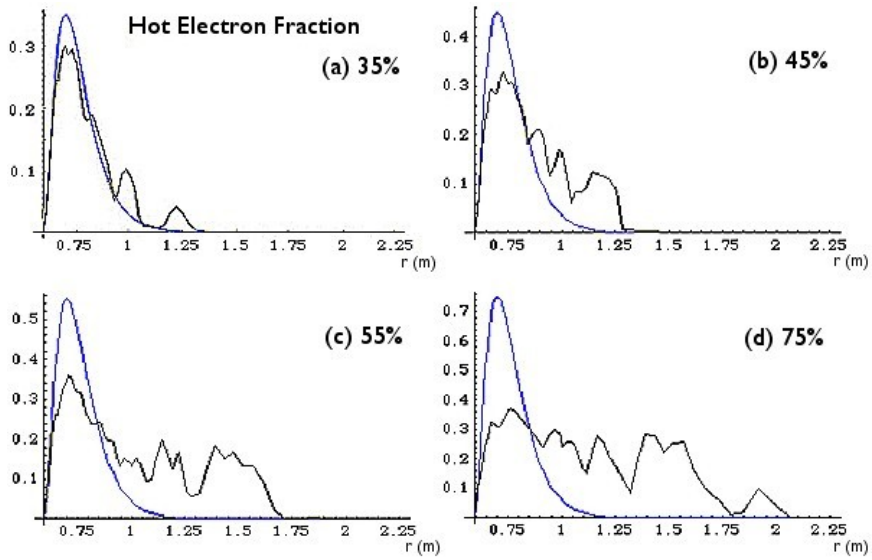

Figure 6-4: Hot Electron Fraction. Initial and final states of simulated cases representing four different hot electron fractions, n_{eh}/n_i. A larger initial hot electron fraction leads to increased transport by the HEI instablity.

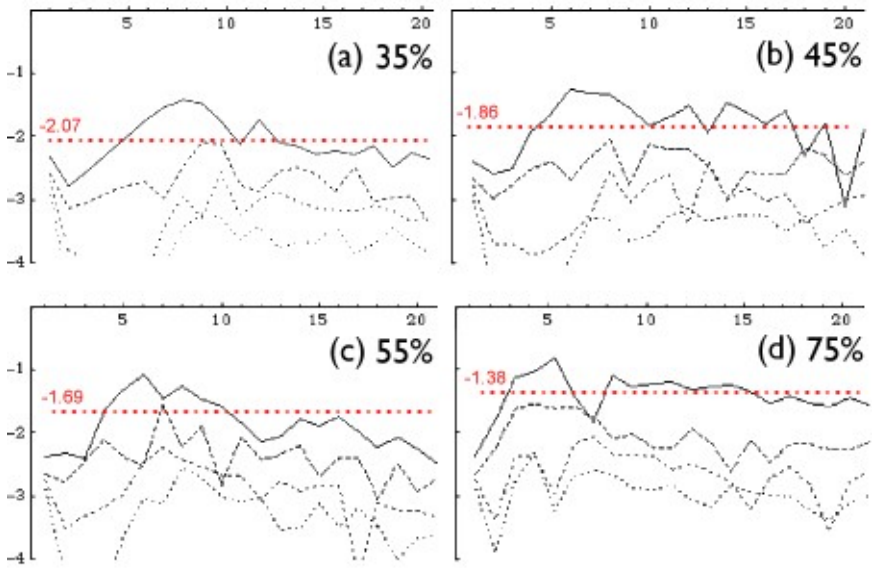

Figure 6-5: Log Mode Amplitude. The log of the mode amplitude behaves differently depending on the hot electron fraction.

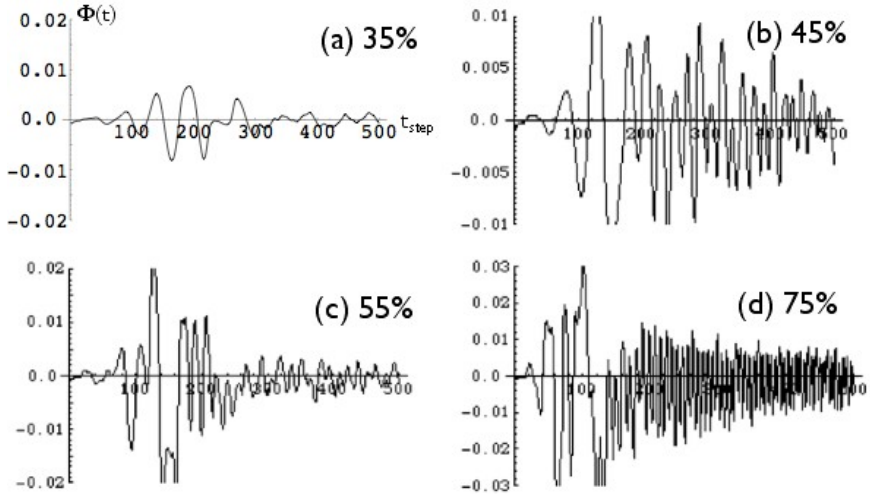

Figure 6-6: Electrostatic Potential. Simulation results of the electrostatic potential at different hot electron fractions plotted as a function of time. Frequency sweeping is clearly observed and the growth rate of the instability rises with increasing hot electron fraction.

$m = 1$ mode amplitude and the over-plotted dotted red line indicates the median value of this mode over the selected time period. Notice that the saturated amplitude increases with increasing hot electron fraction.

Third, Figure 6-4 shows the radial profile of the density, at one azimuthal location, changes from the beginning to the end of the run for all cases. The most drastic change occurs for the case with the highest hot electron fraction suggesting that that transport rises with hot electron fraction. It also confirms experimental observations that the HEI restricts the buildup of the hot electron population when the hot electron fraction is high, *i.e.* $n_{eh}/n_i > 0.5$. In the experiment this condition exists when we operate in a low density highly unstable plasma.

6.4 Magnetics Simulation Comparison

The HEISIM code was originally created to simulate the dynamics of the electrostatic HEI instability. In general, if the diamagnetic currents generated by the fast electrons are not too large, this code can calculate the perturbed magnetic response during instability. In

Chapter 5 we saw that the HEI instability disturbs and rearranges the high beta trapped electrons. This perturbed fast electron pressure creates large perturbations to diamagnetic currents that are detected by Mirnov coils. In theory these experimental observations from the Mirnov coils can be compared to the magnetic calculations using a modified HEISIM code. In this section we derive the necessary equations to add a magnetic perturbation module that will take the HEISIM calculated diamagnetic currents and output the δB_θ. Initial results from this module are also presented.

6.4.1 Magnetic Module

HEISIM assumes the hot electrons are strongly anisotropic, $P_\perp \gg P_\parallel$. In this case, the current density is a localized disk on the equatorial plane of the dipole and can be related to the gradients of the hot electron pressure for $\theta = 0$

$$J_\phi = -2\pi r \frac{\partial P_\perp}{\partial \psi} + 2\pi r P_\perp \frac{\partial}{\partial \psi} \ln B = -2\pi r B \frac{\partial}{\partial \psi}\left(\frac{P_\perp}{B}\right) \tag{6.31}$$

$$J_\psi = \frac{1}{rB}\frac{\partial P_\perp}{\partial \phi} \tag{6.32}$$

and the equatorial surface current density on a current sheet, $\mathbf{K}$, is obtained by integrating along a field-line

$$\mathbf{K} = \int ds\ \mathbf{J} = \int \frac{d\chi}{B^2} B\mathbf{J} \tag{6.33}$$

$\mathbf{K}$ is a vector field in the plane of the dipole's equator. Therefore, the perturbed magnetic response is entirely in the poloidal direction.

In HEISIM the number of electrons having magnetic moment, μ_k, is computed as $N_k(\psi, \phi)$ for any field-line labeled (ψ, ϕ). The field-line integrated magnetization can be defined as

$$H_\perp(\psi, \phi) \equiv \int \frac{d\chi}{B^2}\frac{P_\perp}{B} = \sum_k \mu_k N_k(\psi, \phi). \tag{6.34}$$

Using this definition, the gradients needed to compute $\mathbf{K}$ can be found by taking $\partial H_\perp / \partial \psi$

and $\partial H_\perp/\partial\phi$. $\mathbf{K}$ then becomes

$$K_\phi = -rB^2 \sum_k \mu_k \frac{\partial N_k}{\partial \psi} \tag{6.35}$$

$$K_\psi = \frac{B}{r} \sum_k \mu_k \frac{\partial N_k}{\partial \phi} \tag{6.36}$$

where the "curvature" term in the azimuthal current is combined as shown in Equation 6.31.

Finally, we can use the surface currents that have been computed to measure a response to any poloidal field detector by using the Biot-Savart Law and a little trigonometry

$$B_\theta(r) = \frac{\mu_o}{4\pi} \int\int \frac{\hat{\theta} \cdot \mathbf{K}(\psi', \phi') \times (\mathbf{r} - \mathbf{r}')}{|\mathbf{r} - \mathbf{r}'|^3} \frac{d\psi' d\phi'}{B(\psi', \phi')} \tag{6.37}$$

where $\mathbf{r}'$ is the location at (ψ', ϕ') within the plane where $\xi = 0$ and $\theta = \pi/2$. HEISIM solves Equations 6.34, 6.35, and 6.36 by integrating the product of the sheet current with a Green's function.

6.4.2 Magnetic Module Results

Initial results for the magnetic module have not been promising. In the first calculation there was a normalization error that over-estimated the non-axisymmetric perturbation to the outer Mirnov sensor. The second calculation fixed this error, but the magnetic perturbations at the wall decreased significantly. Figure 6-7 shows these latest results for a 75% hot electron fraction. Typically, in the experiment, we observe magnetic fluctuation levels that exceed the average fluctuation level of the preceding stable period by a factor of two or three. Although the modified nonlinear simulation reproduces many characteristics resembling the HEI instability behavior observed in experimental measurements, perturbed magnetic observations of the high beta HEI instability are not reproduced by the simulation.

HEISIM does not represent the experiment in many ways. It is an initial-value code that preserves particle number. The outer walls have imposed a "zero-outward-flux" boundary condition. In the experiment, we have significant hot electron loss. The particles hit the wall and the F-coil ring. In the code, the hot electrons move toward the ring and the wall, but they never leave.

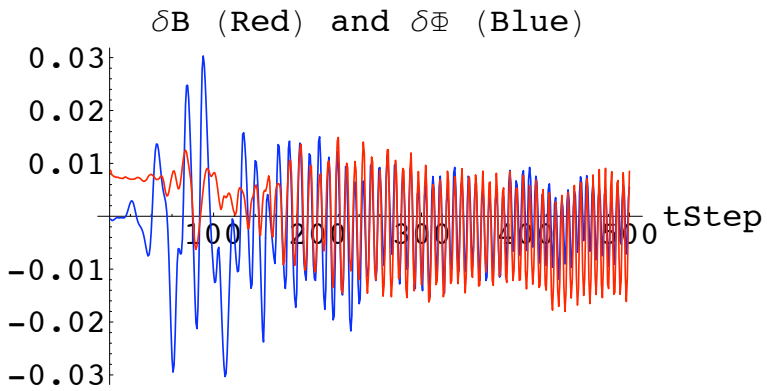

Figure 6-7: Initial results of the magnetic module added to HEISIM.

The magnetic module results remain inconclusive. The study does reveal that the presence of an HEI instability will cause a reduction of the hot electron high beta ring current. This change is detected experimentally and with the appropriate boundary conditions, may also be detected in future versions of the HEISIM code. A successful implementation of this code will allow for further exploration of the relationship between the intensity of the HEI burst and the overall change in diamagnetism associated with the outward expansion of the hot electrons during the instability.

6.5 Summary

A nonlinear, self-consistent numerical simulation of the growth and saturation of the HEI instability has been adapted for use with LDX experimental conditions. The code, HEISIM, reproduces many experimental observations including: frequency sweeping, transport of the hot electron density, mode amplitude saturation and a mode growth rate that increases proportionally with the hot electron fraction. Also, an attempt was made to extend the code to study the relationship between the high beta diamagnetic current carried by the hot electrons and the edge magnetic fluctuations during the instability. Unfortunately, despite developing a module to replicate these fluctuations at the edge, the analysis fell short of duplicating experimental observations.

Chapter 7

Summary

This thesis reports on the first study of the high beta, hot electron interchange instability in a laboratory, dipolar confined plasma. The HEI instability has been observed in LDX and measurements made using high-impedance, floating potential probes and fast Mirnov coils reveal the extent of the transport during high beta plasmas. LDX is the first dipole experiment to create consistently long-pulse, quasi-steady-state microwave discharges lasting more than 10 sec with equilibria having peak beta values of 20%.

7.1 New Results

Observations of the HEI instability in LDX have led to a better understanding of how the experiment behaves in the presence of the instability and also how to avoid it. The instability is found to occur under three conditions: during the low density regime, as local high beta relaxation events, and as global intense energy relaxation bursts. The spectrograms of this interchange instability reveal unique characteristics of the high beta HEI instability, which include: long lasting afterglow HEI instabilities, a relationship between the level of fueling and spectral characteristics of the HEI instability, the presence of both local and global HEI during high beta plasma, and differences in the quantity, timing and temporal characteristics of the HEI instabilities affected by the ECRH heating profile.

Achieving a high beta plasma state requires stabilizing the HEI pressure driven instability by properly adjusting the deuterium fuel and heating profile. The use of programmed gas puffs has proven to be an experimental control knob for determining when to enter and how

long to remain in the high beta plasma regime. With insufficient neutral gas pressure the plasma will become unstable to the hot electron interchange instability.

Magnetic and electrostatic diagnostics are used to study the plasma transport in the high beta LDX experiment. Unfortunately, magnetic diagnostics are affected by eddy currents driven in the experiment's walls. A correction for these is presented and applied to reveal the true rapidly changing magnetic signals. With these corrections Mirnov coils serve as a non-invasive, high speed diagnostic of transport for they compute the perturbed magnetic signals caused by the intense high beta HEI instability. Analysis of these and the other magnetic signals reveals that the magnitude of the fluctuations at the edge significantly exceed the magnitude of the equilibrium field generated by the high beta electrons. During the intense high beta HEI instability energetic electron confinement ends in under 100 μsec.

A guiding center drift Hamiltonian is used to described the interaction between the electrostatic wave and the high beta particles. Electrostatic waves are then modeled as a sum of traveling waves. With this formalism the motion of the particles is analyzed to determine if the condition for chaotic particle motion leads to global transport for a given wave spectrum. For the intense, high beta HEI instability the condition for global chaotic transport is met during the incoherent phase. It is not during the frequency chirping phase. Both of these results are in agreement with experimental observations. In addition, experimentally observed local relaxation events do not exhibit transport. This agrees with theory since they do not meet the criterion for global chaotic transport. The low beta HEI instability in LDX compares favorably with the HEI instability observations made in CTX. Finally, one of the consequences of the observed high beta transport is the presence of hysteresis in the neutral gas fueling required to stabilize and maintain the high beta plasma. High neutral fueling is required to create a high beta plasma, yet once stabilized, the plasma survives in a high beta state using a lower level of neutral fueling.

HEISIM, a nonlinear, self-consistent numerical simulation of the growth and saturation of the HEI instability, has been adapted for use with LDX experimental conditions and it reproduces many experimental observations. These include: frequency sweeping, transport of the hot electron density, mode amplitude saturation and a mode growth rate that increases with the hot electron fraction. An attempt to extend the code to study the relationship between the high beta diamagnetic current carried by the hot electrons and the edge magnetic fluctuations during the instability was presented. Unfortunately, despite developing a module

to replicate these fluctuations at the edge, our analysis fell short of duplicating experimental observations.

7.2 Future Work

Many opportunities remain for experimental research relating to the high beta HEI instability. In will be interesting to compare the results of these supported mode experiments with the results from new levitation experiments. Will the lack of supports allow for a higher n_i and make the experiment more stable to interchange instabilities? Also, how does plasma size affect the HEI instability and does this agree with the HEISIM results? Finally, since in its present state HEISIM does not represent the experiment (it does not account for electron losses at the wall and inner surfaces) would an alternate implementation using a NIMROD code, which accounts for sources and sinks, together with a kinetic model do a better job of modeling the high beta HEI instability? The perturbed magnetic response could (and should) be modeled to more fully understand how the plasma behaves during the high beta HEI instability.

Chapter 8

Appendix

8.1 Dipole Magnetic Field Notation

Plasma dynamics are greatly influence by the magnetic geometry involved in confinement. For that reason it is useful to work in a coordinate system that can represent a particular magnetic configuration. In our case the vacuum field of point dipole can be used to approximate the coil field because plasma pressure is low and most of the plasma volume is sufficiently far from the dipole electromagnet. The magnetic coordinates for a point dipole are especially easy since field-line integrals can be performed algebraically and it is curl-free.

An axisymmetric point dipole magnetic field can be represented in magnetic coordinates $\mathbf{B} = \nabla\varphi \times \nabla\psi = \nabla\chi$, where φ is the azimuthal angle of symmetry and ψ is the magnetic flux, (φ, ψ) defines a field-line and χ, the magnetic scaler potential, parametrizes the distance along a field-line. Spherical coordinates are used to represent these last two quantities as,

$$\psi = \mathrm{M}\frac{\sin^2\theta}{r}, \tag{8.1}$$

$$\chi = \mathrm{M}\frac{\cos\theta}{r^2}, \tag{8.2}$$

where $\mathrm{M} \equiv \mathrm{B}_o\mathrm{L}_o^3$ is the moment of the dipole magnet defined by the field strength at the equatorial ($\theta = \pi/2$) reference radius, L_o in analogy with McIlwain [43]. The dipole field has a magnitude of the form

$$\mathrm{B(r,}\theta) = \frac{\mathrm{M}}{r^3}\sqrt{(1 + 3\cos^2\theta)}, \tag{8.3}$$

Using this notation, a few useful identities from vector calculus are

$$\int\int\int d^3r = \int_0^{2\pi} d\varphi \int_{\psi_{min}}^{\psi_{max}} d\psi \int_{-\infty}^{+\infty} \frac{d\chi}{\mathrm{B}^2} \equiv \int_0^{2\pi} d\varphi \int_{\psi_{min}}^{\psi_{max}} d\psi \; \delta V \tag{8.4}$$

$$\nabla \cdot \mathbf{A} = \mathrm{B}^{\mathbf{2}} \frac{\partial}{\partial \varphi} \left(\frac{\mathbf{1}}{\mathrm{B}^{\mathbf{2}}} \nabla \varphi \cdot \mathbf{A} \right) + \mathrm{B}^{\mathbf{2}} \frac{\partial}{\partial \psi} \left(\frac{\mathbf{1}}{\mathrm{B}^{\mathbf{2}}} \nabla \psi \cdot \mathbf{A} \right) + \mathrm{B}^{\mathbf{2}} \frac{\partial}{\partial \chi} \left(\frac{\mathbf{1}}{\mathrm{B}^{\mathbf{2}}} \nabla \chi \cdot \mathbf{A} \right) \tag{8.5}$$

where δV is the differential volume of a tube per unit flux. The field-line integrals along χ are preformed by transforming the variable of integration to $\xi \equiv \sin^2 \theta$, such that

$$r = \frac{\mathrm{M}}{\psi} \xi, \quad \chi = \frac{\psi^2}{\mathrm{M}} \sqrt{\frac{1-\xi}{\xi^4}}, \quad \text{and } \left. \frac{d\chi}{d\xi} \right|_{\psi,\varphi} = \frac{\psi^2}{\mathrm{M}} \frac{3\xi - 4}{2\xi^3 \sqrt{1-\xi}}, \tag{8.6}$$

the flux tube average, $\langle \mathrm{A} \rangle$, is

$$\langle \mathrm{A} \rangle \equiv \frac{1}{\delta V(\psi)} \int \frac{d\chi}{\mathrm{B}^2} \; \mathrm{A}, \tag{8.7}$$

and the volume of a tube per unit flux becomes

$$\delta V(\psi) \equiv \int_{-\infty}^{+\infty} \frac{d\chi}{\mathrm{B}^2} = \frac{\mathrm{M}^3}{\psi^4} \int_0^1 \frac{d\xi \; \xi^3}{\sqrt{1-\xi}} = \frac{32}{35} \frac{\mathrm{M}^3}{\psi^4}. \tag{8.8}$$

The point-dipole definition, Equation 8.1, was used. Along the equatorial plane $\psi = \mathrm{M/L}$, and $\delta V \propto \mathrm{L}^4/\mathrm{M}$. This relationship between radius and flux-tube volume is a fundamental property of the dipole magnetic field.

An important simplification to be used later is the density-weighted flux-tube average [42]. It is defined as

$$\|\mathrm{A}\| \equiv \frac{\langle \mathrm{A}n \rangle}{\langle n \rangle} = \frac{1}{N} \int \frac{d\chi}{\mathrm{B}^2} \mathrm{A}n \tag{8.9}$$

where n is the plasma density and $N \equiv \langle n \rangle \delta V$ is the total number of particles on a tube per unit flux. When interchange dynamics are independent of the field-aligned distribution of density within a flux-tube, then interchange motion is two-dimensional. This assumes the profile function $n/\langle n \rangle$ is approximately independent of field-line location, (φ, ψ). A reasonable profile has $n/\langle n \rangle = \sin\theta$ and is independent of time and space.

Bibliography

[1] S. L. Allen, C. Clower, R. P. Drake, E. B. Hooper Jr., A. L. Hunt, R. Munger, R. J. Bastasz, W. Bauer, and W. L. Hsu. Initial wall conditioning for the tmx-u fusion experiment. *Journal of Vacuum Science and Technology A*, 1(2):916–919, April 1983.

[2] A.B. Antipenkov, P. Ladd, and R. Marrs. Iter glow discharge cleaning system. *Fusion Engineering and Design*, 56-57:233–238, October 2001.

[3] Fran Bagenal. Giant planet magnetospheres. *Annual Reviews of Earth and Planetary Science*, 20:289–328, 1992.

[4] H. L. Berk. Stability of hot electron plasmas. *Physics of Fluids*, 19(8):1255–1256, August 1976.

[5] H. L. Berk, B. N. Breizman, J. Candy, M. Pekker, and N. V. Petviashvili. Spontaneous holeclump pair creation. *Physics of Plasmas*, 6(8):3102–3113, August 1999.

[6] Allen H. Boozer. Guiding center drift equations. *Physics of Fluids*, 23(5):904–908, May 1980.

[7] Francis F. Chen. *Plasma Diagnostic Techniques*. Academic Press, 1965. 113-200, ed. Richard H. Huddlestone and Stanley L. Leonard.

[8] Xing Chen, B. G. Lane, D. L. Smatlak, R. S. Post, and S. A. Hokin. Experimental study of the hot electron plasma equilibrium in a minimum-b magnetic mirror. *Physics of Fluids B*, 1(3):615–628, March 1989.

[9] H. Dickinson, W. H. Bostick, J. N. DiMarco, and S. Koslov. Experimental study of rayleigh-taylor instability in plasma. *Physics of Fluids*, 5(9):1048–1056, September 1962.

[10] H. F. Dylla. Glow discharge techniques for conditioning high-vacuum systems. *Journal of Vacuum Science & Technology A*, 6(3):1276–1287, May 1988.

[11] Jennifer Ellsworth. X-ray diagnostics for the levitated dipole experiment. Master's thesis, MIT, 2004.

[12] Andrew Fazakerley and David Southwood. Magnetospheric interchange instability in anisotropic plasma. *Planetary and Space Science*, 41(3):245–255, March 1993.

[13] D. T. Garnier, A. Boxer, J. Ellsworth, A. Hansen, I. Karim, J. Kesner, S. Mahar, M.E. Mauel, E. Ortiz, and A. Roach. Production and study of high-beta plasma confined by a superconducting dipole magnet. *Physics of Plasmas*, 13(1), 2006.

[14] D.T. Garnier, J. Kesner, and M. E. Mauel. Magnetohydrodynamic stability in a levitated dipole. *Physics of Plasmas*, 6(9):3431–3434, September 1999.

[15] M. J. Gerver and B. G. Lane. Line-tying of interchange modes in a hot electron plasma. *Physics of Fluids*, 29(7):2214–2230, July 1986.

[16] T. Gold. Motions in the magnetosphere of the earth. *Journal of Geophysical Research*, 64(9):1219–1224, September 1959.

[17] O. Grulke and B. LaBombard, 2004. Private communications on Alcator Langmuir probe circuit boards.

[18] J. P. Gunn, C. Boucher, P. Devynck, I. Duran, K. Dyabilin, J. Horacek, M. Hron, J. Stckel, G. Van Oost, H. Van Goubergen, and F. Zcek. Edge flow measurements with gundestrup probes. *Physics of Plasmas*, 8(5):1995–2001, May 2001.

[19] A.H. Hansen, D.T. Garnier, M.E. Mauel, E.E. Ortiz, J. Kesner, A.C. Boxer, J.E. Ellsworth, I. Karim, S. Mahar, and A. Roach. Profile scan studies on the levitated dipoleprofile scan studies on the levitated dipole experimentexperiment. Poster BP1.108 Presented at the 46th Meeting of the American Physical Society, Division of Plasma Physics, November 2004.

[20] A.K. Hansen, S. Mahar, A.C. Boxer, J.L. Ellsworth, D.T. Garnier, I. Karim, J. Kesner, M. Mauel, and E.E. Ortiz. Initial results of multi-frequency electron cyclotron heating in the levitated dipole experiment. *AIP Conference Proceedings*, 787:395, 2005. 16th Topical Conference on Radiofrequency Power in Plasmas, Park City, UT, 4/11/05.

[21] Akira Hasegawa. A dipole field fusion reactor. *Comments Plasma Phys. Controlled Fusion*, 11(3):147–151, 1987.

[22] Wilmot N. Hess. *The Radiation Belt and Magnetosphere*. Blaisdell Publishing Company, 1968.

[23] S. Hiroe, J. B. Wilgen, F. W. Baity, L. A. Berry, R. J. Colchin, W. A. Davis, A. M. El Nadi, G. R. Haste, D. L. Hillis, D. A. Spong, T. Uckan, and T. L. Owens. Observation of hot electron ring instabilities in elmo bumpy torus. *Physics of Fluids*, 27(4):1019–1029, April 1984.

[24] I. H. Hutchinson. A fluid theory of ion collection by probes in strong magnetic fields with plasma flow. *Physics of Fluids*, 30(12):3777–3781, December 1987.

[25] I. H. Hutchinson. *Principles of Plasma Diagnostics*, volume 1. Cambridge University Press, 1987. 50-86.

[26] G.L. Jackson and et al. Particle control in diii-d with helium glow discharge cleaning conditioning. *Nuclear Fusion*, 30:2305–2317, 1990.

[27] Ishtak Karim. *Magnetic Equilibrium Results of the Levitated Dipole Experiment*. PhD thesis, MIT, 2006.

[28] M. C. Kelly. *The Earth's Ionosphere*. Academic Press, Sand Diego, CA, 1989.

[29] J. Kesner, L. Bromberg, D.T. Garnier, and M.E. Mauel. Plasma confinement in a magnetic dipole. *IAEA Fusion Engineering Conference (1998)*, 3:1165–1168, 1999.

[30] J. Kesner, D.T. Garnier, A. Hansen, M. Mauel, and L. Bromberg. Helium catalysed dd fusion in a levitated dipole. *Nuclear Fusion*, 44(1):193–203, January 2004.

[31] Nicholas A. Krall. Stabilization of hot electron plasma by a cold background. *Physics of Fluids*, 9:820–821, 1966.

[32] Natalia S. Krasheninnikova and Peter J. Catto. Effects of hot electrons on the stability of a closed field line plasma. *Physics of Plasmas*, 12:032101, March 2005.

[33] R. P. Lepping, M. H. Acutildena, L. F. Burlaga, W. M. Farrell, J. A. Slavin, K. H. Schatten, F. Mariani, N. F. Ness, F. M. Neubauer, Y. C. Whang, J. B. Byrnes, R. S. Kennon, P. V. Panetta, J. Scheifele, and E. M. Worley. The wind magnetic field investigation. *Space Science Reviews*, 71(1-4):207–229, February 1995.

[34] B. Levitt, D. Maslovsky, and M. E. Mauel. Observation of centrifugally driven interchange instabilities in a plasma confined by a magnetic dipole. *Physical Review Letters*, 94:175002, 2005.

[35] Ben Levitt, Dimitri Maslovsky, and Michael E. Mauel. Measurement of the global structure of interchange modes driven by energetic electrons trapped in a magnetic dipole. *Physics of Plasmas*, 9(6):2507–2517, June 2002.

[36] Benjamin Joseph Levitt. *Global Mode Analysis of Rotation and Curvature Driven Interchange Instabilities*. PhD thesis, Columbia University, 2004.

[37] Minxu Li and H.F. Dylla. Reduction of outgassing rate by glow discharge cleaning. *Journal of Vacuum Science*, 13(3):571–575, May 1994.

[38] W. Lochte-Holtgreven. *Plasma Diagnostics*. American Institute of Physics, 1995. Ch11, 668-731, by L. Schott.

[39] D. Maslovsky, B. Levitt, and M. E. Mauel. Observation of nonlinear frequency-sweeping suppression with rf diffusion. *Phys Rev Lett*, 90:185001, 2003.

[40] D. Maslovsky, B. Levitt, and M. E. Mauel. Suppression of nonlinear frequency-sweeping of resonant interchange modes in a magnetic dipole with applied radio frequency fields. *Physics of Plasmas*, 10(5):1549–1555, May 2003.

[41] D. A. Maslovsky, M. E. Mauel, and B. Levitt. Numerical simulation of phase-space flows in the collisionless terrella experiment. *IEEE Trans Plasma Sci*, 30(1):8–9, February 2002.

[42] M. E. Mauel. Laboratory observations of wave-induced radial transport within an 'artificial radiation belt". *J Phys IV France*, 7:307, 1997.

[43] Carl E. McIlwain. Coordinates for mapping the distribution of magnetically trapped particles. *Journal of Geophysical Research*, 66(11):3681–3691, November 1961.

[44] Dale M. Meade. Fluctuations in a plasma confined by a toroidal octupole magnetic field. *Physical Review Letters*, 17(13):677–679, September 1966.

[45] Theodore G. Northrop and Edward Teller. Stability of the adiabatic motion of charged particles in the earth's field. *Phys Rev*, 1(1):215–225, January 1960.

[46] J. C. Orchard, A. T. Peacock, and G. Saibene. Jet experience in recovery from large air leak incidents. *Journal of Nuclear Materials*, 200:395–399, May 1993.

[47] E.E. Ortiz, A.C. Boxer, J.L. Ellsworth, D.T. Garnier, A.K. Hansen, I. Karim, J. Kesner, and M.E. Mauel. Effects of the hot electron interchange instability on plasma confined in a dipolar magnetic field. *Journal of Fusion Energy*, ???(???):???, 2007.

[48] M. N. Rosenbluth and C. L. Longmire. Stability of plasmas confined by magnetic fields. *Annals of Physics*, 1:120–140, 1957.

[49] C. T. Russell. The dynamics of planetary magnetospheres. *Planetary and Space Science*, 49(10-11):1005–1030, August 2001.

[50] K. Rypdal, O. E. Garcia, and J.V. Paulsen. Anomalous cross-field current and fluctuating equilibrium of magnetized plasmas. *Phys Rev Lett*, 79:18571860, 1997.

[51] J. H. Schultz, G. Driscoll, D. Garnier, J. Kesner, M. Mauel, J.V. Minervini, B. Smith, A. Radovinsky, G. Snitchler, and A. Zhukovsky. High temperature superconducting levitation coil for the levitated dipole experiment. *IEEE Transactions on Applied Superconductivity*, 11(1):2004–2009, March 2001.

[52] J. H. Schultz, J. Kesner, J. Minervini, A. Radovinsky, S. Pourrahimi, B. Smith, P. Thomas, P. Wang, A. Zhukovsky, R. Myatt, S. Kochan, M.E. Mauel, and D.T. Garnier. The levitated dipole experiment (ldx) magnet system. *IEEE Transactions on Applied Superconductivity*, 9:378–381, 1999.

[53] B.A. Smith, J.H. Schultz, A. Zhukovsky, A. Radovinsky, C. Gung, P.C. Michael, J.V. Minervini, J. Kesner, D.T. Garnier, M.E. Mauel, G. Naumovich, and R. Kocher. Design, fabrication and test of the react and wind, nb3sn, ldx floating coil. *IEEE Transactions on Applied Superconductivity*, 11:2010–2013, 2001.

[54] David J. Southwood and Margaret Kivelson. Magnetospheric interchange motions. *Journal of Geophysical Research*, 94(A1):299–308, January 1989.

[55] David J. Southwood and Margaret G. Kivelson. Magnetospheric interchange instability. *Journal of Geophysical Research*, 92(A1):109–116, January 1987.

[56] L. Spitzer. *Physics of Fully Ionized Gases*. New York: Interscience, 1956.

[57] H. P. Warren and M. E. Mauel. Observation of chaotic particle transport induced by drift-resonant fluctuations in a magnetic dipole field. *Phys Rev Lett*, 74:13511354, February 1995.

[58] H. P. Warren and M. E. Mauel. Wave-induced chaotic radial transport of energetic electrons in a laboratory terrella experiment. *Physics of Plasmas*, 2(11):4185–4194, November 1995.

[59] H. P. Warren, M. E. Mauel, D. Brennan, and S. Taromina. Observation of wave-induced chaotic radial transport in a laboratory terrella experiment. *Physics of Plasmas*, 3(5):2143–2148, May 1996.

[60] Harry Paul Warren. *Observation of Chaotic Particle Transport Driven by Drift-Resonant Fluctuations in the Collisionless Terrella Experiment*. PhD thesis, Columbia University, 1994.

[61] Frank J. *Øynes*, Hans L. *Pécseli*, and Kristoffer Rypdal. Fluctuations in a magnetized toroidal plasma without rotational transform. *Phys Rev Lett*, 75:81–84, July 1995.

[62] A. Zhukovsky, D. Garnier, C. Gung, J. Kesner, M.E. Mauel, P. Michael, J. Minervini, M. Morgan, T. Pedersen, A. Radovinsky, J. Schultz, and B. Smith. Status of the floating coil of the levitated dipole experiment. *IEEE Transactions on Applied Superconductivity*, 12:666–669, 2002.

[63] A. Zhukovsky, D.T. Garnier, and A. Radovinsky. Thermal perfomance of the ldx floating coil. *Advances in Cryogenic Engineering*, 2006. Cryogenic Engineering Conference 2005, Keystone, Colorado, August 29 - September 2, 2005, (2005) R1-M.

[64] A. Zhukovsky, M. Morgan, D.T. Garnier, A. Radovinsky, B. Smith, J. Schultz, L. Myatt, S. Pourrahimi, and J. Minervini. Design and fabrication of the cryostat for the floating coil of the levitated dipole experiment (ldx). *IEEE Transactions on Applied Superconductivity*, 10:1522–1525, 2000.

[65] A. Zhukovsky, J. Schultz, B. Smith, A. Radovinsky, D.T. Garnier, O. Filatov, V. Beljakov, S. Egorov, V. Kuchinsky, A Malkov, E. Bondarchouk, V. Korsunsky, and V. Sytnikov. Charging magnet for the floating coil of ldx. *IEEE Transactions on Applied Superconductivity*, 11:1873–1876, 2001.